# FUNDAMENTAL STUDIES OF CROSSFLOW HEAT EXCHANGERS FOR LAMINAR AND TURBULENT FLOWS

A Dissertation
SUBMITTED TO THE FACULTY OF
UNIVERSITY OF MINNESOTA
BY

Jungwon Ahn

IN PARTIAL FULFILLMENT OF THE REQUIREMENTS
FOR THE DEGREE OF
DOCTOR OF PHILOSOPHY

Prof. Ephraim M. Sparrow

August, 2017

**Acknowledgements**

I am now at the end of my Ph.D. program. At this moment in time, I take a breath and look back over the past times and realize that I am very blessed having many people that I am thankful to.

Words cannot express how much I feel thankful to my advisor, Professor Ephraim Sparrow, for his unconditional support. In addition to invaluable advice and guidance to my thesis work, he was my mentor for the entirety. I will remember forever the hours of friendship I have spent with him as well as the many days and nights I have talked about my research with him.

Professor Kuehn has also given me priceless help and advice in teaching and I would like to express my sincere gratitude to him. I have been very fortunate to work for him twice as a teaching assistant. I will never forget all the moments that I have intellectually talked with him. I would also like thank him for giving me excellent comments and advices when serving as my committee member. I also want to thank Professor Rusen Yang and Professor Kevin Leder for serving my Ph.D. final presentation committee members and encouraging me during my Ph.D. program. I am also grateful for Professor Vinod Srinivasan for his support and help in teaching.

I also appreciate my lab mates especially John Gorman and Winston Tan for their help and support in CFD simulations and experiments for this research and other projects. My friends that I have met in Minnesota from the department of Mechanical Engineering, from the Carlson School, and from Saint Andrew Kim Church have been very influential and I would also like to thank them for their continuous support.

Lastly, I would like to express my deep gratitude to my parents and my brother, Hyungjune Ahn, for their unlimited support with their sincere love.

## Dedication

*To my lovely wife and daughter: Ja young Koo and Erin Anna Ahn*.

## Abstract

The focus of this thesis research is heat transfer and fluid flow in heat exchangers where a fluid flows across heated cylindrical elements. Three unique devices are considered, and highly detailed and accurate solutions are obtained for each by making use of advanced numerical simulation techniques. As prerequisite to the implementation of these solutions, validation of the numerical procedure was obtained by comparing highly accurate and complete experimental data to the numerical predictions for a relevant test case.

The first considered situation is a two-dimensional, in-line tube bank where the number of rows and the Reynolds number serve as parameters. New methods were devised to determine the prevailing flow regime in the tube bank, one based on the calculation of the turbulent viscosity and the other utilizing a comparison of heat transfer coefficients respectively determined from laminar and turbulent models. Array-based average heat transfer coefficients showed that shorter arrays gave rise to higher values of the transfer coefficient, in contrast to certain literature predictions.

The second studied case is the simultaneous treatment of heat transfer in a pin-fin array and the fluid flow created by a conventional rotating fan which is delivered to the inlet of the array. The basic issue is the nature of the delivered flow. Even when a blower curve is used, it is assumed that the delivered flow is uniformly distributed across the heat exchanger. In reality, when blade rotation of the fluid mover are taken into account, the uniformity disappears. In fact, the delivered flow includes a swirl component superimposed on the main axial flow. The velocity of the delivered flow may be larger adjacent to the walls than it is in the core of the flow. In many cases, backflow occurs, driven by the rotation of the hub of the fan. The outcome of the work is that correct results require simultaneous treatment of the fluid mover and the heat exchanger.

The final dealt-with case is the cylinder in crossflow and provides the most complete set of transient heat transfer results ever.

## Table of Contents

## List of Tables

## List of Figures

# CHAPTER 1

## INTRODUCTION

A heat exchanger is a device which brings two fluids of different temperatures into intimate thermal contact without mixing. The most commonly used category of heat exchanger is the recuperator. In these devices, the two fluids are kept separate from each other by the walls of pipes which contain them. Heat exchangers are encountered in virtually phase of everyday life, and their existence and proper functioning is necessary to sustaining life on the planet as we know it.

Heat exchangers have appeared in literature citations as early as 1888, which marks the beginning of the search engine presently called *Compendex*, originally *Engineering Index*. However, since heat exchangers are equipment that have great commercial value, it can be assumed that there is much existing information that is regarded as protected intellectual property. The published work is primarily academically based and, as a consequence, is strongly dominated by idealized assumptions. The academic approach tends to focus on components rather than on entire heat exchangers.

Here, a different approach is taken. The depth of the present work was chosen to go well beyond that encountered in the typical academic-based publication but also to deal with highly complex issues which appear not to have been previously investigated in the open literature. The methodology of the present work is based on numerical simulation. Therefore, it was regarded as necessary that the simulation model be validated by comparisons of results from the simulations and experimental data. This success of this validation effort provided the license to apply the simulation model to deal with both fundamental and applied issues that had not been studied previously.
All of the heat exchangers and components investigated here belong to the most commonly encountered heat-exchanger geometrical configuration in which the fluid flow

passes in crossflow over cylindrical tubes. By crossflow, it is meant that the flow direction is at right angles to the axis of the cylindrical object. Three different configurations are considered: (a) a multi-row tube bank, (b) a pin-fin array whose fluid flow is delivered by a rotating fan, and (c) a cylinder in crossflow for which the turbulence intensity of the oncoming freestream flow is a varied parameter. Although the ultimate focus is on the heat transfer phenomena for these situations, the fluid flow aspects that are a necessary requisite for the study of convective heat transfer methodologies were treated with the necessary depth.

The thesis consists of six chapters including this Introduction. Chapter Two deals with heat exchangers composed of in-line tube banks. This apparently well-established device motivates study of a number of fundamental questions: (a) what is the criterion for the breakdown of the laminar flow regime, (b) does transient operation smoothly converge to a steady state, (c) does the geometric symmetry of the tube bank configuration necessarily lead to fluid flow and thermal symmetry, (d) what is the nature of the dependence of the heat transfer coefficient on the number of tubes in the array.

Chapter Three sets the stage for the multi-dimensional, transient and steady turbulent fluid flow and heat transfer problems that are dealt with in later chapters. It is an unwritten rule that numerical simulations must be validated before their results can be seriously regarded as possessing high accuracy and archival status. The validation normally consists of comparing the predictions from the simulations with experimental results of impeccable accuracy. The main drawback in carrying out this procedure is the difficulty of finding experiments that correspond to the physical situation being considered for numerical solution. In fact, this drawback is so great that it is common to look for a somewhat different approach. That alternative is to identify the key physical processes in the actual physical situation and then to look for experiments for situations where the key process are the same or similar to the actual ones. This is the approach followed in Chapter Three.

In Chapter Three, the related physical experiments are for turbulent fluid flow in a pin-fin array situated in a rectangular duct with tip clearance between each pin fin and the upper wall of the duct. The setup included control of the fluid flow at the inlet of the duct, a pin-fin-free hydrodynamic development length, and a fin array of sufficient length to permit periodic flow to develop. The agreement between the predictions of the numerical simulations and the experimental data was exceptionally good, providing support for the use of the simulation model for the problems of subsequent chapters.

The next chapter, Chapter Four, deals with a fundamental issue in heat exchanger theory and design. In both the published academic-based literature and in design practice, it is rare to encounter the fluid-mover, which supplies fluid to the heat exchanger, and the exchanger to be considered as a single interactive system. The closest that such interactions are considered is when a blower curve is used to relate the flow rate Q and the pressure drop P of the exchanger with that of the fan or blower which serves as the fluid mover. Even when his accounting is considered, it does not account for the most profound interactions.

The basic issue is the nature of the supplied flow. Even when a blower curve is used, it is assumed that the delivered flow is uniformly distributed across the inlet of the heat exchanger. In reality, when the rotating blades of the fluid mover are taken into account, the uniformity disappears. In fact, the delivered flow includes a swirl component superimposed on the main axial flow. Equally important is the fact that nonuniformity dominates rather that uniformity. In fact, the velocity of the delivered flow may be larger adjacent to the walls than it is in the core of the flow. In many cases, backflow occurs, driven by the rotation of the hub of the fan.

These realistic but rarely considered features cause heat exchanger design to depart from the realities of heat exchanger operation. Chapter Four deals with the case of a duct-housed array of pin fins that function as a heat exchanger for the management of electronic equipment. Air is supplied to the inlet of the heat exchanger by means of an

axial fan whose rotating blades are the source of fluid motion. Numerical simulation enables the detailed fluid flow field to be determined. Subsequently, the per-fin heat transfer rates and the total array heat transfer are computed. In order to identify the inaccuracies that correspond to the standard simplified heat exchanger analysis method, solutions and results are obtained via numerical simulation for the standard model.

The last substantive problem is dealt with in Chapter Five. The focus of the chapter is the effect of turbulence intensity on fluid flow and heat transfer. This is a very complicated phenomenon, and it was thought reasonable to begin the investigation with what might be a relatively simple model problem. This was the thinking that led to consideration of a one-row heat exchanger, which is a cylinder-in-crossflow. A cylinder–in-crossflow experiences a number of phenomena that could be affected by the intensity of freestream turbulence. Chief among these is the separation phenomenon, where the boundary layer on the forward part of the cylinder is unable to follow the contour of the surface as the zone of freestream pressure rise is approached. The location at which separation occurs defines so-called subcritical and supercritical operation, with the critical operating point corresponding to the movement of the separation point from the forward part of the cylinder to the rearward part.

The work described in Chapter Five takes advantage of the available computer resources to obtain a much finer resolution of unsteady phenomena than has been reported in the literature. The presence of a periodic steady state was identified for the first time in which the flow and heat transfer vary periodically after the passage of a start-up transient.

It may be observed that an explicit literature review is not included in the foregoing paragraphs. It was deemed advantageous to review the literature that is relevant to each chapter to that very chapter. Chapter Six is a summary of the accomplishments of the thesis.

# CHAPTER 2

## NEW DESIGN METHOLOLOGIES FOR IN-LINE ARRAY HEAT EXCHANGERS

## 2.1 Introduction

There are many types of heat exchangers whose internal configurations depend on the nature of the application. One of the most common configurations is a crossflow in which an array of circular tubes, situated in a periodic pattern, exchanges heat with a fluid that passes over the tubes. The two most common periodic patterns are in-line and staggered. Both of these physical situations have been subjected to extensive investigation. Notwithstanding this, there are many crucial issues that remain unresolved. These issues include: (a) the quantification of flow regimes and the Reynolds numbers that define the regimes, (b) effect of numbers of rows, (c) start-up transient, and (d) symmetry. These issues will be explored by means of numerical simulations. Since the foregoing issues are generic, it is deemed sufficient to focus on one of the standard geometric arrangements, namely, the in-line array type.

A generic schematic diagram of an in-line array is displayed in Figure 2.1. As seen there,

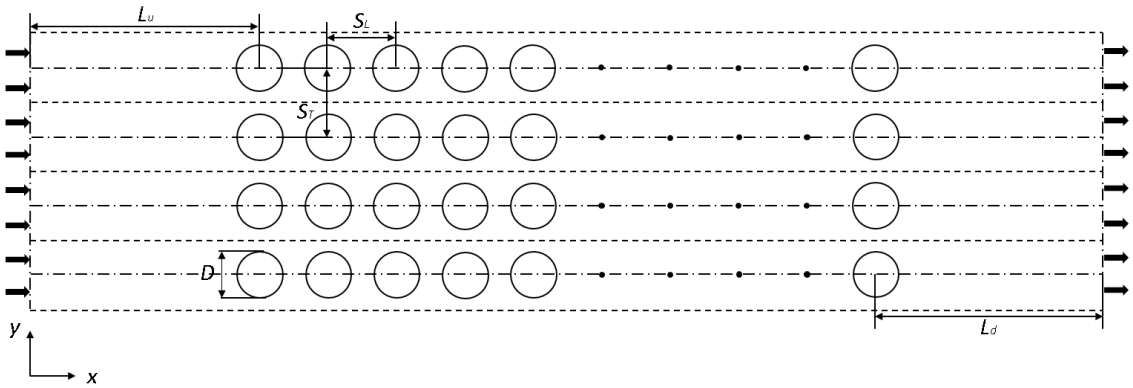


Figure 2.1 Schematic diagram of an in-line array of cylinders.

the tubes are situated periodically in the streamwise direction and symmetrically in transverse direction. The fluid inlet is situated a distance $L_u$ upstream of the center of the first row of tubes. Similarly, the fluid exit is situated downstream of the center of the last row by a distance $L_d$. The tube diameter is $D$, the longitudinal center-to-center distance between rows is $S_L$, and the transverse center-to-center distance is $S_T$.

The plan of the research is as follows:

(a) Flow regime determination. It has been established [1] that the Shear Stress Transport (SST) turbulence model reduces to virtually laminar flow when applied in a flow regime that is truly laminar. This knowledge suggests that duplicate solutions, one strictly laminar and the other SST-based turbulent be obtained for each Reynolds number of interest. Comparison of these two sets of results will enable a valid definition of the flow regime.

(b) One of the literature citation [2] has reported start-up transient results which display an irregular approach to steady state. That investigation was focused on the turbulent flow regime. Here, where laminar flow is the focus. The start-up transient will be inspected to determine whether the observation of [2] continues to persist.

(c) Reference [3] also questioned whether the geometric symmetry of the array led to fluid flow and heat transfer symmetry, and that issue will also investigated here.

(d) Another literature issue relates to how the performance of arrays having different number of tubes compare with each other. The results of [4, 5] indicate that the heat transfer coefficient for an array of fewer tubes is smaller than that for an array of a greater number of tubes. This outcome is believed to be incompatible with physical reasoning. The issue will, therefore, be addressed here in a quantitative manner.

## 2.2 Governing Equations

Since the present investigation deals with both laminar and turbulent models of fluid flow and heat transfer, the governing equations must encompass both regimes. For convenience, the equations will be written for the turbulent regime, and the non-turbulent terms will be pointed out. The physical principles that govern the fluid flow and heat transfer are: momentum conservation, mass conservation, and the First Law of Thermodynamics. The turbulent flow interpretation of these principles, written for incompressible, constant property flow, are

$$\rho \frac{\partial u_j}{\partial t} + \rho \left( u_i \frac{\partial u_j}{\partial x_i} \right) = - \frac{\partial p}{\partial x_j} + \frac{\partial}{\partial x_i} \left( \mu \frac{\partial u_j}{\partial x_i} + \mu_{turb} \right) \quad i = 1,2 \;\; j = 1,2 \tag{2.1}$$

These equations are written in Cartesian tensor notation for compactness. The term $\mu_{turb}$ denotes the turbulent viscosity. This is a fictive quantity defined to account for the momentum transfer that is due to the turbulent velocity fluctuations as given by

$$\mu_{turb} = - \rho \overline{u_i' u_j'} \tag{2.2}$$

where the $u_i'$ represent the fluctuating component of $u_i$. Equations (2.1) are called the Reynolds Average Navier Stokes (RANS) equations.

The mass conservation equation is

$$\frac{\partial u_i}{\partial x_i} = 0 \tag{2.3}$$

Turbulence does not appear in this equation because the time-average of the turbulent fluctuation is zero.

The quantity $\mu_{turb}$ is determined from the use of the SST turbulence model [1]. It consists of a pair of simultaneous, non-linear partial differential equations for the turbulence kinetic energy $\kappa$ and ω which is the specific rate of turbulence dissipation. The equations of the SST model are

$$\frac{\partial(\rho u_i \kappa)}{\partial x_i} = P_\kappa - \beta_1 \rho \kappa \omega + \frac{\partial}{\partial x_i}\left[\left(\mu + \frac{\mu_{turb}}{\sigma_\kappa}\right)\frac{\partial \kappa}{\partial x_i}\right] \tag{2.4}$$

$$\frac{\partial(\rho u_i \omega)}{\partial x_i} = A\rho S^2 - \beta_2 \rho \omega^2 + \frac{\partial}{\partial x_i}\left[\left(\mu + \frac{\mu_{turb}}{\sigma_\omega}\right)\frac{\partial \omega}{\partial x_i}\right] + 2\rho(1 - F_1)\frac{1}{\sigma_{\omega 2}\omega}\frac{\partial \kappa}{\partial x_i}\frac{\partial \omega}{\partial x_i} \tag{2.5}$$

The solution of Equations (2.4) and (2.5) yields the values of $\kappa$ and $\omega$, which give the turbulent viscosity $\mu_{turb}$ from

$$\mu_{turb} = \frac{\alpha \rho \kappa}{\max(\alpha\omega, SF_2)} \tag{2.6}$$

The symbols that appear in the foregoing equations are defined as

| | |
|---|---|
| $A$ | model constant |
| $F_1$, $F_2$ | blending functions in the SST model |
| $P_k$ | production term for the turbulent kinetic energy |
| $S$ | absolute value of the shear strain rate |
| $u$ | local velocity |
| $x_i$ | tensor coordinate direction |
| $\alpha$ | SST model constant |
| $\beta_1$, $\beta_2$ | SST model constants |
| $\omega$ | specific rate of turbulence dissipation |
| $\mu$ | molecular viscosity |
| $\mu_{turb}$ | turbulent viscosity |

$\kappa$ turbulence kinetic energy

$\sigma$ diffusion coefficient

$\rho$ fluid density

The heat transfer problem is governed by the First Law of Thermodynamics. For incompressible, constant property flow, the First Law can be written as

$$\rho c_p \frac{\partial (u_i T)}{\partial x_i} = \frac{\partial}{\partial x_i}\left[(k + k_{turb})\frac{\partial T}{\partial x_i}\right] \tag{2.7}$$

where, again, Cartesian tensor notation has been used. In this equation, $T$ is the temperature, $c_p$ is specific heat, and $k$ is the thermal conductivity. The quantity $k_{turb}$ is commonly referred to as the turbulent thermal conductivity. Its value is closely connected to that of the turbulent viscosity by means of the turbulent Prandtl number

$$Pr_{turb} = \frac{c_p \mu_{turb}}{k_{turb}} \tag{2.8}$$

There is an extensive literature that has shown that a constant value of $Pr_{turb} = 0.85$ [11, 12] gives rise to highly accurate heat transfer results.

## 2.3 Numerical Simulation

Numerical simulation was used to quantify the responses to the issues that have been raised in the foregoing paragraphs. The numerical tool that was employed is ANSYS – CFX 15.0. This software package is based on finite-volume discretization. The meshing of the discretized solution domain was performed based on the principles: (a) fine mesh in zones of high gradients and (b) fine mesh adjacent to all solid surfaces. Another major issue was the sufficiency of number of nodes. That issue is commonly termed mesh independence. To demonstrate mesh independence, three different meshes were employed and the corresponding Nusselt numbers compared. The respective mesh

included 1.8, 2.2 and 3.5 million, with Nusselt numbers of 6.098, 6.099, and 6.095. It was concluded that any number of nodes greater than 1.8 million would yield highly satisfactory results. Thereafter, all of the results were obtained for mesh numbers between 1.8 and 2.2 nodes.

## 2.4 Results for Determination of the Flow Regime

It has been found elsewhere [1] that at sufficiently low Reynolds number, the SST turbulence model virtually reduces to laminar flow. This finding was based on calculating the ratio of $\mu_{turb}/\mu$, where $\mu_{turb}$ is the turbulent viscosity as defined earlier, and $\mu$ is the viscosity of the medium. This methodology will be applied here in addition to the more practical approach of comparing Nusselt numbers determined for a pure laminar model with those calculated using a turbulence model. The second approach will now be implemented. In this regard, it is first necessary to convey the definition of the Nusselt number that was employed here.

### 2.4.1 Comparison of Nusselt number for laminar and turbulence model

At the time at which this research was initiated, it was planned to determine the Nusselt number for each individual cylinder in the array. However, careful evaluation of the recirculation zone that fills the space between successive cylinders suggested that a local bulk temperature could not be obtained with sufficient degree of accuracy. The reason for this conclusion is that the existence of forward flow and back flow in the inter-cylinder space did not lend itself to the calculation of the bulk temperature. In this light, attention was redirected to the determination of the array-average heat transfer coefficient for each of the investigated arrays.

The array-average heat transfer coefficient is defined as

$$\bar{h} = \frac{\sum_{i=1}^{N} Q_i}{LMTD} \tag{2.9}$$

In this equation, $Q_i$ is the rate of heat transfer from cylinder *i* to the flowing fluid. The value of $Q_i$ was obtained by integrating the local heat flux at each angular position of cylinder *i* around the circumference of the cylinder. For the calculation of the log-mean temperature difference (LMTD), the needed temperatures are the fluid bulk temperatures both upstream of the first cylinder (*i = 1*) and downstream of the last cylinder (*i = N*) of the array. With these quantities and with the cylinder wall temperature $T_w$ which is uniform for all cylinders, the LMTD definition is

$$LMTD = \frac{(T_w - T_{b1}) - (T_w - T_{bN})}{\ln\left[\frac{T_w - T_{b1}}{T_w - T_{bN}}\right]} \tag{2.10}$$

The array-average Nusselt number houses $\bar{h}$ in dimensionless form according to the definition.

$$Nu = \bar{h}D/k \tag{2.11}$$

The Nusselt number results are parameterized by the Reynolds number, defined as

$$Re = \rho U_{max} D/\mu \tag{2.12}$$

In this equation, $\rho$ and μ are the density and viscosity of the flowing fluid which is taken as air for the present investigation. The quantity that needs some discussion is $U_{max}$. The use of $U_{max}$ as the characteristic velocity is traditional although by no means necessary. It is based on the assumption that the maximum velocity in the entire flow field occurs in the cross section of smallest geometric area. It has been shown elsewhere [7] that that assumption is fallacious. Nevertheless, it was deemed appropriate to continue to use the standard definition of $U_{max}$ to provide continuity with the literature.

It is appropriate to derive the relationship between $\overline{U}$ and $U_{max}$ for the dimensions that were employed in the investigation. The specified non-dimensionalized dimensions are $\frac{S_T}{D} = \frac{S_L}{D}$ = 1.5. To facilitate the derivation, it is convenient to make a reference to Figure 2.2. From the geometry shown there, it can be deduced that

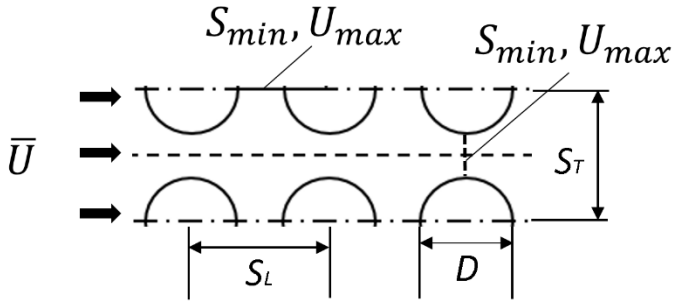


Figure 2.2 Diagram for the relationship between $\overline{U}$ and $U_{max}$.

$$S_T = 0.5D + 0.5D + S_{min} = 1.5\ \mathrm{D} \tag{2.13}$$

So that $S_{min} = 0.5D$. Since $S_T = 1.5D$, it follows that $S_{min} = \left(\frac{1}{3}\right) S_T$ . As a consequence,

$$U_{max} = 3\overline{U} \tag{2.14}$$

Numerical experiments were performed for values of the Reynolds number ranging between 100 and 1,000 in increments of 100. The Nusselt numbers results for Re = 100 for both the laminar model and the SST turbulence model are displayed in Figure 2.3. As

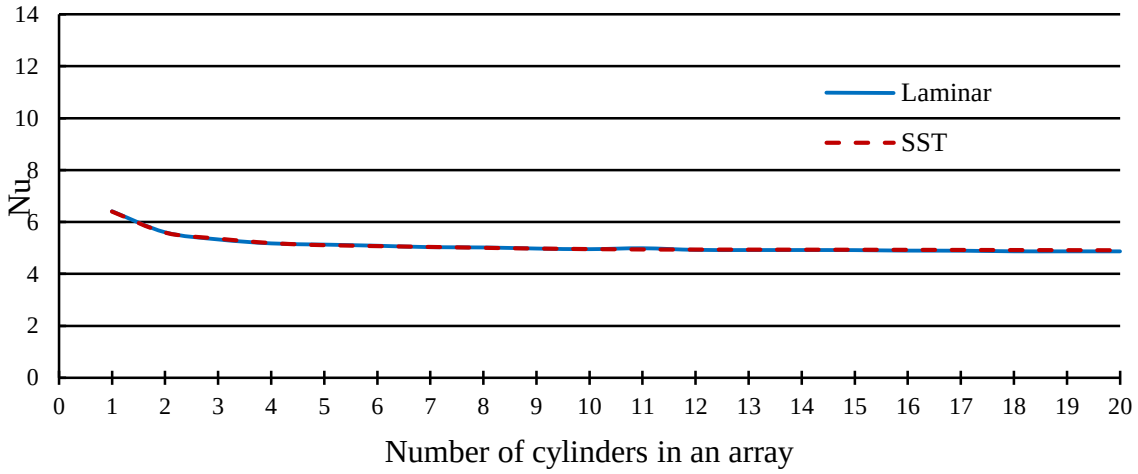


Figure 2.3 Array-average Nusselt numbers for Re = 100.

seen there, the two models provided identical Nusselt numbers results. This outcome verifies that the flow is truly laminar at this Reynolds number. It is also noteworthy that the largest value of the Nusselt number corresponds to arrays which have the fewest number of cylinders. Equally worthy of note is the leveling off of the Nusselt number to a value that is identical to arrays of seven and more cylinders. It is not unreasonable to denote that situation as *fully developed*.

The next result to be presented is for are Re = 200, and Figure 2.4 has been prepared for that purpose. A careful comparison of this figure with its antecedent confirms the

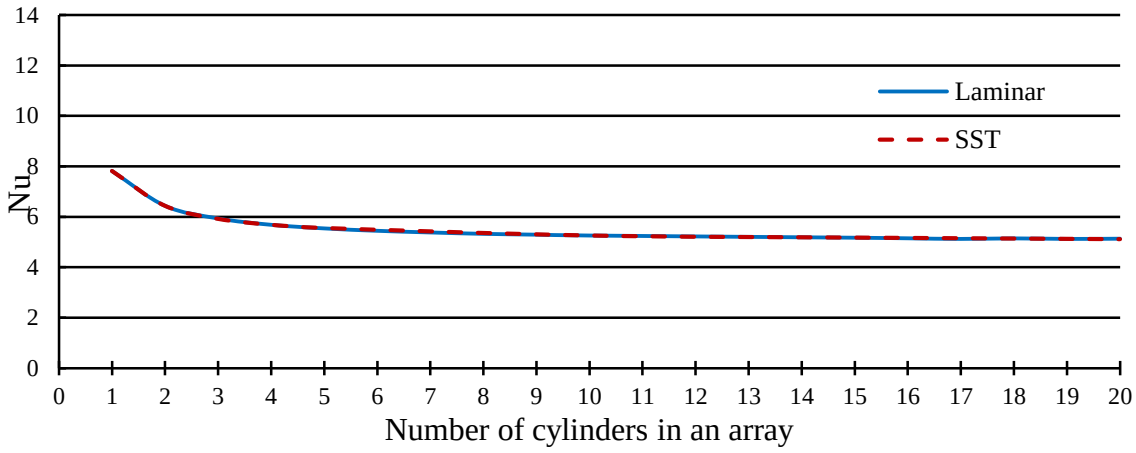


Figure 2.4 Array-average Nusselt numbers for Re = 200.

continuing existence of laminar flow. One of the differences between the results of the two figures is that constancy of the Nusselt number is not achieved at the higher Reynolds number for arrays whose number of cylinders equals or exceeds 11. This outcome is to be compared with the fact that constancy of the Nusselt number sets in for arrays of seven or more cylinders. Another difference is that the fully developed Nusselt number is somewhat higher for the larger Reynolds number.

The next in this sequence, Figure 2.5, exhibits the Nusselt number results for Re=300.

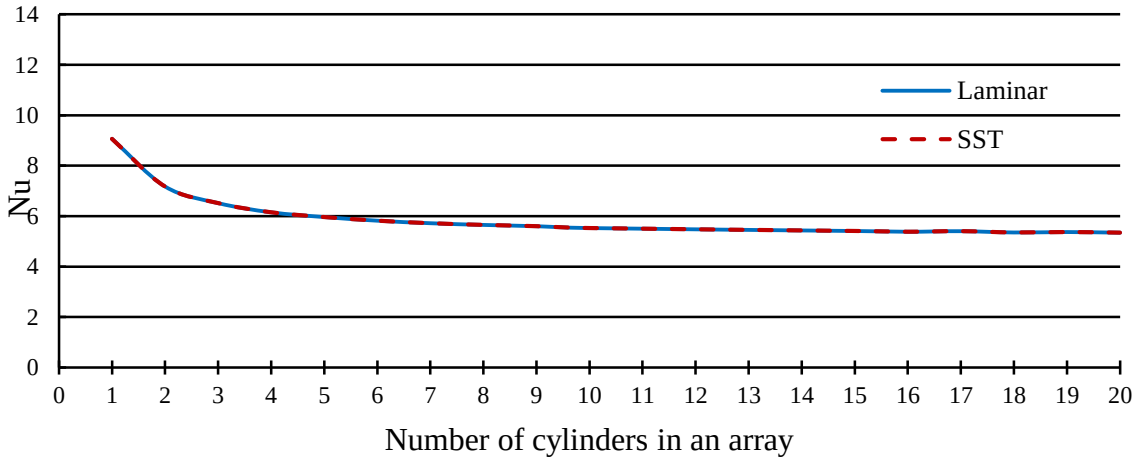


Figure 2.5 Array-average Nusselt numbers for Re = 300.

Inspection of this figure and comparison with the two preceding figures reveals a continuation of the trends that have already been identified and discussed. The presentation continues successively to higher Reynolds numbers. The results displayed in Figures 2.6 and 2.7, respectively for Reynolds numbers of 400 and 500, begin to show small deviations between laminar and turbulent curves. These deviations are sufficiently small as to support the laminar model.

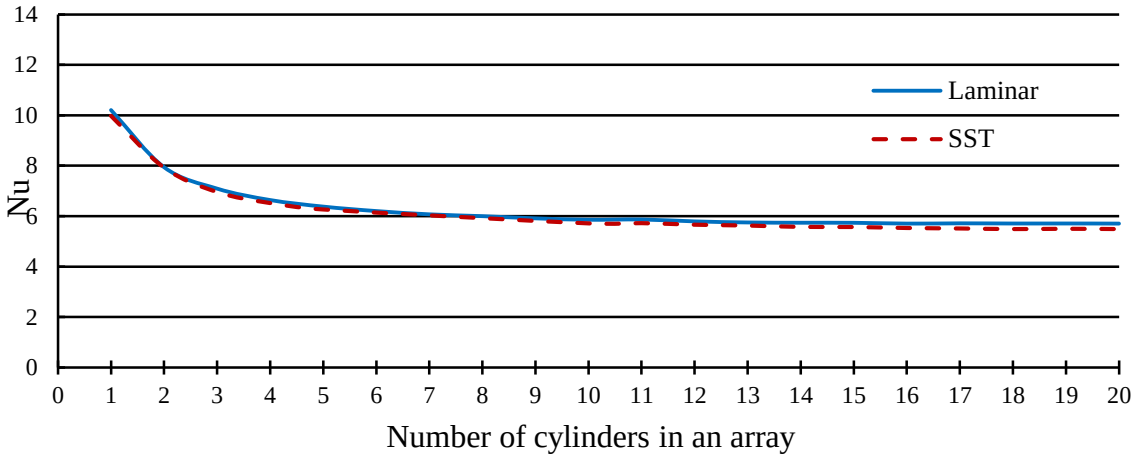


Figure 2.6 Array-average Nusselt numbers for Re = 400.

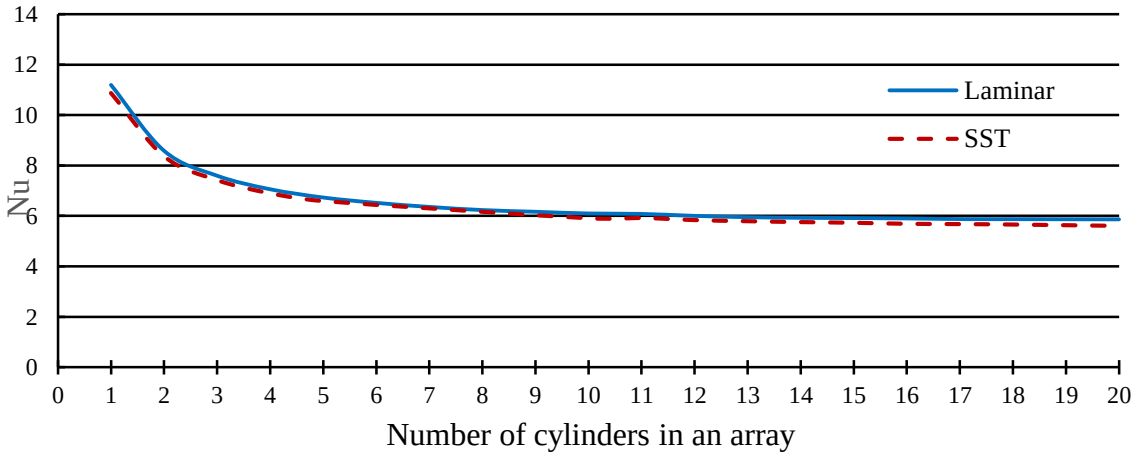


Figure 2.7 Array-average Nusselt numbers for Re = 500.

Figures 2.7 and 2.8 correspond to Reynolds numbers of 500 and 600. For the most part, these figures continue to support the laminar model. The small deviations for the one-cylinder array are acceptable. They may reflect the initial turbulence level of 5% that was assigned to the inlet flow for the SST model.

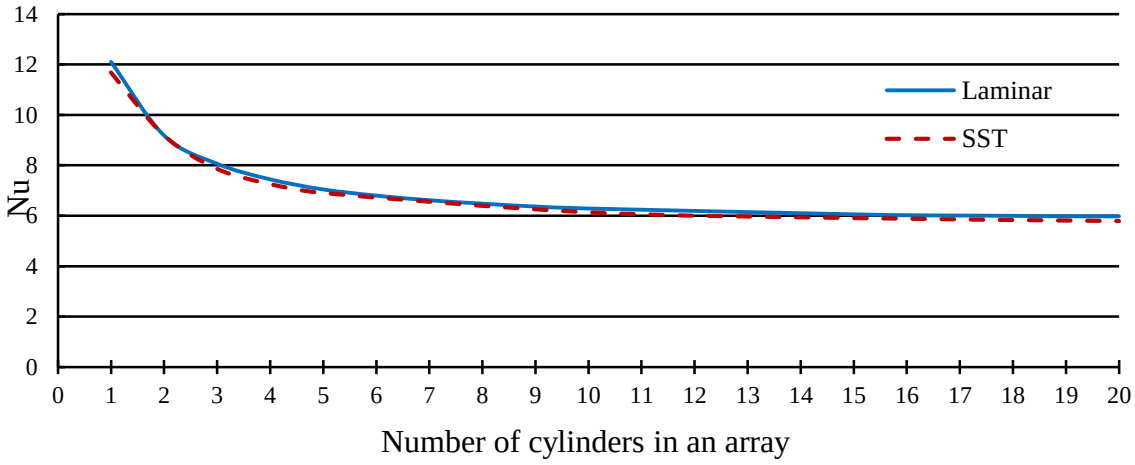


Figure 2.8 Array-average Nusselt numbers for Re = 600.

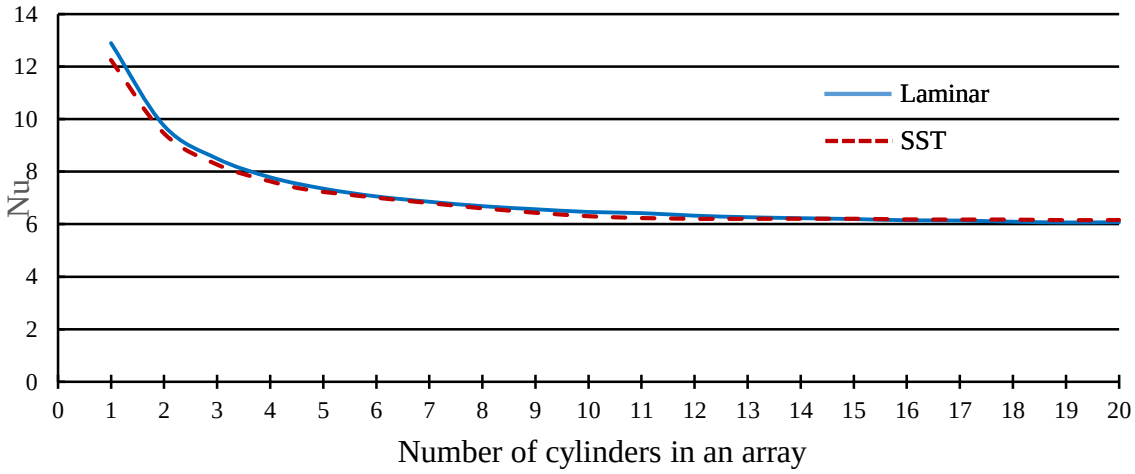


Figure 2.9 Array-average Nusselt numbers for Re = 700.

The last three Reynolds numbers to be considered are 800, 900, and 1,000. Results for these cases are displayed in Figures 2.10, 2.11, and 2.12. Inspection of these figures shows substantial deviations between results for the laminar case and those for the SST turbulence model. It is believed that the deviations seen in these figures indicates that the laminar model is no longer acceptable. Therefore, it may be concluded that the laminar flow persists up to Reynolds number of 700 and not beyond.

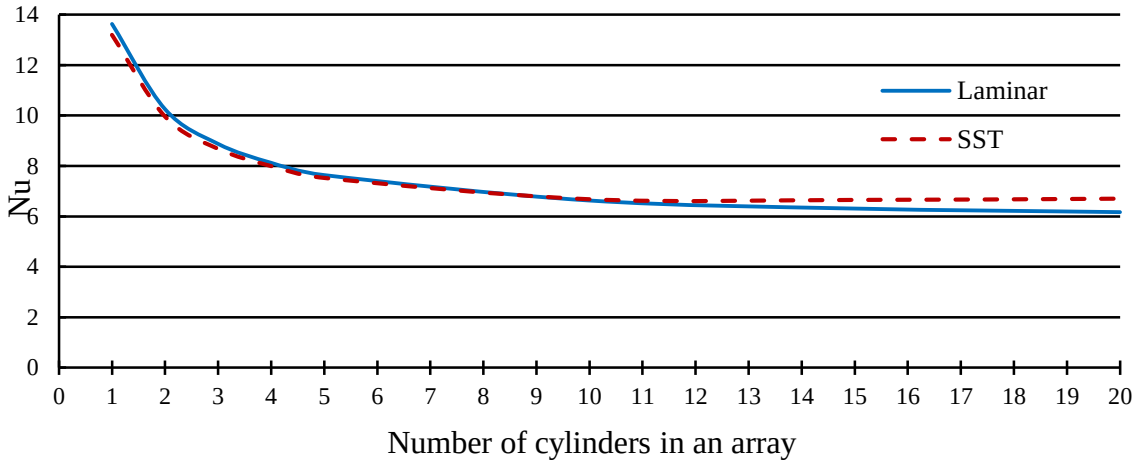


Figure 2.10 Array-average Nusselt numbers for Re = 800.

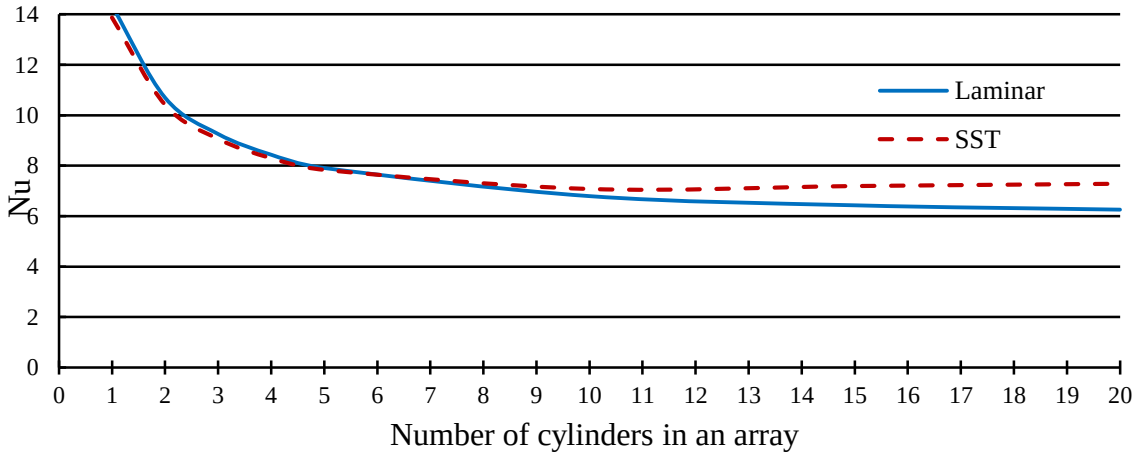


Figure 2.11 Array-average Nusselt numbers for Re = 900.

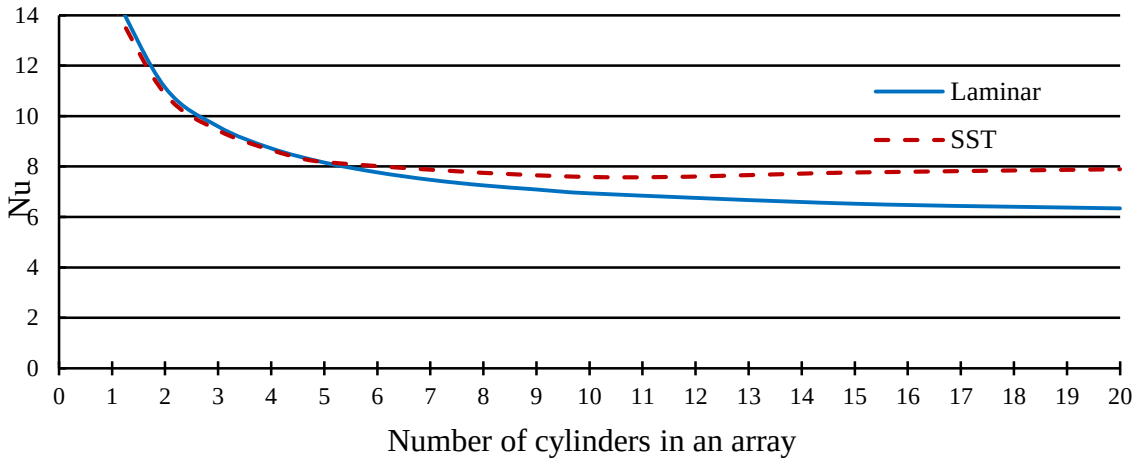


Figure 2.12 Array-average Nusselt numbers for Re = 1,000.

### 2.4.2 Ratio of $\mu_{turb}/\mu$ as a marker for the flow regime

As an alternative means for sorting out the issue of the flow regime, values of $\mu_{turb}/\mu$ have been calculated for the SST solutions for each of the Reynolds numbers of interest. This information is presented in the forthcoming figures, starting with Figure 2.13 for Re = 100 and continuing to Figure 2.16 for Re = 700. The figure corresponds to an array of 10 cylinders (N = 10). Displayed in each figure is a color contour diagram in which the colors correspond to different values of $\mu_{turb}/\mu$. The color strip below the color contour diagram displays the correspondence between the colors and the values of the ratio.

Attention will not be directed to Figure 2.13. For perspective, note that the largest value of the ratio $\mu_{turb}/\mu$ for this figure is 0.005. The figure shows that the largest value of $\mu_{turb}$ is 1/200 of $\mu$, and this value occurs just downstream of the inlet of the array. It is believed that this non-zero value of $\mu_{turb}/\mu$ is the legacy of the 5% value of turbulence intensity that was applied at the inlet of the array.

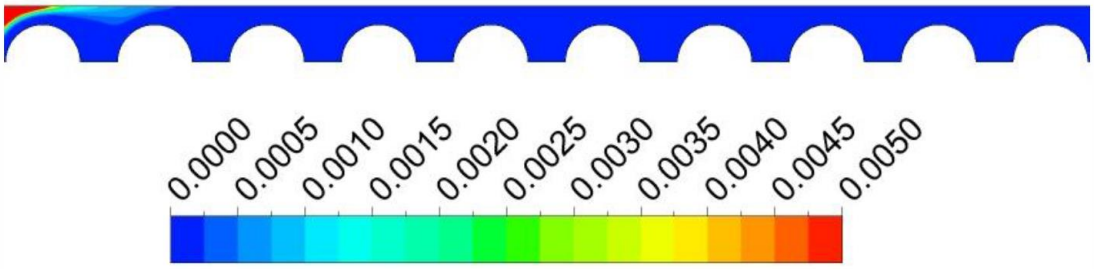


Figure 2.13 Color contour diagram showing the values of $\mu_{turb}/\mu$ for the SST solution for a ten-cylinder array and a Reynolds number of 100. The color strip displays the values of $\mu_{turb}/\mu$.

The next figure in this sequence, Figure 2.14, corresponds to a Reynolds number of 200.

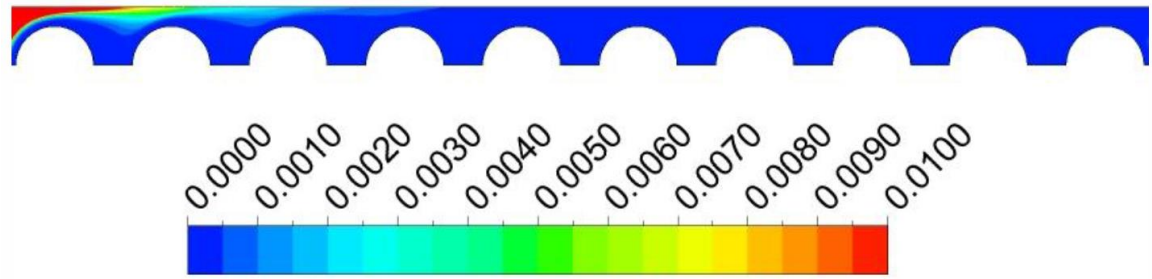


Figure 2.14 Color contour diagram showing the values of $\mu_{turb}/\mu$ for the SST solution for a ten-cylinder array and a Reynolds number of 200. The color strip displays the values of $\mu_{turb}/\mu$.

The only visible change in Figure 2.14 compare to its antecedent is that the maximum value of $\mu_{turb}/\mu$ as shown by the color scale is 0.01 compared with 0.005. This slightly elevated value can be attributed to the lesser damping of the originally assumed initial turbulence intensity of 5%.

The aforementioned trend in which the legacy of the initial turbulent intensity is less damped with increasing Reynolds number continues, as can be seen in Figure 2.15 which corresponds to Re = 500. For this case, the maximum value of $\mu_{turb}/\mu$ is 0.05.

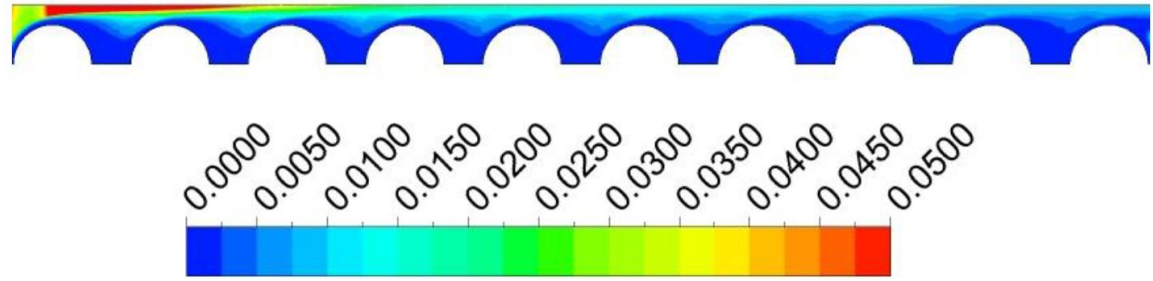


Figure 2.15 Color contour diagram showing the values of $\mu_{turb}/\mu$ for the SST solution for a ten-cylinder array and a Reynolds number of 500. The color strip displays the values of $\mu_{turb}/\mu$.

The last figure in this sequence, Figure 2.16, corresponds to Re = 700. Although there are clearly locations where the viscosity ratio achieves a value as high as 0.2, for the most part, the ratio is lower than 0.1. This outcome suggests that Re = 700 may be regarded as primarily a laminar flow.

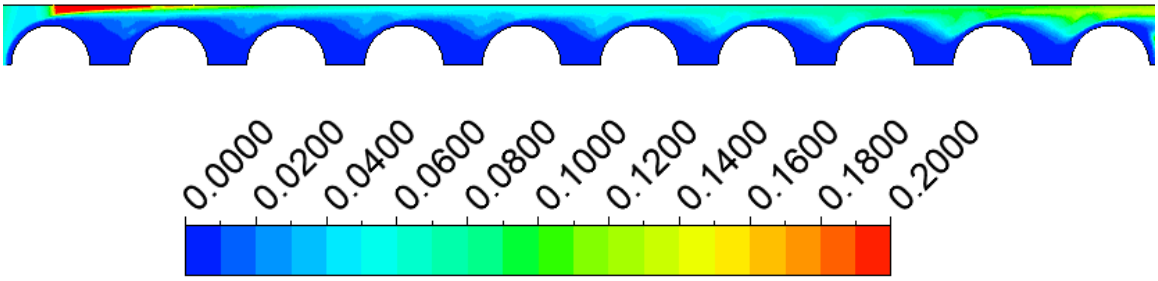


Figure 2.16 Color contour diagram showing the values of $\mu_{turb}/\mu$ for the SST solution for a ten-cylinder array and a Reynolds number of 700. The color strip displays the values of $\mu_{turb}/\mu$.

## 2.5 Values of *Nu* as a Function of the Number of Cylinders that Constitute an Array

From observations made of array-average Nusselt number information in Figures 2.3 to 2.9, it is seen that the array-average Nusselt number becomes independent of the number of the rows beyond a certain threshold. The Nusselt number that is independent of the

number of rows may be termed a *fully developed* value. For design purposes, such fully developed values can be used effectively for arrays whose row number exceeds the threshold value. This information is conveyed in Table 2.1.

Table 2.1 Fully developed laminar Nusselt numbers and the array sizes for which they are applicable.

| Re | $Nu_{fd}$ | Arrays for which $Nu_{fd}$ applies |
|---|---|---|
| 100 | 4.87 | $N \geq 10$ |
| 200 | 5.10 | $\geq 13$ |
| 300 | 5.33 | $\geq 13$ |
| 400 | 5.70 | $\geq 12$ |
| 500 | 5.87 | $\geq 13$ |
| 600 | 5.96 | $\geq 15$ |
| 700 | 6.04 | $\geq 16$ |

The information conveyed in Table 2.1 covers the range from Re = 100 to 700. It is interesting that the dependence of $Nu_{fd}$ on the Reynolds number is moderate. Since, according to Figures 2.3 to 2.9, the array-average Nusselt numbers approach their fully developed value asymptotically. In this light, the exact array population where fully developed conditions occur is somewhat uncertain. To eliminate this uncertainty, the array number for which the average Nusselt number is 1.02 times the fully developed value has been identified and is listed in Table 2.1.

A graphical representation of the fully developed array-average Nusselt numbers are plotted in Figure 2.17 as a function of Reynolds number. Both Table 2.1 and Figure 2.17 demonstrate a moderate dependence of $Nu_{fd}$ on Reynolds number.

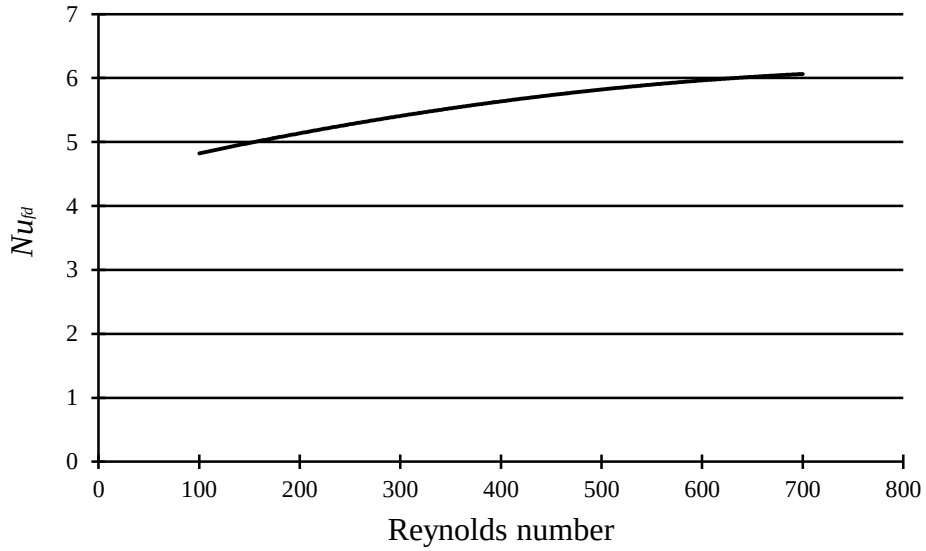


Figure 2.17 Dependence of fully developed array-average Nusselt number on Reynolds number.

More detailed information about how the array-average Nusselt number varies with the number of rows in the array will now be presented. This presentation was influenced by information in the heat exchanger literature [4, 5]. These references report experimental work performed in the early 1950s. The information from [4, 5] is reproduced in Table 2.2.

Table 2.2 Ratio of the average heat transfer coefficient for an array of N cylinders compared with the average heat transfer coefficient for a 10-cylinder array for turbulent flow [4, 5].

| Ratio $\bar{h}_{cN}/\bar{h}_c$ | N = 1 | 2 | 3 | 4 | 5 | 6 | 7 | 8 | 9 | 10 |
|---|---|---|---|---|---|---|---|---|---|---|
| In-line tubes | 0.64 | 0.80 | 0.87 | 0.90 | 0.92 | 0.94 | 0.96 | 0.98 | 0.99 | 1.0 |

Although the table purports to be comparing the array-average heat transfer coefficient for an N-cylinder array with that for a 10-cylinder array, which is actually not the case. The experimental technique involved a transient method in which only a single cylinder

in the entire array was thermally active. All the other cylinders were fluid mechanically but not thermally involved. Such approach cannot take account of the heating of the flowing fluid by contact with cylinders situated upstream of the thermally active positions as would occur in reality. It is difficult to rationalize the use of these data as array-averages.

Even though the tabulated information is purported to correspond to turbulent flow and the present investigation is focused on laminar flow, the trends shown in the table merit careful consideration here. Of greatest concern to the writer is that the lowest value of the purported array-average heat transfer coefficient occurs for the array having the least number of cylinders and that the array-average increases as number of cylinders in the array becomes greater. There are many analogous situations encountered in heat transfer experience that display a trend opposite to that of Table 2.2. The most-encountered situation is heat transfer in a pipe. In that case, it has been established beyond doubt that the highest heat transfer coefficient occurs at the inlet of the pipe, and that the magnitude of the coefficient decreases steadily with increasing downstream distance. The same trend is encountered for boundary layer flow where the maximum value of the transfer coefficient occurs at the leading edge of the plate and decreasing values occur monotonically with distance along the plate.

The low magnitudes of the heat transfer coefficient near the inlet of the array were attributed by the author of [4, 5] to turbulence level. It was postulated that the fluid entering the array possessed a moderate but unknown turbulence level, and that the turbulence level increased as fluid passed downstream, encountering the walls of the bounding cylinders. This explanation would appear to be more reasonable if the flow were occurring in an array of staggered cylinders, but appears less likely to be valid for the case of in-line cylinders. Since the inlet value of turbulent intensity for the experiments of [4, 5] was unknown, the information displayed in Table 2.2 is best regarded as qualitative.

Another relevant piece of information from the literature is exhibited in Figure 2.18 which has been copied from [6]. That figure purports to give a correction factor to account for the difference in the values of the array-average heat transfer coefficients for an N-row array and a 20-row array. The figure conveys results for both in-line and staggered arrays. The Reynolds number range is subdivided into two parts: 100 to 1,000 and > 1,000. According to the figure, for the low Reynolds number range (< 1,000), there is no dependence of the array-average heat transfer coefficients on the number of rows for in-line arrays. This outcome is contrary to the results of the present investigation as set forth in Figures 2.3 to 2.9. In Section 2.4.2, it was shown that for Reynolds numbers up to 700, turbulence is not a factor and that the flow regime is laminar. Therefore, any arguments having to do with changes in turbulent intensity are irrelevant.

If each of the participating cylinders has the same uniform surface temperature, then logic dictates that the successive cylinders will experience a trend of monotonic decreasing heat transfer rate. On the other hand, the fluid bulk temperature must increase in the direction downstream from the array inlet. These facts are believed to be irrefutable proof that the array-average heat transfer coefficient cannot be a constant.

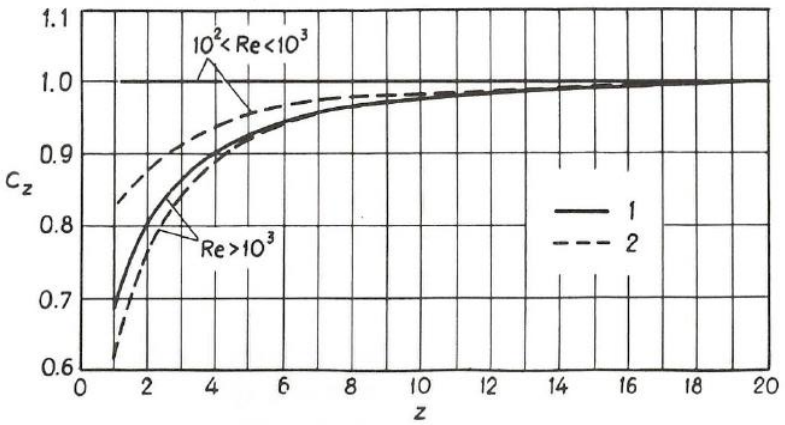


Figure 2.18 Correction for the number of rows in the heat transfer calculations of banks. (1) in-line and (2) staggered [6]. The quantity z is the number of rows in the array.

## 2.6 Continuity of Transient and Steady State Solutions

In [2], it was found that when the adopted fluid flow model was turbulent, a start-up transient solution did not converge to a steady state. This issue will be explored here for the laminar flow model which is the basis of the present investigation. The issue will be examined from two points of view: (a) qualitative nature of the flow field and (b) quantitative comparison of array-average Nusselt numbers.

For the qualitative investigation, attention was directed to an intermediate Reynolds number that has been demonstrated to be strictly laminar, Re = 500. An array consisting of 10 rows of tubes was used in demonstration. For the transient situation, an initial condition of zero velocity throughout the entire array was imposed. Figure 2.19 displays a succession of color contour diagram depicting the velocity field, with each diagram corresponding to an increasing value of dimensionless time starting with time = 0. Inspection of the successive diagrams displays an orderly progression of temporal flow development. It can be seen by comparison of diagram (f), dimensionless time equal to 19.60 with the steady state flow field displayed in diagram (g) that steady state is actually achieved at that value of the dimensionless time.

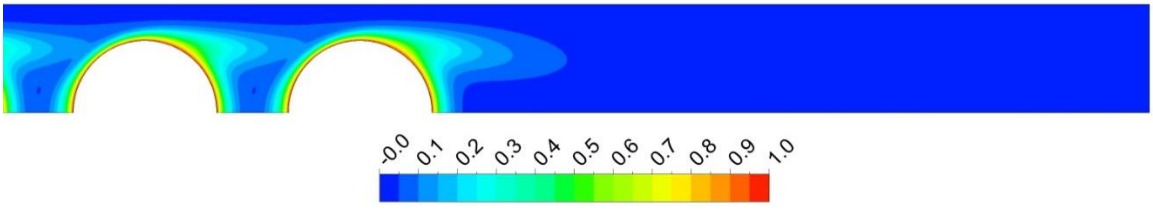


Dimensionless temperature

(a) $Ut/D$ = 0.65

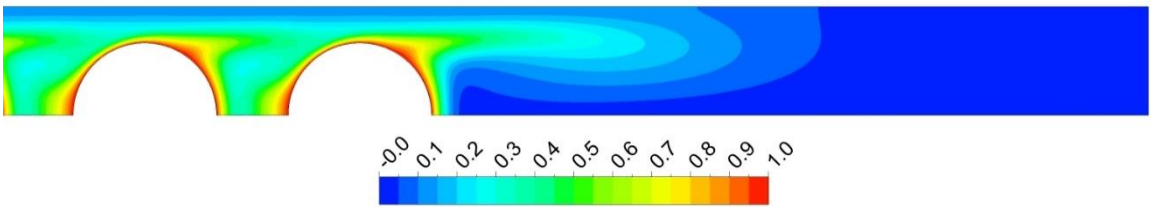


Dimensionless temperature

(b) $Ut/D$ = 1.96

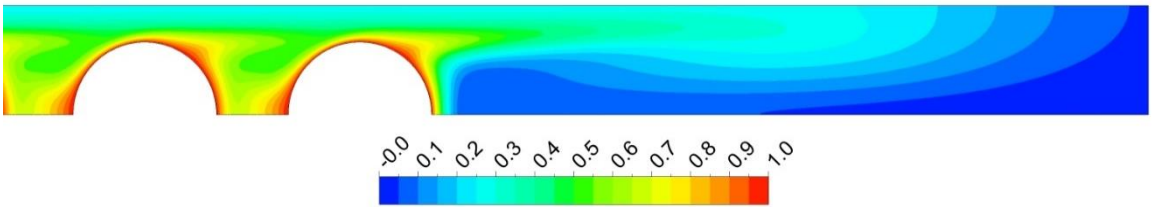


(c) *Ut/D* = 3.27

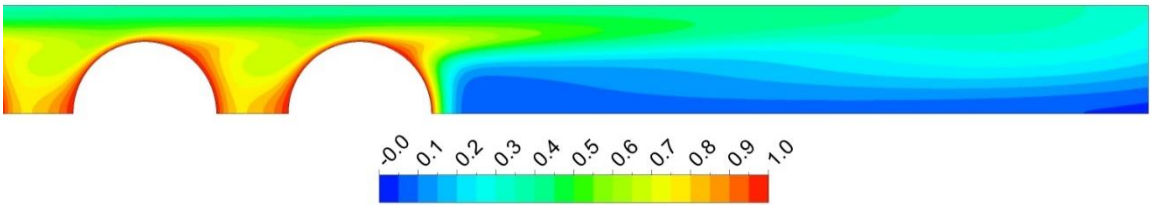


(d) *Ut/D* = 4.57

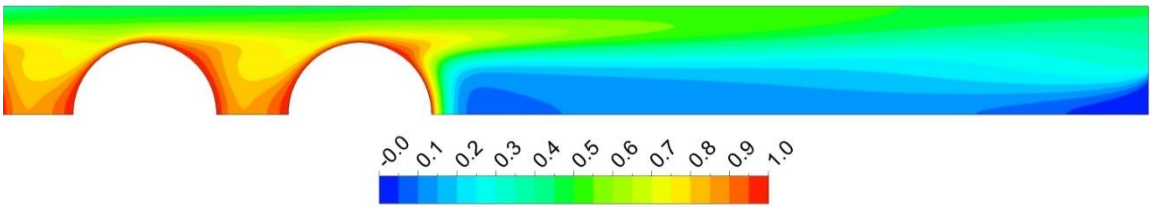


(e) *Ut/D* = 5.88

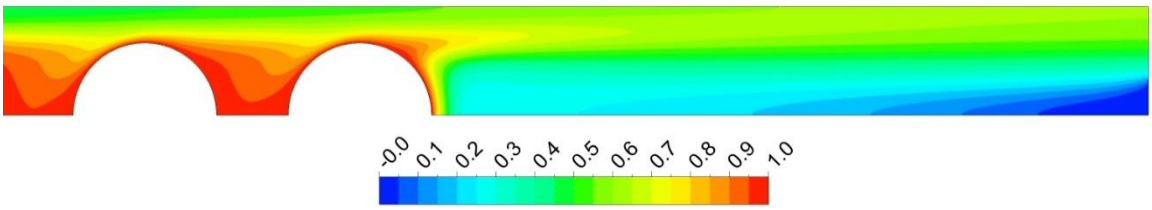


(f) *Ut/D* = 19.60

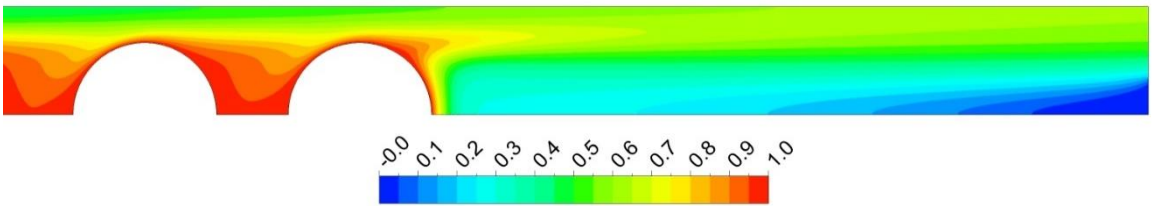


(g) Steady state solution

Figure 2.19 Development of the flow field during a start-up transient and comparison with the steady state. Re = 500 for a 10-row array.

The qualitative display of Figure 2.19 will not be supplemented by a quantitative comparison between results from the start-up transient solution and that for the steady state. This comparison, exhibited in Figure 2.20, is for a 10-row array and Re = 500. In the figure, the array-average Nusselt number is plotted as a function of dimensionless time. For the steady state case, the Nusselt number is, of course, independent of time.

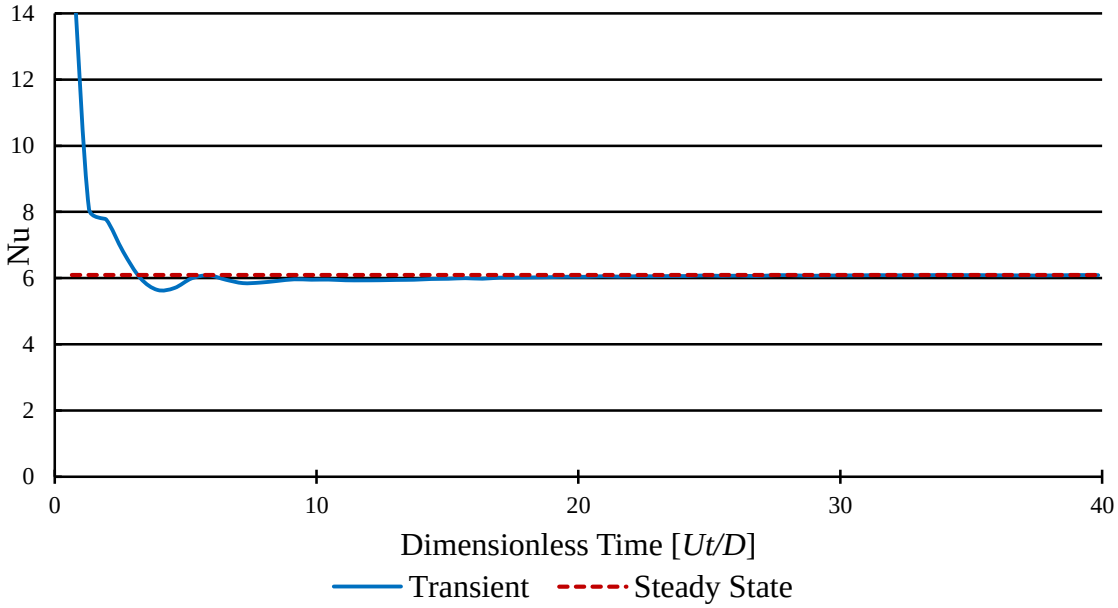


Figure 2.20 Quantitative demonstration of the convergence of the start-up transient to a steady state. Re = 500 for a 10-row array.

Inspection of the figure shows that for dimensionless times greater than approximately10, steady state clearly established with respect to the Nusselt number.

## 2.7 Examination of the Symmetry Assumption

In the setup of the numerical simulation, it was found advantageous to use all possible geometrical symmetries. The underlying reasons for aforementioned advantage is that when the size of the solution domain is very compact, the nodal allocation can be used very effectively with respect to accuracy and solution time. On the other hand, others (for example, [3]) have questioned whether the imposition of symmetry does not enable the solution to follow its own path which might not lead to the geometric symmetry. To explore this issue, two different solution domains were used for the same array and Reynolds number, and the results compared with respect to symmetry.

The two solution domains consider for this demonstration are respectively displayed in Figures 2.21 and 2.22. In the first of these figures, the upper half of a column of cylinders which constitute the array are displayed. The upper and lower bounding lines of this solution domain are symmetry lines. Figure 2.22 defines a full column of cylinders, with upper and lower boundaries being symmetry lines. Note, however, the symmetry lines for Figure 2.21 are different from those for Figure 2.22.

Figure 2.21 Minimum-sized solution domain.

Figure 2.22 Solution domain of Figure 2.21 doubly enlarged.

The results obtained from the solutions based on this solution domains will be compared both on a qualitative and a quantitative basis. The qualitative comparison is based on inspection of the respective temperature fields obtained for the two geometric models. The domain-specific temperature field results are displayed in Figures 2.23 and 2.24. A

very careful inspection of the two figures offers convincing evidence that the solutions that correspond to the different symmetry assumptions are identical.

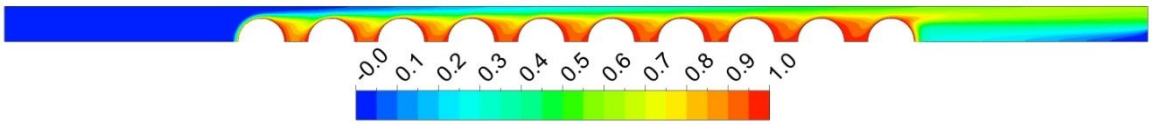


Figure 2.23 Temperature field for a simulation model that utilizes the solution domain of Figure 2.21. Results are for a 10-row array and a Reynolds number of 500.

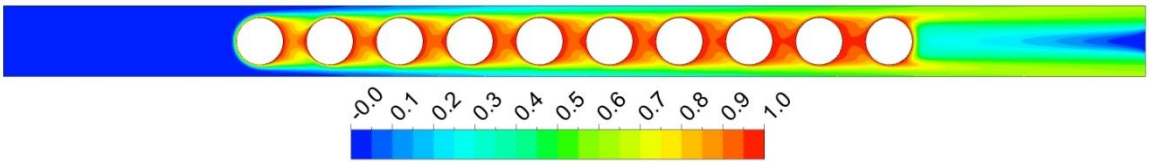


Figure 2.24 Temperature field for a simulation model that utilizes the solution domain of Figure 2.22. Results are for a 10-row array and a Reynolds number of 500.

To effectuate a quantitative comparison of the results of two solution domains, it was deemed appropriate to focus on the array-average Nusselt numbers for a 10-row array with a Reynolds number of 500. Without additional complication, it was possible to make the desired comparison for the transient operating condition which may be regarded as more severe test case. Figure 2.25 has been prepared to display the comparison. The figure shows Nusselt number results for selected times that span both start-up and steady state. The results for the respective solution domains of Figures 2.21 and 2.22 are displayed by means of case-specific data symbols. It is evident from the inspection of Figure 2.25 that the Nusselt number results are independent of the specific symmetry model that was adopted.

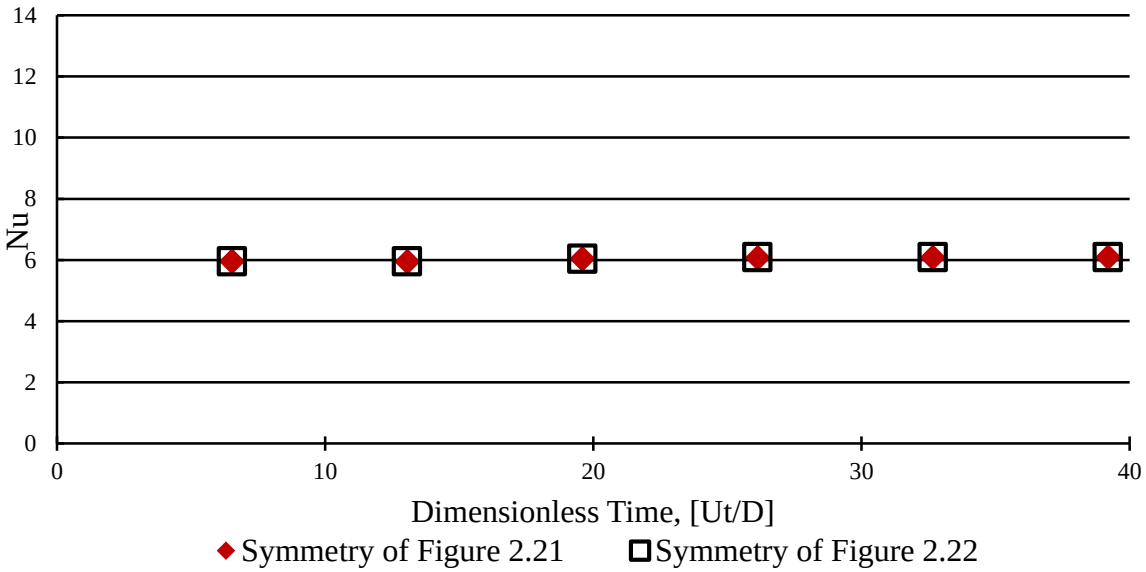


Figure 2.25 Comparison of array-average Nusselt numbers for the symmetry pattern of Figures 2.21 and 2.22. The results correspond to a 10-row array and a Reynolds number of 500.

## 2.8 Pressure Variations

Two types of pressure results have been extracted from the numerical simulations. The first is detailed pressure variations along the upper and lower boundaries of the solution domain. The other is the per-row pressure drop as a function of the row number.

The first type is exhibited in Figures 2.26 and 2.27, respectively for Re = 120 and 500. The case of Re = 120 is not one of the mainline cases dealt with in the foregoing; it was run especially for purpose of comparison with the literature. The format of these figures displays the solution domain and focuses on the upper symmetry line and on the lower boundary of the domain which includes the lower symmetry line and the surfaces of the successive cylinders. For generality, the pressure distributions are displayed in dimensionless terms. Specifically, the pressure at the inlet cross section $p_{in}$ is used as a reference quantity, and the difference between $p_{in}$ and the local pressure $p$ is normalized

by $\frac{1}{2}\rho {U_{max}}^2$. The use of $U_{max}$ in the nondimensionalization was prompted in order to facilitate a comparison with the literature.

Attention will first be turned to Figure 2.26. It can be seen from the figure that a repeating pattern of pressure variation exists. Undulations occur fore and aft of each of the cylinders. The lowest pressures occur in zones of highest velocity and pressure recovery takes place as velocities diminish. The pattern of undulations has a unique form at the beginning of the array, but it appears that regularity sets in with increasing downstream distance. This issue will be quantified shortly.

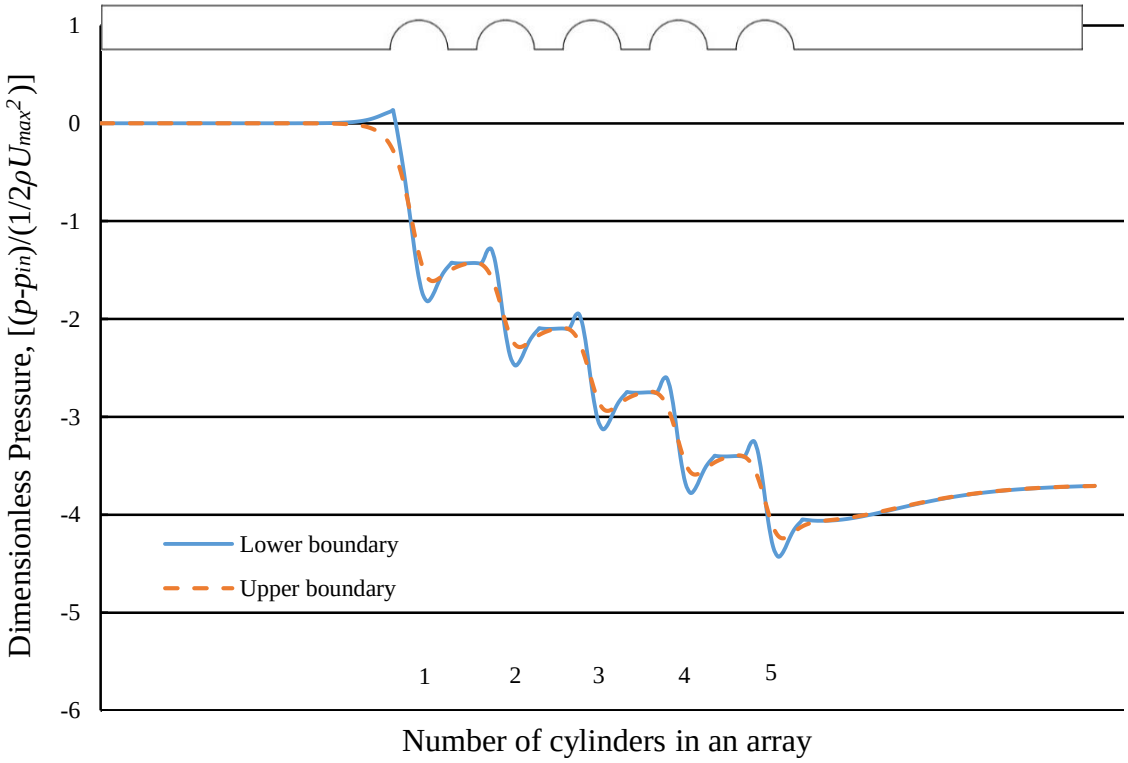


Figure 2.26 Pressure variations along the upper and lower boundaries of the solution domain for Re = 120 for a five-row array.

The next figure, Figure 2.27, is for the mainline Reynolds number of 500 and is for a 20-row array. The general features displayed in this figure are similar to those which were identified in Figure 2.26.

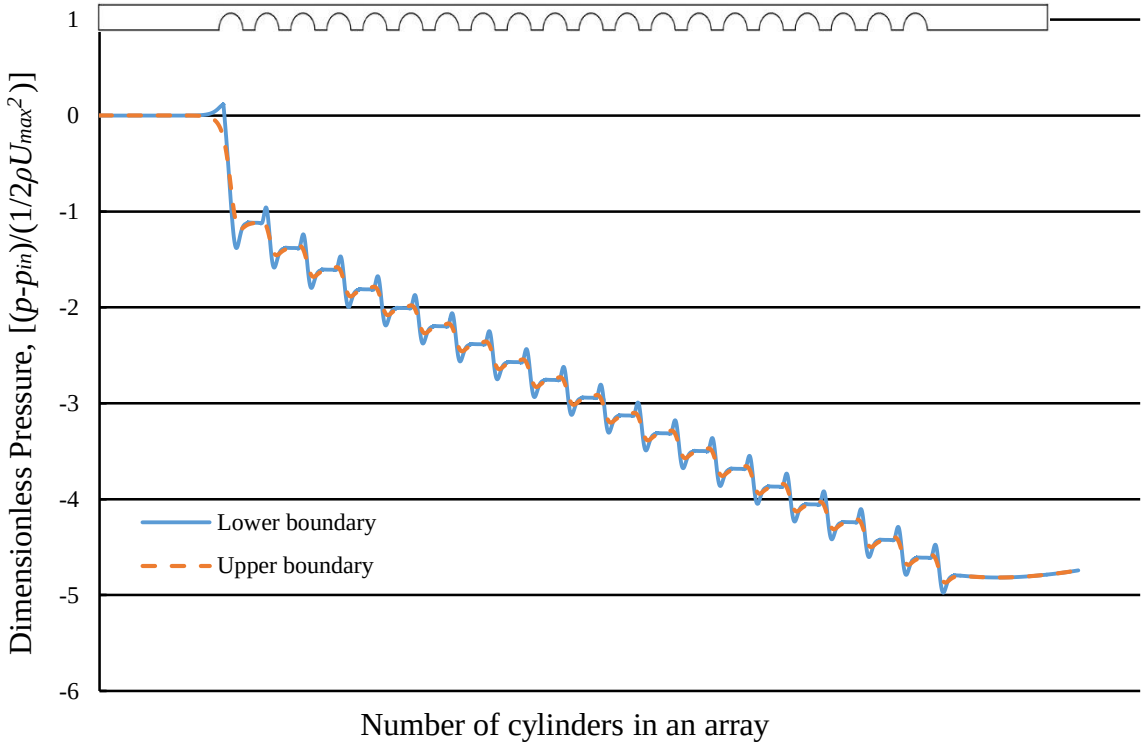


Figure 2.27 Pressure variations along the upper and lower boundaries of the solution domain for Re = 500 for a 20-row array.

The last figure in this series is devoted to a displayed of results obtained by Fujii [8] for the case of Re = 120 and a five-row array. Although Fujii's model for heat transfer can be demonstrated to be erroneous, his pressure drop results are believed correct. This conclusion follows from a comparison of Figures 2.28 and 2.26, respectively due to Fujii and to the present analysis. The clearly good agreement is supported of both investigation.

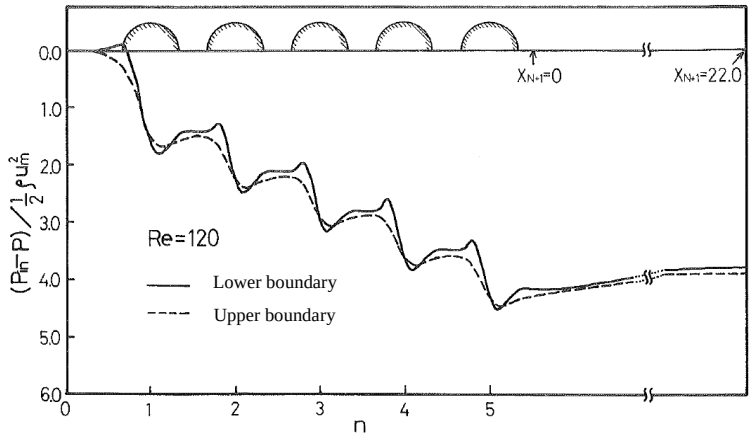


Figure 2.28 Pressure variations along the upper and lower boundaries of the solution domain for Re = 120 for a five-row array from Fujii [8]. The upper boundary is the centerline between tube bank and lower boundary includes along the surface of cylinders.

Focus will now be directed to the presentation of the per-row pressure drops. It is expected, based on the periodicity of the geometry of the array, that the per-row pressure drop will also be repetitive and independent of the row number. Information on the per-row pressure drops is presented in Figures 2.29 to 2.32 for Reynolds numbers of 100, 300, 500, and 700. In each figure, the per-row pressure drop, made dimensionless by $\frac{1}{2}\rho U^2$, is plotted as a function of row number.

For Re = 100, Figure 2.29, it is seen that only at the very beginning of the array is there a departure from constancy of the per-row pressure drop. With increasing values of the Reynolds number, the pre-periodic pressure drop length increases monotonically. For the largest considered Reynolds number, about eight rows are required to obtain per-row pressure periodicity.

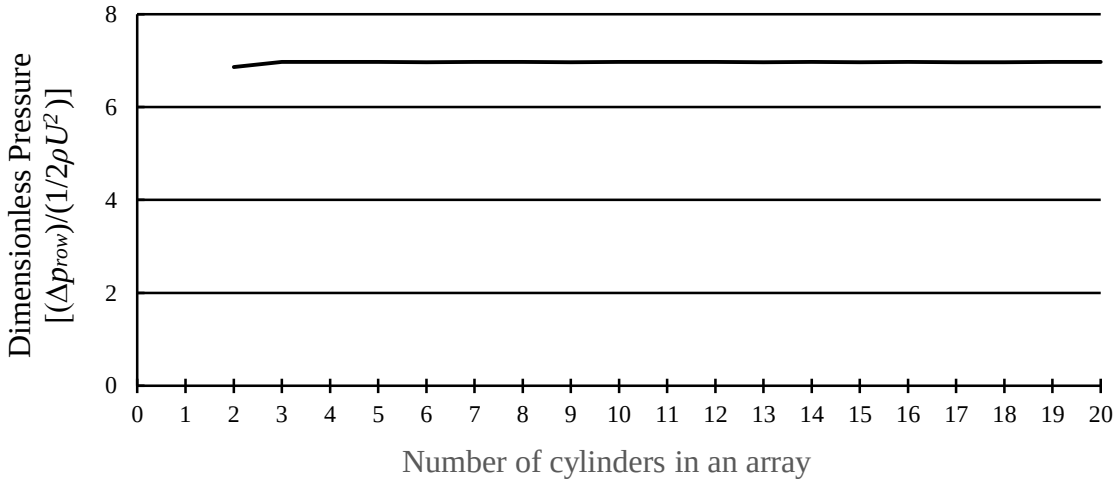


Figure 2.29 Dimensionless pressure drop between two adjacent cylinders in a 20-row array, Re = 100.

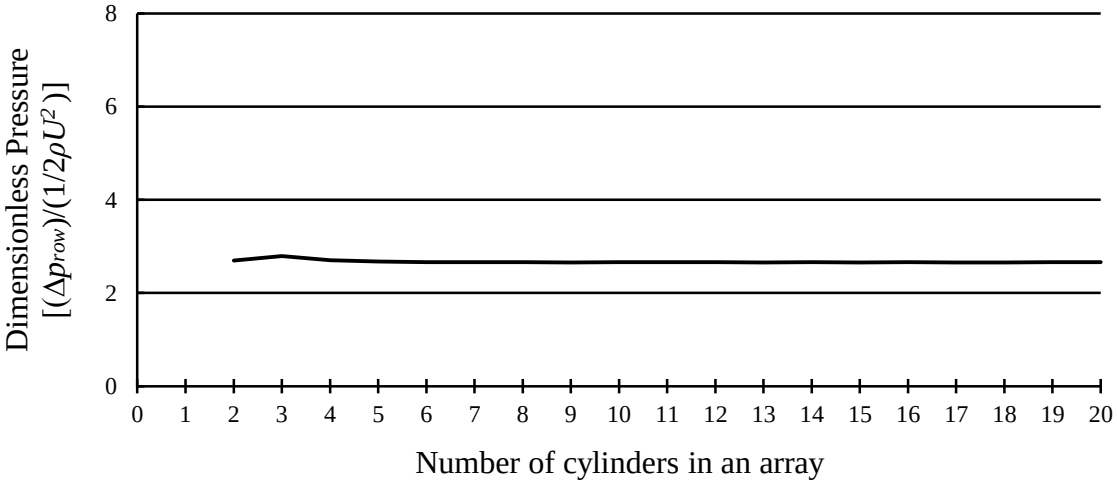


Figure 2.30 Dimensionless pressure drop between two adjacent cylinders in a 20-row array, Re = 300.

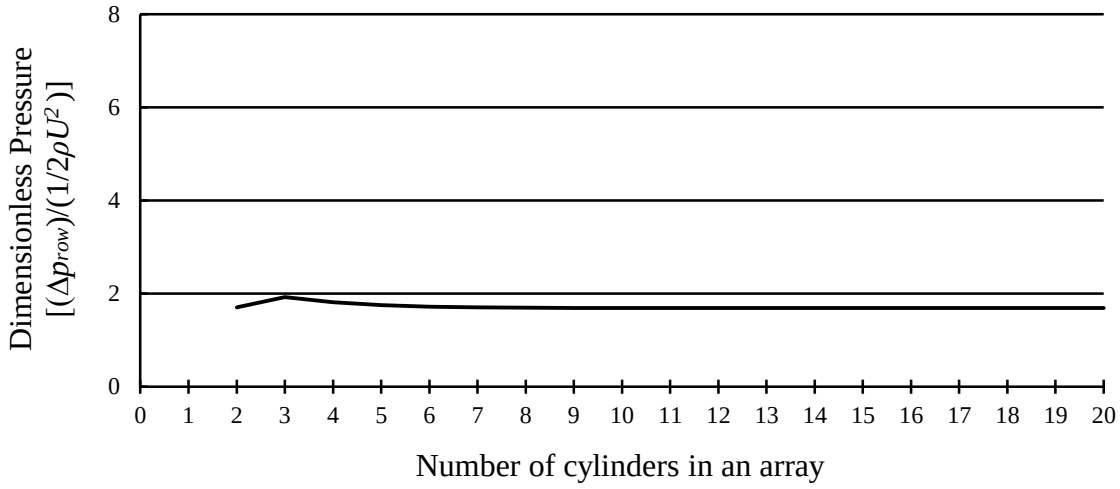


Figure 2.31 Dimensionless pressure drop between two adjacent cylinders in a 20-row array, Re = 500.

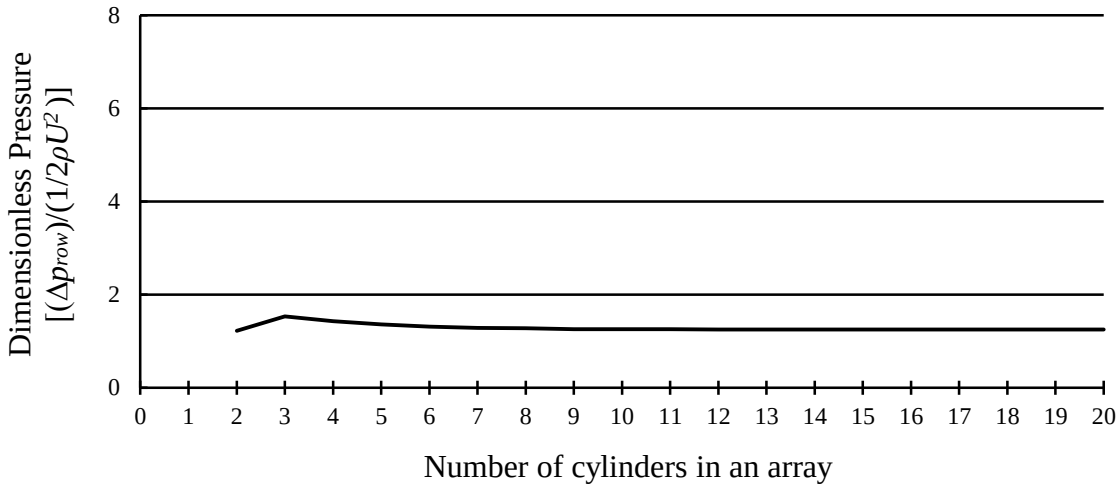


Figure 2.32 Dimensionless pressure drop between two adjacent cylinders in a 20-row array, Re = 700.

The values of the per-row periodic pressure drop information extracted from foregoing figures and others for Re = 200, 400, and 600 have been brought together in Figure 2.33.

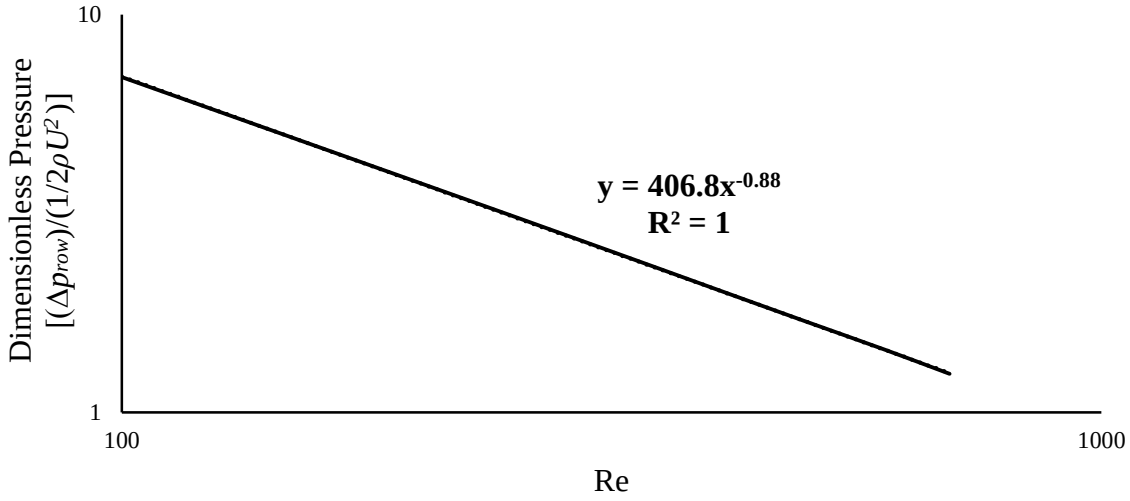


Figure 2.33 Per-row periodic dimensionless pressure drops

Inspection of this figure clearly indicates a linear relationship between the per-row periodic dimensionless pressure drops. The equation extracted from a perfect ($R^2 = 1$) linear fit is

$$\frac{\Delta p_{row}}{\frac{1}{2}\rho U^2} = 406.8\ \mathrm{Re}^{-0.88} \qquad (2.15)$$

Numerical experiments were performed for values of the Reynolds number ranging Re = 100 to Re = 700. In dimensional terms, Equation (2.15) indicates that $\Delta p_{row}$ is proportional to the velocity $U^{1.12}$. Since laminar friction-based pressure drops are directly proportional to the velocity *U*, the exponent contains momentum change contributions to the pressure drop.

## 2.9 Vector Diagram

Insights into the nature of the pattern of fluid flow is conveniently displayed with the aided of vector diagrams. Also relevant is the related discussion of the difficulty in defining a bulk temperature when recirculation zones dominate the flow pattern. Vector diagrams are presented in Figures 2.34 to 2.36 for Reynolds numbers of 100, 400, and 700. Each figure is subdivided into (a) and (b) parts. The (a) part corresponds to the part of the array encompassing the first and second cylinders, while the (b) part pertains to a pair of cylinders situated in the fully developed regime.

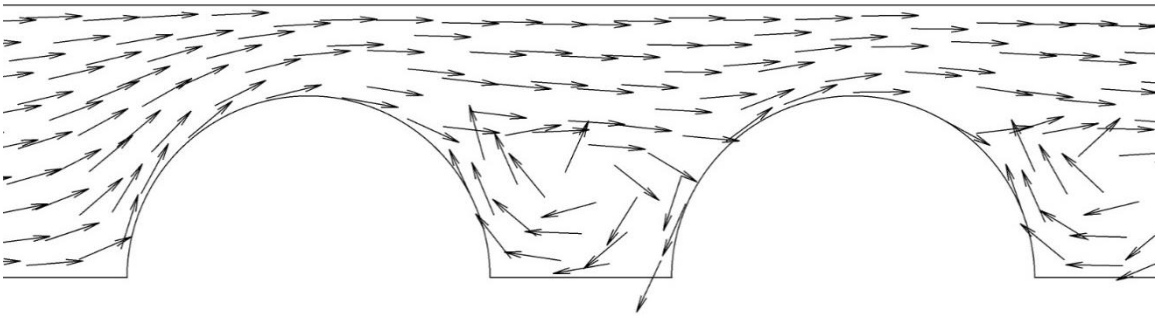

(a) First and second rows

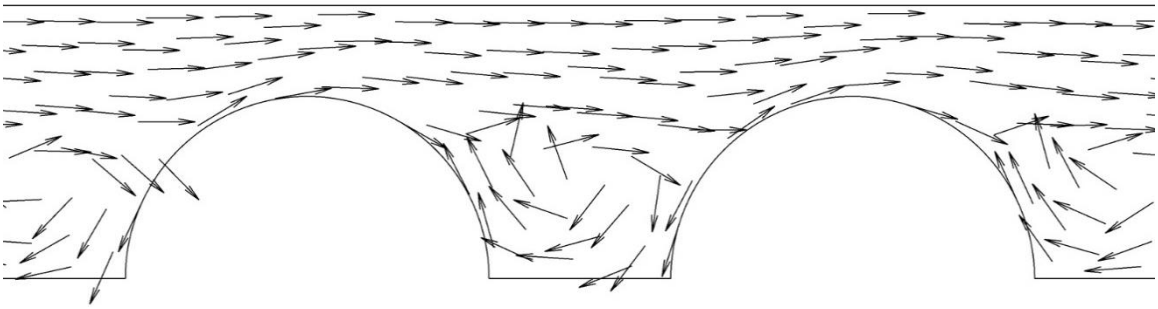

(b) Fully developed regime

Figure 2.34 Vector diagrams for Re = 100. (a) First and second rows; (b) Fully developed regime.

It can be seen from Figure 2.34 that between each pair of consecutive cylinders, there is a vigorous recirculation zone. Such a zone is absent upstream of the first cylinder in the array. It is noteworthy that the recirculation zone at the beginning of the array is hardly

different from that in the fully developed regime. Inspection of Figures 2.35 and 2.36 show the very same patterns as has already been identified in Figure 2.34.

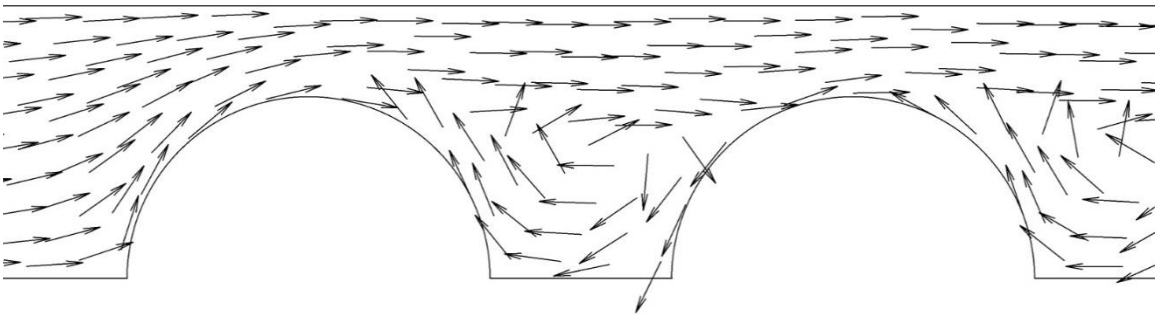

(a) First and second rows

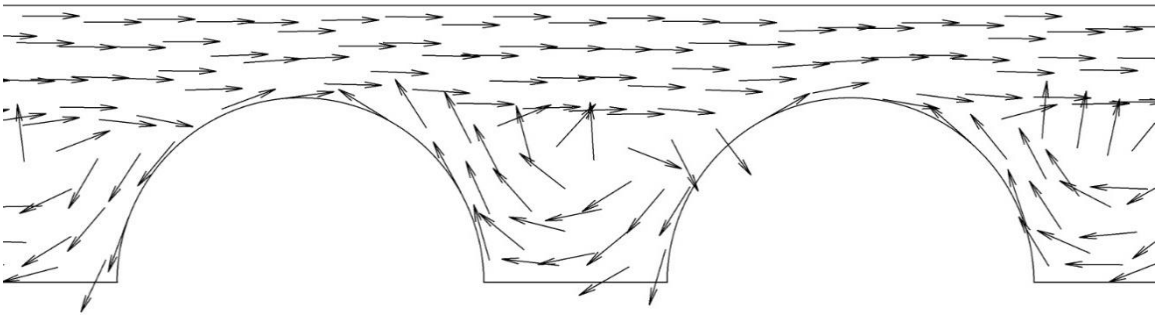

(b) Fully developed regime

Figure 2.35 Vector diagrams for Re = 400. (a) First and second rows; (b) Fully developed regime.

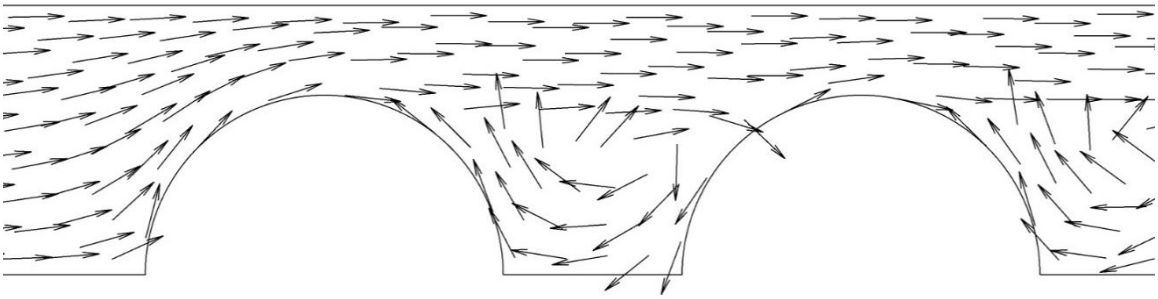

(a) First and second rows

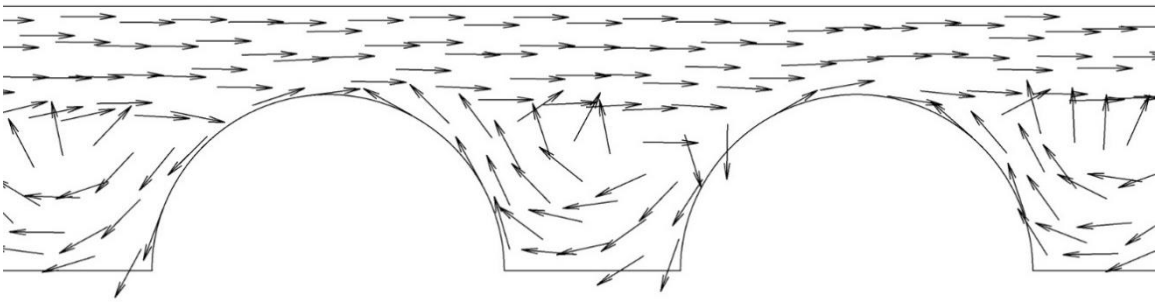

(b) Fully developed regime

Figure 2.36 Vector diagrams for Re = 700. (a) First and second rows; (b) Fully developed regime.

The information displayed in the preceding figures helps to explain the difficulty of finding of rational basis for the definition of the bulk temperature. In the inter-cylinder space, the recirculating fluid exchanges heat with both the upstream and downstream cylinders that define that space. It is very difficult to differentiate between quantities of heat transferred from the respective cylinders to the recirculating fluid. Because of this, it is not possible to identify a bulk temperature either upstream or downstream of a given cylinder.

## 2.10 Streamlines

An alternative view of the pattern of fluid flow is provided by streamlines. Since the primary variations in the flow pattern occur in the rows that are at the upstream end of the array, the streamlines for those rows are the focus of the forthcoming presentation. That presentation is made for Reynolds numbers of 100, 400, and 700 in Figure 2.36 (a)-(c) and is confined to the first four rows of the respective arrays.

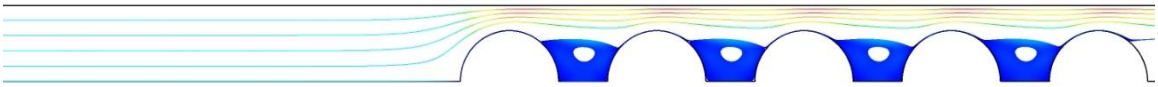

(a) Re = 100

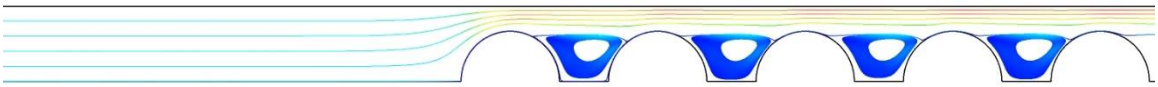

(b) Re = 400

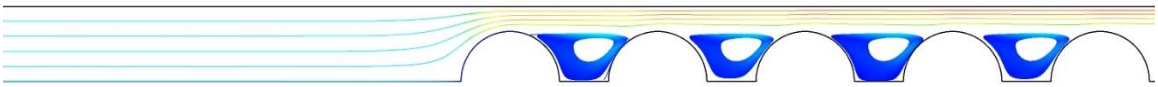

(c) Re = 700

Figure 2.37 Streamlines up to four rows from the upstream end.

The striking feature of the streamline display is the dual personality of the flow. One portion of the flow consists of captured eddies whose fluid inventory is confined forever to the inter-cylinder spaces. The other portion is a throughflow which serves to drive the rotational motion of the captured eddies. The two portions of flow interact along a certain streamline which bounds the throughflow from below and the captured eddy from above.

The general nature of the aforementioned flow pattern is not affected by the Reynolds number. There is a slight Reynolds number influence seen from observation of the lowermost throughflow streamline. That streamline tends to dip more deeply into the inter-cylinder space at the lowest Reynolds number than at the higher Reynolds number.

This behavior can be attributed to the fact that the streamwise momentum is lowest at the lowest Reynolds number and increases as the Reynolds number becomes larger. It can be expected that the larger streamwise momentum, the less will the streamline dip.

## 2.11 Concluding Remarks

The investigation reported in this chapter is noteworthy for its in-depth nature and for the breadth of the issues explored. A summary of accomplishments of the chapter will now be presented.

(a) The nature of the flow regime, laminar versus turbulent, was evaluated by means of two independent approaches.
   (i) Compared predicted heat transfer coefficients from a laminar model and a turbulent model
   (ii) Determined magnitude of the turbulent viscosity relative to the laminar viscosity

(b) Determined the array-average Nusselt numbers for arrays of different numbers of cylinders

(c) Identified the array population that gives rise to Nusselt numbers that are independent of the population. This determination provides a means of defining a fully developed regime.

(d) Demonstrated that shorter array gives rise to higher array-average Nusselt numbers than do longer arrays

(e) Demonstrated that for laminar flow, in contrast to turbulent flow, start-up flow transients do converge to steady state

(f) Showed that geometric symmetry prevails for different symmetric models of the solution domain

(g) Variation of pressure as a function of location in the array demonstrated the influence of velocity accelerations and decelerations.

(h) Showed that after the initial rows of the array, the per-row pressure drop became constant, indicating flow periodicity

(i) Flow visualization was accomplished by means of vector diagram and streamline patterns. The flow was shown to be two-faced in that it consisted of a throughflow stream and a succession of captured eddies.

# CHAPTER 3

## COMPARISONS WITH EXPERIMENTAL DATA

### 3.1 Introduction

There is an unwritten rule that numerical simulations should be validated by experimental data. On the other hand, it is necessary that access to a laboratory is available to perform the experimentation. In this regard, the construction in progress in the Mechanical Engineering building has resulted in the closure of many laboratories, so that it was not possible to perform the necessary experiments during the duration of this thesis.

As an alternative, it was decided to make use of the results of other experiments performed in our laboratories. Specifically, data collected by Sparrow, Ramsey and Altemani [13, 14] in 1978-1980 were used for validation. Those experiments pertained to an array of in-line and staggered wall-attached cylinders (pin fins) with tip clearance. Measurements were made of pressure distributions and mass transfer. The mass transfer was implemented by the naphthalene sublimation technique. Because of the innate limitations of that technique, only a single pin fin was able to participate in a given mass transfer experiment.

A photograph of the experimental apparatus is displayed in Figure 3.1. As can be seen in the figure, the pin fins were situated in a flat-rectangular host duct. An alternative view of the apparatus is shown in a schematic diagram in Figure 3.2. It can be seen from the diagram that there is a long flow development length between the inlet cross section and the forward edge of the array. This length was allowed to provide a well-defined velocity profile at the beginning of the array.

Figure 3.2 represents one of the two investigated geometries. The one shown in the figure

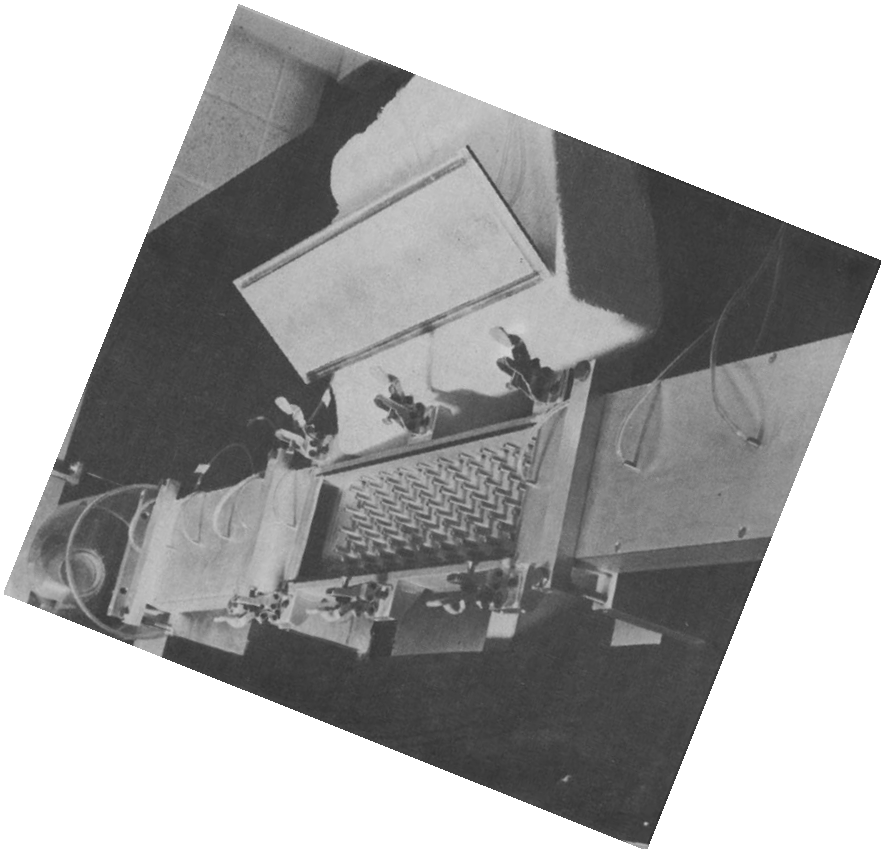

Figure 3.1 Photograph of the experimental apparatus showing the pin-fin array.

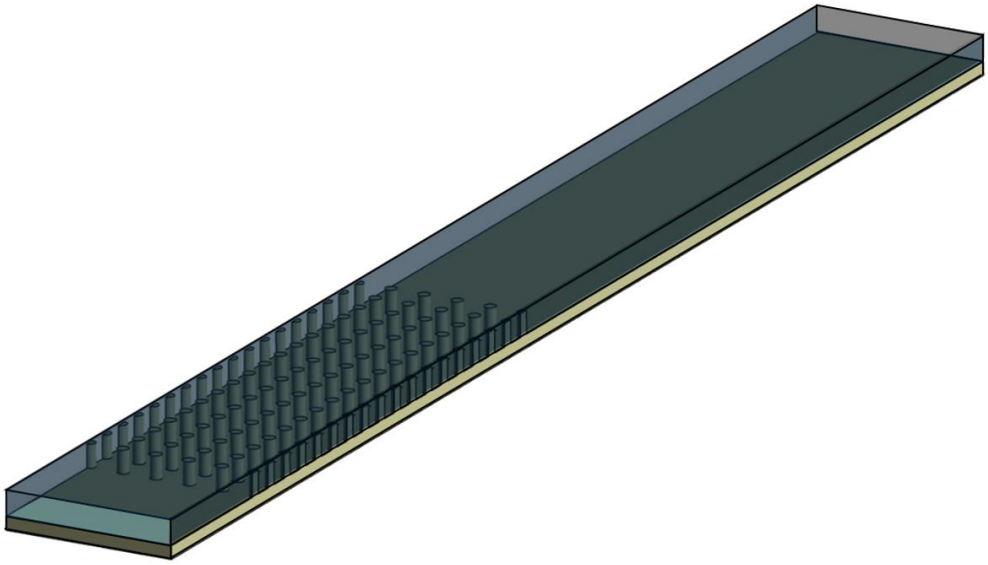

Figure 3.2 Schematic diagram of the experimental apparatus. Air enters at the right end and exits at the left.

draws air directly from the laboratory through the inlet cross section. That configuration necessarily allows the wall thickness of the duct to affect the nature of the inlet velocity profile. In particular, air is drawn into the inlet from both the spaces upstream and to the side of the duct. To avoid the inflow from the side, a large circular plate of radius equal to three feet was fitted to the inlet cross section by means of a rectangular cutout into which the duct was inserted so that the forward edges of the duct wall were precisely co-planar with the forward face of the baffle plate. Separate experiments were performed for both the inlet geometric configurations.

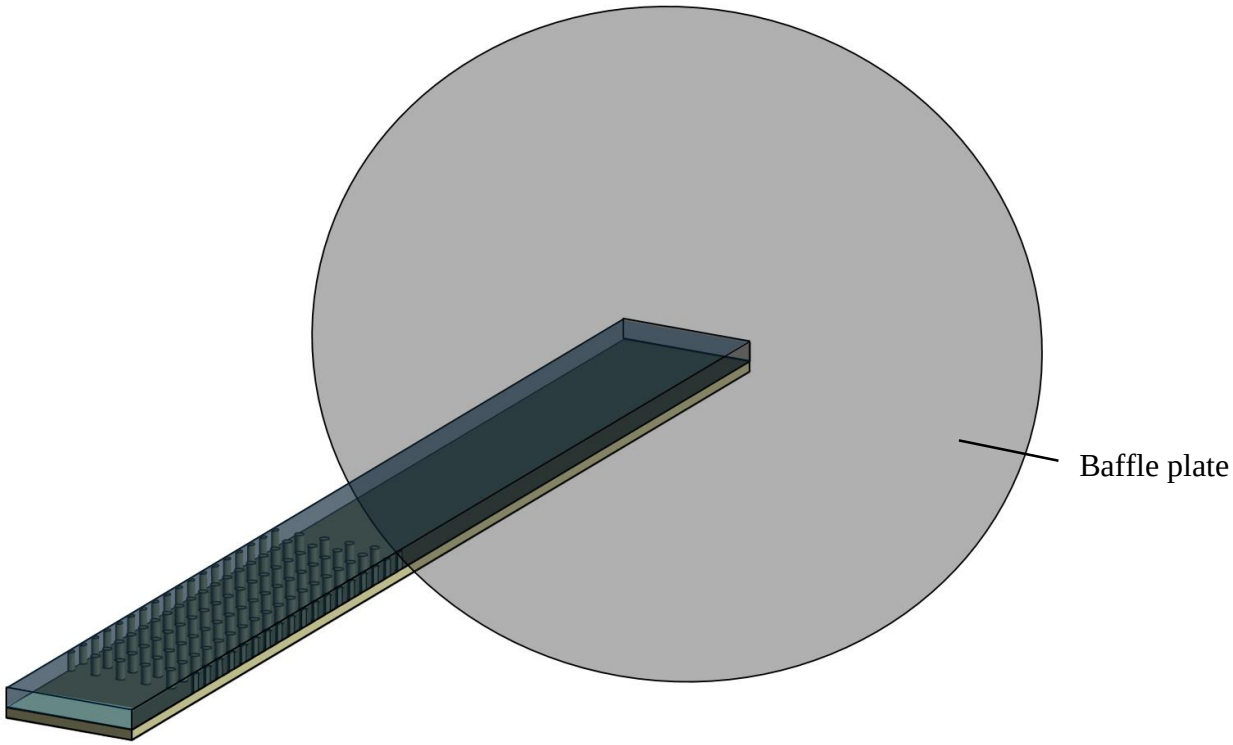


Figure 3.3 Schematic diagram of the experimental apparatus with a baffle plate.

Each of the two inlet configurations are expected to give rise to unique flow separation patterns. In the absence of the baffle plate, some portion of the air that is drawn into the inlet cross section attempts to execute **U**-turn. Such turns are only possible when the fluid Reynolds number is very small. At normal Reynolds numbers, such a turn will give rise to a separation region adjacent to the wall of the duct just downstream of the inlet cross

section. With the baffle in place, the need for a U-turn is eliminated, but some portion of the air that enters the duct executes a $90^o$ turn. Such a turn is also very difficult for a fluid to accomplish, and flow separation is a normal process.

The dimensions of the experimental setup, taken from [13, 14] are listed in Table 3.1 below.

Table 3.1 Dimesions of the host duct and the pin-fin array.

| Component | Dimension or ratio |
|---|---|
| Fin diameter [D] | 7/32 in. = 0.2188 in. |
| $S_T/D$ | 3 |
| $S_L/D = (\sqrt{3}/2)\times(S_T/D)$ | 2.6 |
| Fin height [h] | 7/16 in. = 0.4375 in. |
| Duct cross section | 3.25 in. × 0.75 in. |
| Hydraulic diameter [$D_h$] | 1.22 in. |
| Overall length | 68 in. |

$S_T$ is the transverse center-to-center distance, and $S_L$ is the longitudinal center-to-center distance. The quantity $D_h$ is the hydraulic diameter of the unobstructed duct.

## 3.2 Governing Equations and Numerical Simulations

In order to enhance the value of the validation efforts, the governing equations and turbulence model used for the numerical simulations to be performed for the physical situation defined in the foregoing section are the same as those used for all the other simulations reported in this thesis. The governing equations are Equations. (2.1) through (2.6). In addition, the SST turbulence model used elsewhere in this thesis is also used here.

For the case where the baffle plate is absent, 11 million nodes were used for the

numerical simulations. With the baffle plate in place, the nodal count was 17 million.

The numerical solutions were confined to the velocity problem and related results. The mass transfer experiments was regarded as incomplete and unrealistic because only one pin fin in the entire array participated in the mass transfer process.

## 3.3 Result and Discussion

### 3.3.1 Results from the experiments of [14]

As a starting point for the presentation of results, it is appropriate to display the pressure distribution data from [14], and this information is shown in Figure 3.4. These data correspond to an array Reynolds number of 3,350, where $Re_{array}$ is the array-based Reynolds number: $Re_{array} = \rho U_{max} D/\mu$, where $U_{max}$ is the maximum velocity in the array, and D is the pin-fin diameter.

Figure 3.4 Experimental pressure distribution data from [14]. With the baffle plate in place.

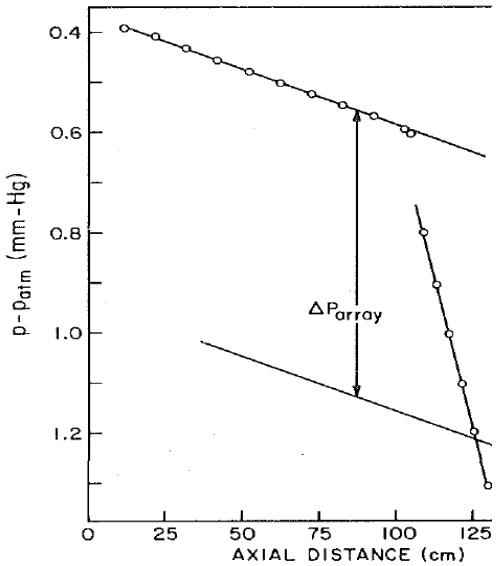


Experimental axial pressure distribution, $h/D$ = 2, $Re_{array}$ = 3,350, $Re_{duct}$ = 15,000.

As can be seen from the figure, the data naturally separate themselves into two groupings, the first group is for the flow in the velocity development region, and the second is for the

pin-fin array. In each grouping, it can be observed that the data fall almost precisely on a straight line, indicating the establishment of fully development flow. The displayed data were obtained with the baffle plate at the duct inlet in place.

### 3.3.2 Comparison of the numerical-simulation results with the experiments

The numerical simulations were performed both with and without a baffle plate at the inlet of the duct. For both cases, the duct Reynolds number ($Re_{duct}$) was equal to 15,000, where $Re_{duct} = \rho U_{duct} D_h/\mu$. It is worthy of note that a duct Reynolds number of 15,000 is perfectly congruent with an array Reynolds number 3,350.

The predicted pressure distributions for the no-baffle case are displayed in Figure 3.5 by red data symbols. Hereafter, this case will be identified as the *baseline case*. For the velocity development portion of the duct, the predicted pressures are, at maximum, 3% lower than the experimental data. For the part of the duct which includes the pin-fin array, it appears that the pressures predicted by the numerical simulations are more or less in perfect agreement with those of experiment. In appraising these results, it should be noted that the numerical simulation model without a baffle plate *does not include an extension of the solution domain upstream of the duct inlet*. In addition, *the air velocity entering the duct was assumed to be uniform*, which is not a perfectly realistic assumption. These departures from reality may be the factors responsible for the slight disagreement between the predicted and experimental results of Figure 3.5.

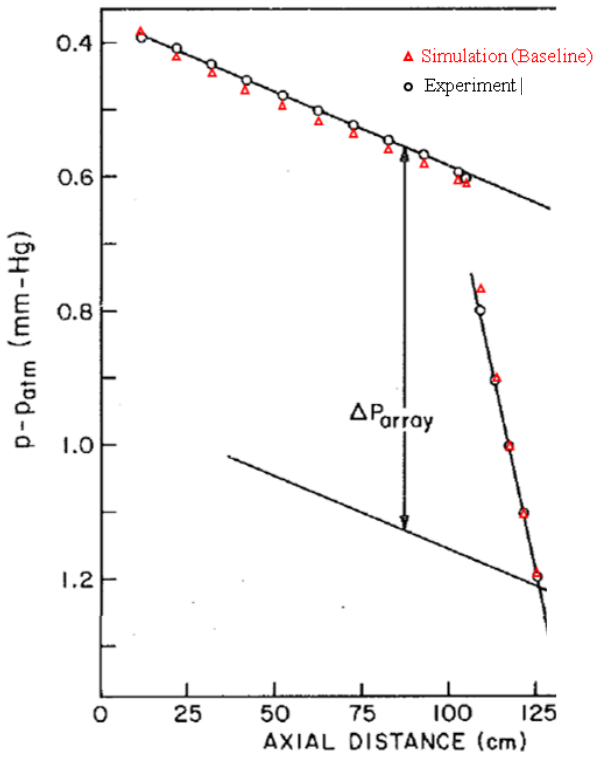


Figure 3.5 Comparison of numerically predicted pressure distributions with experimental data for the case in which there is no baffle plate at the duct inlet (baseline case).

The next comparison to be made is between the numerical simulation results corresponding to the with-baffle case and the experimental data. With the baffle in place, two upstream extensions of the solution domain were employed. The upstream extension designated as A is shown in Figure 3.6. As can be seen from the figure, extension A is a hemisphere. The boundary condition at the exposed surfaces of the upstream extension is atmosphere pressure, which corresponds to a gauge pressure of zero. Those surfaces are designated as openings which permit air to pass through without any impedance. The use of an upstream extension of the solution domain eliminates the need to prescribe anything at the duct inlet cross section.

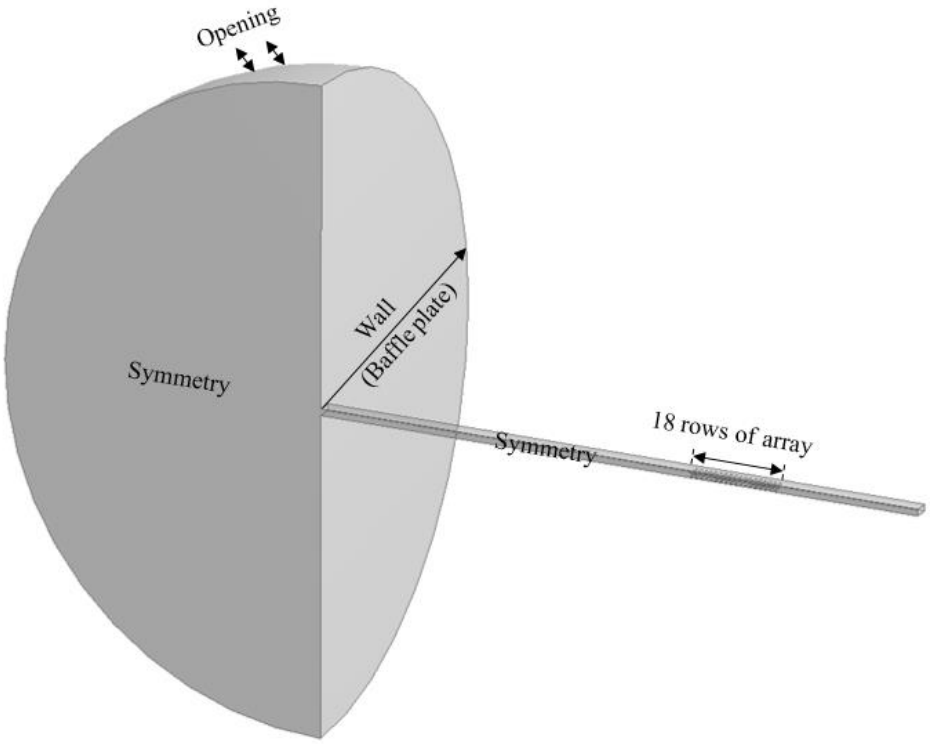


Figure 3.6 Schematic diagram of upstream extension A of the solution domain.

The numerical predictions for the pressure distribution corresponding to this extended solution domain are shown in Figure 3.7 along with the corresponding experimental data. The numerical results are shown as blue symbols. Also appearing in the figure are the red symbols that were previously displayed in Figure 3.5 for the no-baffle case. As can be seen from the figure, the numerical data corresponding to the upstream extended domain A are in excellent agreement with the experimental results in the region upstream of the pin-fin array. This level of agreement can be attributed to the realistic treatment of the inlet condition. Clearly, the level of agreement displayed in Figure 3.7 is much better than that seen in Figure 3.5. The outcome can be attributed to the correct treatment of the inlet condition.

The comparison displayed in Figure 3.7 will now be continued to the portion of the duct that hosts the pin-fin array. Here, it appears that the latest simulation predictions are not

quite as good as those based on the absence of the baffle. However, the agreement is still highly satisfactory.

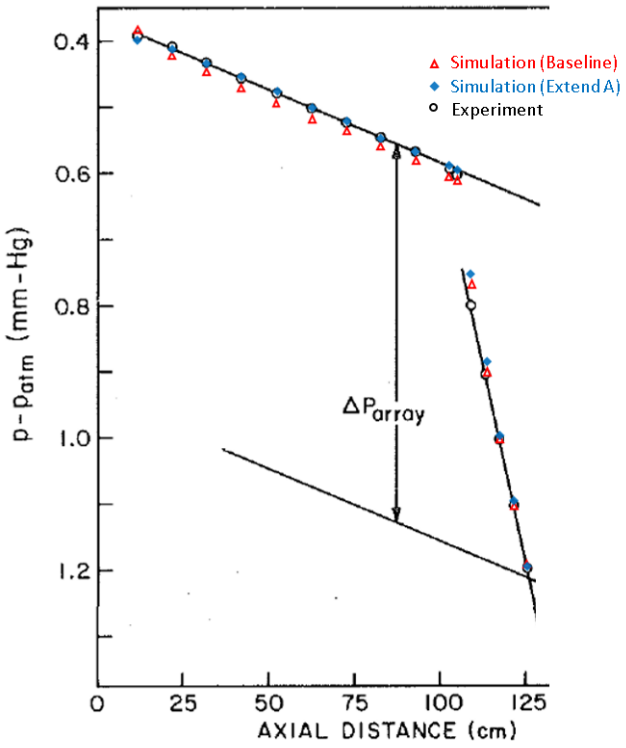


Figure 3.7 Comparison of numerically predicted pressure distributions with experimental data for the case in which the solution domain includes the upstream extension A.

Still another numerical simulation was performed but with a different shape of upstream extension of the solution domain. That extension may be seen in Figure 3.8. It is a cylindrical extension rather than a hemispherical extension and will be designated as extension B.

The numerical results based on the upstream extension B are shown in Figure 3.9 where they are compared with experimental data and with the predictions for the no-baffle case. Inspection of the figure shows a comparison that is more or less the same as that of Figure 3.7, thereby demonstrating that the different shapes of the upstream extensions A and B had a negligible effect on the results. There is outstanding agreement between numerical predictions and the experimental data in the velocity development region and

satisfactory agreement in the part of the duct that hosts the pin-fin array.

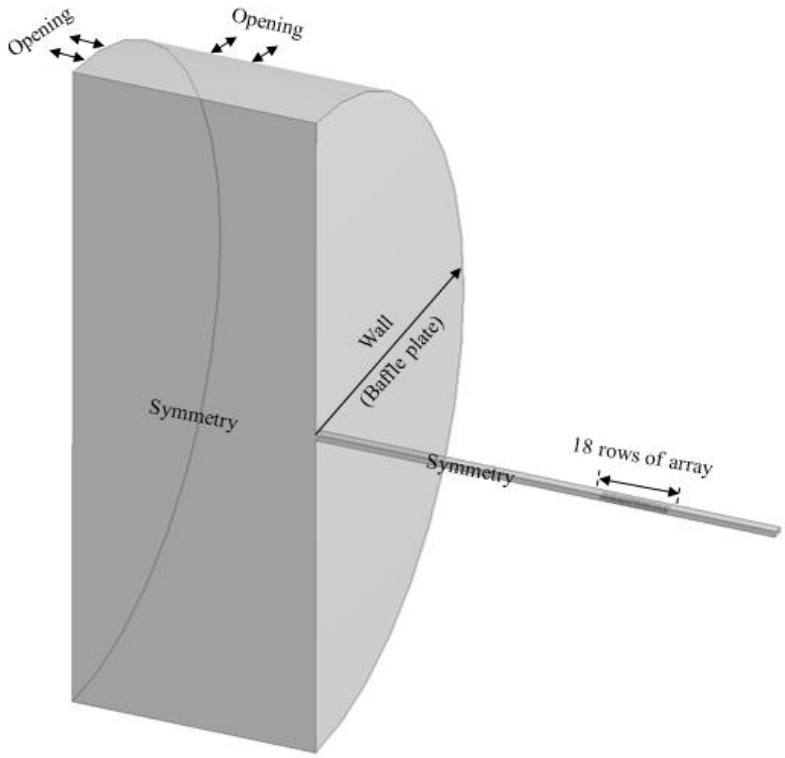


Figure 3.8 Schematic diagram of upstream extension B of the solution domain.

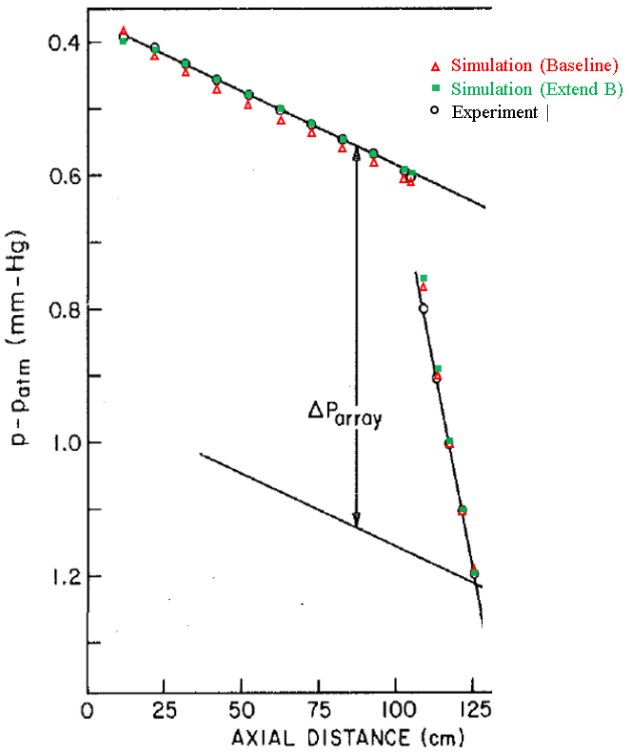


Figure 3.9 Comparison of numerically predicted pressure distributions with experimental data for the case in which the solution domain includes the upstream extension B.

Another mode of comparison between the experimental predictions and the data can be made by means of the *K-factor*. It is well known that the pressure drop through fittings and other obstructions can be expressed in terms of *K-factors*. When applied to the pressure drop caused by the presence of the array, the *K factor* can be defined as

$$K = \Delta\, p_{array} / (\tfrac{1}{2} \rho U_{max}{}^2)\; N \qquad (3.1)$$

In this equation, the array pressure drop is expressed as $\Delta\, p_{array}$, the density of the fluid is $\rho$, the maximum velocity between the fins is $U_{max}$, and $N$ is the number of the rows of fins.

The experimental information, taken from [14], yields $K$ = 0.0817 for a fin height $h/D$ = 2 and a duct Reynolds number of 15,000. The numerical simulations provided three values

of *K*, respectively for the no-baffle case and for the upstream extensions A and B. The corresponding results are 0.0800, 0.0812, and 0.0814. The largest deviation between the experimental and computed *K* value is about 2%, and the smallest deviation is 0.3%. This comparison provides still another support for the simulation model and its implementation.

### 3.3.3 Supporting velocity information

To supplement the previously presented pressure distribution results, some supporting velocity information will now be reported. The first set of results are qualitative cross-sectional velocity distributions information conveyed by color diagrams, as conveyed by Figure 3.10 (a), (b), and (c). These figures respectively correspond to the no-baffle case, the upstream extended solution domain A, and the upstream extended solution domain B. The color red corresponds to the highest velocity and the color green corresponds to a lower velocity.

Careful inspection of the (a), (b), and (c) parts of figure indicates that there are differences between the velocity distributions for the no-baffle case and the baffled cases in the upstream end of the duct. Clearly, the presence of the baffle creates velocity distributions distinguished by a thicker boundary layer. On the other hand, the frictional interaction between the flowing fluid and the wall works to wash out these differences so that it appears that there is only a slight residual effect at a cross section just upstream of the pin-fin array.

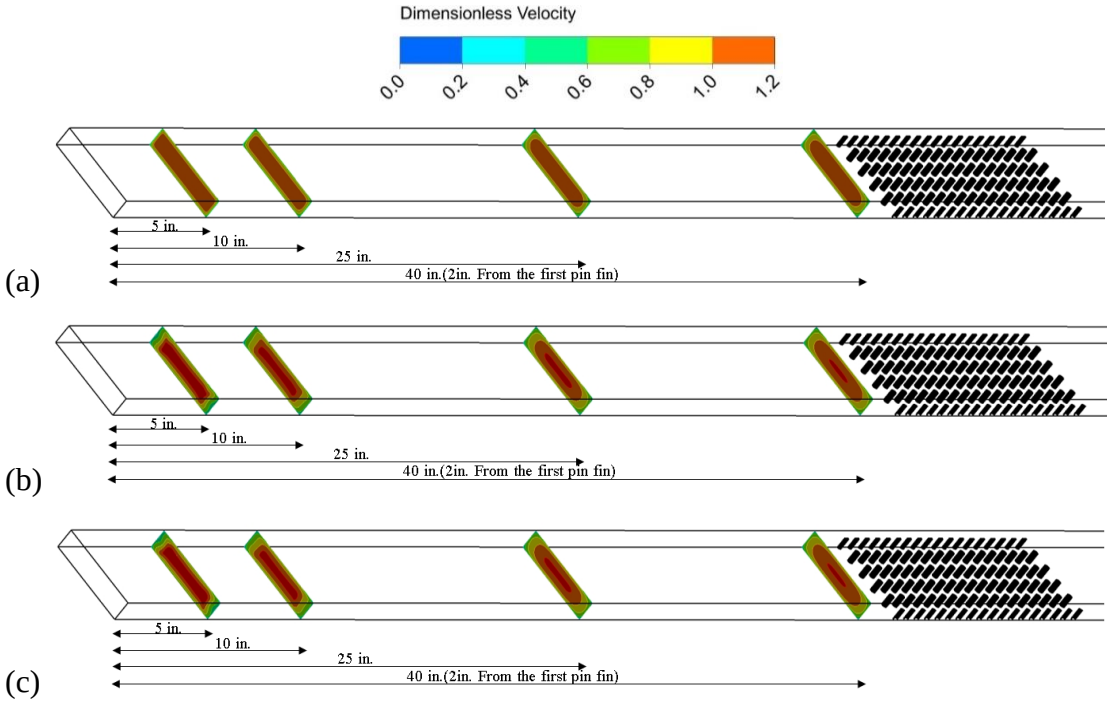


Figure 3.10 Color images of cross-sectional velocity distributions at selected axial locations: (a) no-baffle case, (b) upstream domain extension A, and (c) upstream domain extension B.

To further illuminate the foregoing discussion, Figure 3.11 has been prepared. This figure shows velocity profiles in the duct just upstream of the array. There are three curves in the figure, respectively for the no-baffle case and for the upstream extended domains A and B. It can be seen from the figure that the no-baffle case has a velocity distribution which has not yet merged with those for the baffled cases. For the latter, there is no distinction between the profiles for the upstream domain extensions A and B.

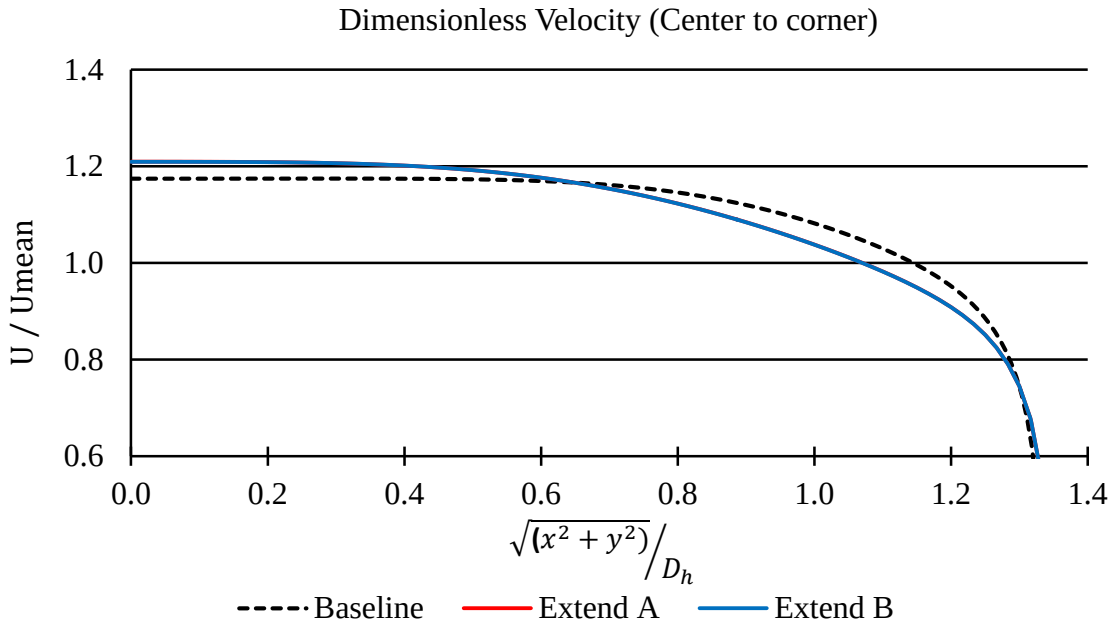


Figure 3.11 Velocity distributions at a location just upstream of the pin-fin array.

## 3.4 Concluding Remarks

This chapter was motivated by the need to obtain validation of the numerical simulation methodology that underlies this thesis. Under normal conditions, it would have been proper to perform laboratory experiments to obtain the needed validation. However, owing to the fact that the Mechanical Engineering building is under repair and laboratory space was not available, data taken in the laboratory at an earlier time was used for the validation purpose. The available data correspond to a duct flow in a hydrodynamic development region and in an array of pin fins.

Specifically, numerical simulations were performed for the exact situation of the experiments that were used for validation. The predictions were carefully compared with the experimental data. It was found that the most extreme deviation of the predictions of pressure was 3% when compared with the experiment, but that deviation can be attributed to the use of an incorrect inlet velocity condition for one of the simulations. The majority

of the comparisons were virtually exact replicates. The overall pin-fin-array pressure drop was compared between the data and predictions with a maximum deviation of 2%.
It is believed that the excellent agreement of the predictions with the experimental data can be regarded as a strong validation of the numerical methodology.

# CHAPTER 4

# INVESTIGATION OF COUPLED SYSTEMS CONSISTING OF FLUID MOVERS AND HEAT EXCHANGE DEVICES

## 4.1 Introduction

A major insufficiency of heat-exchange-device analysis is that it is based on the unrealistic assumption that the fluid flow and pressure required for the operation of the exchanger is automatically available without any consideration of the true capabilities of the related fluid mover. This state-of-affairs seems to include the overwhelming majority of publications that appear in archival journals. The major reason for the broad adoption of this approach is the great difficulty in dealing simultaneously with the heat exchanger and the fluid mover. The outcome of this practice is that errors are committed while the extent of the errors is left unknown.

Here, this practice will be avoided by undertaking an encompassing treatment of the heat exchanger and the fluid mover as a single coupled system. This single-system analysis will be given added significance by accompanying it with a solution of the same problem by the simplified, uncoupled approach. In this way, identification of errors is made possible and the loss of information due to the simplified approach will be determined.

The situation chosen as a case study for considered here has been studied in the published literature solely from the perspective of the heat exchanger, with no focused concern given to the nature of the fluid flow delivered to the inlet of the exchanger. A schematic diagram of the chosen system is conveyed in Figure 4.1. As seen there, an axial fan is positioned flush with the inlet cross section of an array of circular pin fins contained in a duct. The duct is bounded by top, bottom, and side walls. The exit cross section is open to the ambient and is situated downstream of the pin-fin array.

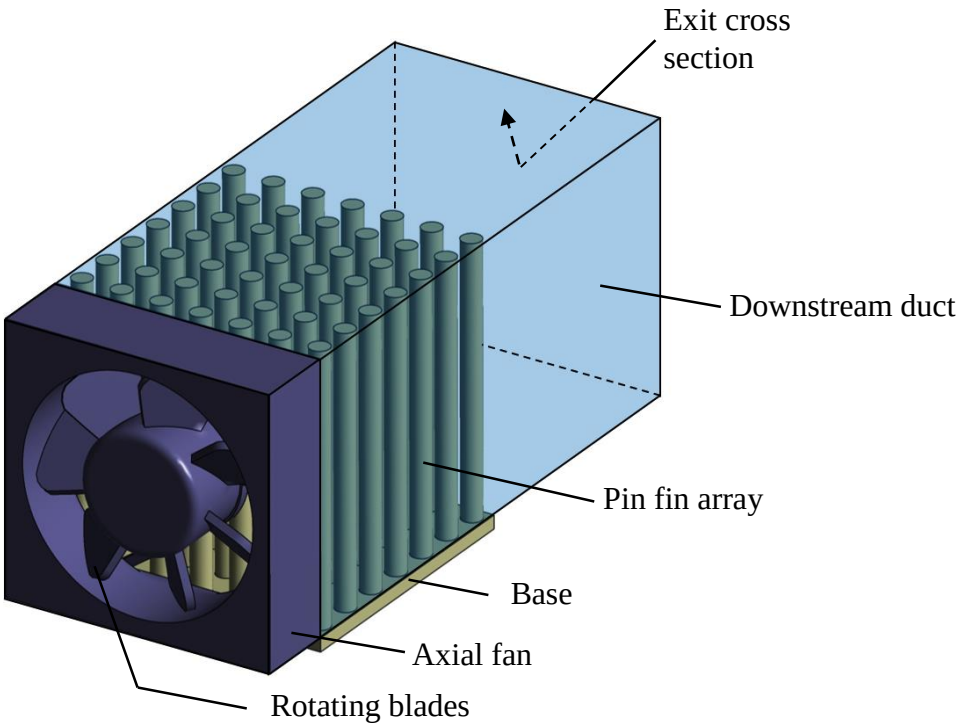


Figure 4.1 Schematic diagram of a pin-fin array and its fluid-mover partner.

The physical situation displayed in Figure 4.1 is a commonly encountered means for temperature management of electronic equipment. The figure displays an array of pin fins that is integral to a baseplate to which an assemblage of heat-generating electronic components is affixed to its downfacing surface. The dissipation of heat from the pin fins and base surface is accomplished by means of the airflow provided by the axial fan (e.g., a muffin fan). The airflow delivered by the muffin fan is both extremely complex and unruly, with a strong swirl component driven by the rotation of the blades. In the simulations, the fluid mover will be operated as it would be in practice, with rotating blades and with struts and supports in place.

In the present numerical investigation, airflow is delivered to the array inlet by the rotating fan, and the fluid flow within the pin-fin array is coupled to that within the

rotating fan. Further coupling occurs between the fan—heat exchanger system and the adjacent environments from which the air is drawn and into which it is subsequently discharged. The convective heat transfer is driven by the fan and interacts by the conjugate heat conduction in the pin fins. Then, two highly simplified no-fan-based cases will be investigated to enable comparisons with the predictions based on the rotating-fan model. For one of the comparisons cases, the delivered airflow is assumed to be the currently standard uniform inlet velocity profile. The magnitude of the inflow was determined from the P-Q curve supplied by the manufacturer. As a variant of the latter, a uniform pressure is applied at the inlet of the array, resulting in a pressure-driven flow.

The first treatment of a fluid mover and a heat exchanger as a single system and where the fan rotation was accounted appears to be due to Zhou and Yang in a 2008 paper [22]. These authors were primarily concerned with the performance of various types of fins, none of which were pin fins, and no comparisons were made with results predicted by the current standard practice of not accounting for fan rotation and using very simple assumptions about the nature of the delivered airflow. Somewhat on the down side, they determined the pressure rise—flow rate (P-Q) characteristics of their fan without taking account of the fact that interactions of a fan with its downstream load can flaw the standard manufacturer-supplied fan curve as has been demonstrated elsewhere, e.g., [23-25].

The literature search will now be extended to papers specifically concerned with pin-fin arrays in crossflow. As already noted in the foregoing, it appears that there is no published work, neither analytical nor experimental, which has dealt with a system which encompasses a fluid mover and a pin-fin array in crossflow. In all analytical/numerical papers, the total focus was on the heat exchanger, and the nature of the delivered air was by assumption.

In one segment of the literature, either the delivered air was assumed to have a uniform velocity profile [26, 27] or a fully developed velocity profile [28]. In both these

situations, it was common to allow a length of non-fin-populated base plate between the fluid inlet cross section and the start of the pin-fin array. This arrangement gives rise to partial development of the velocity distribution, creating uncertainty in the true nature of the velocity profile at first contact of the flowing fluid with the array. A second common feature of the published literature is the assumption that the longitudinal deployment of the pin fins is periodic [26, 29, and 30]. This geometric arrangement enabled investigators to confine their work to determining the so-called periodic fully developed regime. For the determination of that regime, the nature of the fluid flow at the inlet of the pin-fin array is irrelevant, and no consideration was given to that issue.

For further simplification, the transverse deployment of the pin-fin array was regarded either as periodic or, alternatively, as symmetric with concomitant neglect of the duct side walls [26, 28-30]. Both these models enabled consideration to be confined to a single column of fins.

## 4.2 Modeling and Numerical Simulations

In the considered physical situation depicted in Figure 4.1, the fluid flow is turbulent, three-dimensional, and unsteady. In present-day implementations of numerical simulation for turbulent flow, a very common approach is the use of the Reynolds-Averaged, Navier-Stokes (RANS) equations in conjunction with a suitable turbulence model. There are many such models in the published literature. Here, the Shear Stress Transport (SST) model [31] was chosen because of its highly favorable characteristics with respect to the type of problem now under consideration. In particular, the rotating fan blades create a swirling motion in the air delivered to the array. As will be documented shortly, the SST model has excelled in swirl-dominated fluid flow situations.

In [32], six turbulence models were employed to predict the swirling motion in a pipe due to an upstream flow in which a controlled swirl was created. The considered models

included the standard $k$-$\varepsilon$ model, a curvature modified $k$-$\varepsilon$ model, Chen's $k$-$\varepsilon$ model, a cubic non-linear $k$-$\varepsilon$ model, the standard $k$-$\omega$ model, and the SST model. Note that $\omega$ is the frequency of the turbulent fluctuations, $\varepsilon$ is the turbulence dissipation, and $k$ is the turbulence kinetic energy per unit mass. It was concluded in [32] that the SST model was the best numerical model when compared with experimental results.

A completely independent study of the relative efficacies of various turbulence models was performed in [33]. In that regard, [33] considered steady flow in a narrow channel, without side walls, of a single column of pin fins, but having a prescribed inlet velocity and a velocity development length. Again, six turbulence models were investigated, three of which were based on the $k$-$\omega$ platform including BSL, SST, and the explicit algebraic Reynolds Stress Model (EARSM). The three other models were based on the $k$-ε platform: REAL, RNG, and V2 F. The author of [33] concluded that the SST turbulence model gave the best overall prediction of the pin-fin channel flow relative to experimental data.

Several additional studies have demonstrated the efficacious performance of the SST turbulence model [34-36]. Among these, [34] dealt with swirl situations whereas [35, 36] were focused on pipe and duct flows.

The SST model brings together the venerable and commonly used $\kappa$-$\varepsilon$ model and the relatively newer $\kappa$-$\omega$ model. The $\kappa$-$\varepsilon$ model is known to yield accurate results away from bounding surfaces; in contrast, the $\kappa$-$\omega$ model has been demonstrated to be highly effective in the near neighborhood of the bounding surfaces.

In addition to the aforementioned displays of the competence of the SST model, it has been demonstrated [1] that the model automatically reduces to laminar flow wherever the actual flow is laminar. Therefore, even if there were isolated pockets of laminar flow in an otherwise primarily turbulent flow, the SST model would be capable of dealing with such situations.

The numerical simulations were carried out by means of ANSYS CFX 15.0 software. The discretization of the governing partial differential equations was performed by means of the finite-volume approach. A demonstration of *mesh independence* is a mandatory part of any numerical simulation solution. The evaluation of mesh independence is logically based on tracking the variation of a key physical quantity as a function of the number of nodes. The physical quantity chosen here is the overall rate of heat transfer. From the mesh independence study, it was found that increasing the node number from 12 to 14 million gave rise to changes of the heat transfer rate no greater than 0.10%. The iterative solutions were regarded as converged when the residuals were $10^{-5}$ or smaller. Since the problem was treated as being unsteady, it was essential that a sufficiently small time step be used. It was found that a time step of 0.01 seconds was satisfactory. The rotational speed of the fan was 6400 rpm.

Another issue that is critical to the fidelity of the simulation model is the choice of the volume in which the solutions are carried out. The guiding principle for choosing the solution volume is that the fluid has full freedom to execute its natural motions. That space is commonly called the *solution domain*. A schematic diagram of the solution domain selected for the present rotating-fan problem is displayed in Figure 4.2. It is seen from the figure that a spacious upstream extension of the solution domain was allowed to enable the rotating fan to draw air freely from its upstream and lateral surroundings. The fan housing, the square duct to which it is mated, and the duct exit comprise the other bounding surfaces of the solution domain.

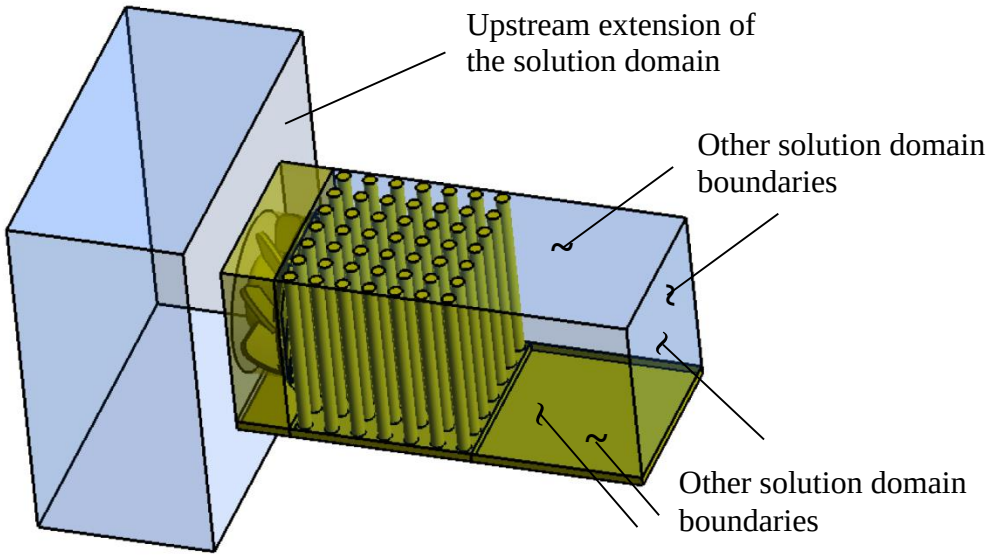


Figure 4.2 Schematic diagram of the solution domain.

A table listing the geometrical specifications of the pin fin array is presented in Table 1. Note in the table that the length of the duct downstream of the fin array is equal to the streamwise length of the array. The fins are made of aluminum (thermal conductivity = 237 $W/m\text{-}^oC$, density = 2702 $kg/m^3$, and specific heat = 903 $J/kg\text{-}^oC$).

Table 4.1 Dimensional information.

| **Component** | **Dimension or ratio** |
|---|---|
| Fin diameter | 3.75 mm |
| Center-to-center distance | 7.5 mm |
| ST/D, SL/D | 2 |
| Fin height | 50 mm |
| Base width and length | 50 mm |

## 4.3 Governing Equations and Boundary Conditions

The relevant physical principles that govern the flow and heat transfer are: momentum conservation (Reynolds-Averaged, Navier-Stokes (RANS) equations), mass

conservation, and the First Law of Thermodynamics. These equations are written for unsteady, three-dimensional, incompressible, and constant property flow of air with the properties being those at 25 $^{o}C$. In compact, Cartesian-tensor form, the RANS equations are

$$\rho \frac{\partial u_j}{\partial t} + \rho \left( u_i \frac{\partial u_j}{\partial x_i} \right) = -\frac{\partial p}{\partial x_j} + \frac{\partial}{\partial x_i} \left( (\mu + \mu_{turb}) \frac{\partial u_j}{\partial x_i} \right) + S_{rotation} \quad i = 1,2,3 \; and \; j = 1,2,3 \tag{4.1}$$

where the rotation-related source term is

$$S_{rotation} = -\rho \boldsymbol{\omega} \times (\boldsymbol{\omega} \times \boldsymbol{r}) - 2\rho \boldsymbol{\omega} \times \boldsymbol{u_{\theta,i}} \tag{4.2}$$

The rotating domain (a relatively small, meshed fluid volume surrounding the rotating components of the non-deforming fan blades and hub) uses rotating frames of reference at a specified angular velocity $\boldsymbol{\omega}$, and includes both Coriolis forces and centrifugal momentum terms, in addition to a rotating-frame energy equation. The first term on the right-hand side of Equation (4.2) is the centrifugal term, and the second represents the Coriolis forces. In addition, $\boldsymbol{r}$ is the position vector, and $\boldsymbol{u_{\theta,i}}$ is the rotating frame velocity.

Next, the mass conservation equation is

$$\frac{\partial u_i}{\partial x_i} = 0 \tag{4.3}$$

The quantity $\mu_{turb}$ in Equation (4.1) is designated as the turbulent viscosity. The determination of $\mu_{turb}$ is achieved by means of the Shear Stress Transport (SST) turbulence model.

The governing equations for the SST turbulence model are

$$\frac{\partial(\rho\kappa)}{\partial t}+\frac{\partial(\rho u_i\kappa)}{\partial x_i}=P_\kappa-\beta_1\rho\kappa\omega+\frac{\partial}{\partial x_i}\left[\left(\mu+\frac{\mu_{turb}}{\sigma_\kappa}\right)\frac{\partial\kappa}{\partial x_i}\right] \tag{4.4}$$

$$\frac{\partial(\rho\omega)}{\partial t}+\frac{\partial(\rho u_i\omega)}{\partial x_i}=A\rho S^2-\beta_2\rho\omega^2+\frac{\partial}{\partial x_i}\left[\left(\mu+\frac{\mu_{turb}}{\sigma_\omega}\right)\frac{\partial\omega}{\partial x_i}\right]+2\rho(1-F_1)\frac{1}{\sigma_{\omega 2}\omega}\frac{\partial\kappa}{\partial x_i}\frac{\partial\omega}{\partial x_i} \tag{4.5}$$

Once $\kappa$ and $\omega$ have been found from the solution of the foregoing equations, the eddy viscosity $\mu_{turb}$ is obtained from

$$\mu_{turb}=\frac{\alpha\rho\kappa}{\max(\alpha\omega,SF_2)} \tag{4.6}$$

The First Law of Thermodynamics for a constant-property, turbulent flowing fluid, supplemented by the Fourier law of heat conduction, is

$$\rho c_p\frac{\partial T}{\partial t}+\rho c_p\frac{\partial(u_iT)}{\partial x_i}=\frac{\partial}{\partial x_i}\left[(k+k_{turb})\frac{\partial T}{\partial x_i}\right] \tag{4.7}$$

in which the quantity $k_{turb}$ is used to quantify the contribution of turbulence to the transfer of heat. This quantity, in common with $\mu_{turb}$, is not a true property of the fluid. To obtain numerical values for $k_{turb}$, the turbulent Prandtl number $Pr_{turb}$ is used, where

$$Pr_{turb}=c_p\mu_{turb}/k_{turb}=0.85 \tag{4.8}$$

The numerical value 0.85 is based on comparisons of predicted heat transfer coefficients with those of experiment [38, 39].

The heat transfer problem is conjugate in that convection in the flowing fluid interacts with conduction in the pin fins. As a consequence, the heat conduction equation for the

pin fins must be solved simultaneously with the fluid energy equation, Equation (4.7). For unsteady fin conduction,

$$(\rho c)_{fin} \frac{\partial T_{fin}}{\partial t} = k_{fin} \frac{\partial^2 T_{fin}}{\partial {x_i}^2} \tag{4.9}$$

To complete the statement of the problem, boundary conditions must be provided. All of the surfaces that comprise the upstream extension of the solution domain pictured in Figure 2 were specified as openings, allowing the air to choose its own direction. The pressures on these surfaces was specified as being the ambient value, which corresponds to zero gauge pressure. The temperature of the air crossing these surfaces was uniform and equal to $T_{\infty}$.

All of the solid walls within the solution domain (Figures 4.1 and 4.2) are no-slip and impermeable surfaces with respect to velocity. With regard to heat transfer, the fan blades and frame and the duct walls are adiabatic. The exposed surface of the base plate and the base of the pin fins are isothermal at a temperature $T_{base}$.

At the exit of the duct, a closure is imposed wherein the streamwise second derivatives of all three velocity components and the temperature are zero. The gauge pressure at the exit plane is zero.

## 4.4 Definition of Comparison Case

To demonstrate the significance of the single-system approach to heat exchangers and fluid movers, it is relevant to compare the results obtained from that model to those which would be forthcoming from the presently standard model in which the fluid delivered to the exchanger inlet is arbitrarily specified as a boundary condition for the solution of the flow and heat transfer in the heat exchanger. That specification is primarily based on the P-Q (pressure rise vs. flow rate) curve provided by the

manufacturer of the fan. In order to effectuate such a comparison, it is necessary to make use of the presently standard model. To this end, the available P-Q curve for the fan is that without regard to the downstream load serviced by the fan. Figure 3 is the P-Q curve which shows the pressure rise in mm $H_2O$ on the vertical axis and the volumetric flow rate in CFM or $m^3$/min on the abscissa for the fan in question.

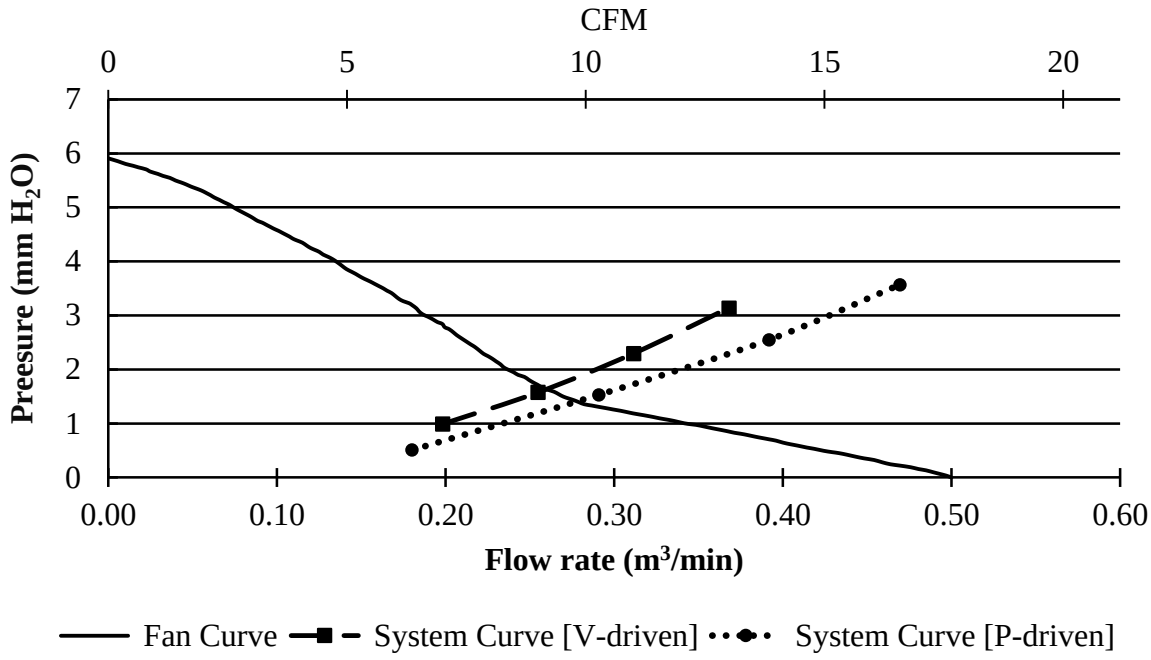


Figure 4.3 P-Q curve for SOFASCO fan D5015 and system curves for the pin-fin heat exchanger situated in the duct pictured in Figure 4.1.

The displayed P-Q curve is of the generally encountered shape for small axial fans. In addition to the P-Q curve of Figure 4.3, there are two additional curves which represent the pressure drop versus flow rate for the pin-fin array situated in the duct pictured in Figure 4.1. It will be convenient to denote the pin-fin array situated within the duct as the heat-exchanger system. Such curves are typically designated as heat-exchanger system curves and do not relate in any way to the fan in question.

To determine a heat-exchanger system curve, the geometry of interest is identified and a uniform flow is envisioned as entering that geometry. The magnitude of the entering

velocity is specified, and the pressure drop experienced by that flow as it passes through the heat-exchanger system is determined. In the present instance, that determination is made by means of highly accurate numerical simulations. In this way, a secession of points can be plotted on the P-Q diagram, and a curve fit can be performed to provide a continuous curve. One such curve is labeled (V given) in Figure 4.3.

A second heat-exchanger system curve will now be constructed. For that situation, it will be assumed that a uniform pressure is imposed at the inlet of the heat-exchanger system. Based on that given value, a highly accurate numerical simulation is performed to give the volumetric flowrate passing through the system. This procedure is continued until a succession of points are plotted on the P-Q diagram, and the points are curve fitted to give a continuous line. That curve is labeled (P given) in Figure 4.3.

The intersection of the respective heat-exchanger system curves with the fan curve provides unique operating conditions. Accurate numerical simulations were performed for both the fluid flow and the heat transfer corresponding to the respective operating points indicated in Figure 4.3. Those results will be compared shortly with those based on the single-system model for the fluid mover and the heat exchanger.

## 4.5 Heat Transfer Results and Discussion

The presentation of thermal-related results will be initiated by an exposition of the overall rate of heat transfer between the pin-fin array and the flowing air. This information will be followed by a display of the local pin-fin heat transfer results, after which the unsteady nature of the rate of heat transfer will be exhibited. The final section of the heat transfer presentation will show temperatures within the pin-fin array.

### 4.5.1 Overall rate of heat transfer

The numerical simulation solutions have provided the rates of heat transfer from the pin-fin array to the flowing air for the three cases of interest here. One of these cases is based on the model in which the fluid mover and the heat exchanger are modeled as a single interacting system. The two other cases correspond to the presently standard approach whereby the fluid flow delivered to the heat exchanger inlet is specified independently and arbitrarily. Here, the specification is made by use of the P-Q fan curve provided by the manufacturer. That curve was employed somewhat innovatively here by considering both velocity-driven flows and pressure-driven flows. The consideration of the latter is uncommon in the heat exchanger literature.

The overall heat transfer results are listed in Table 4.2. Since the fluid flow and heat transfer are intrinsically unsteady, the information conveyed in the table is time-averaged. Separate consideration is given in the listing to the heat transfer from the fin array to the airflow and to the heat flowing from the base surface to the airflow. The tabulated information is respectively conveyed under three column headings. The first column displays the heat transfer corresponding to the present single-system treatment of the fluid mover and the heat exchanger, whereas the last two columns are based on the use of the P-Q curve. If the first focus is on the pin-fin-array heat transfer, it is seen that the simplified standard approach gives rise to an overestimation of the heat transfer rate. This outcome is reasonable since the complex fan-provided fluid flow creates a higher pressure drop than that corresponding to a uniformly entering flow. It can be reasoned that that pressure drop will diminish the flowrate and cause a decrease in the overall rate of heat transfer.

Table 4.2 Overall pin-fin-array heat transfer results comparing those of the rotating-fan-delivered air case with those of the velocity- and pressure-driven P-Q flowrates. The temperature difference $(T_{base} - T_{\infty}) = 30\ ^{o}C$.

| | Rate of heat transfer ($W$) | | |
|---|---|---|---|
| | Rotating fan | P-Q curve with V-driven inflow | P-Q curve with P-driven inflow |
| Through fins | 34.5 | 47.4 | 40.9 |
| Through base | 1.37 | 1.24 | 1.26 |

Since it is likely that the presently standard approach would utilize a velocity-driven flow in conjunction with the P-Q curve, it is relevant to compare the heat transfer results in the first two columns. That comparison shows that the simplified-approach heat transfer rate is about 37% greater than that predicted by the present single-system treatment. If a similar comparison is made between the first and third columns, it is seen that the simple-model overestimation is about 19%. This difference in overestimation can be explained by recognizing that in the velocity-driven P-Q case, the entering velocity distribution is uniform, whereas in the pressure-driven P-Q case, the entering velocity distribution is distinctly non-uniform.

With regard to the base-surface heat transfer rate displayed in Table 4.2, it is seen that the magnitude predicted by the present single-system treatment is slightly larger, by approximately 10 %, than that of the PQ models.

### 4.5.2 Per-fin heat transfer rates

The numerical simulations enabled the local per-fin heat transfer rates to be determined. A convenient manner of presenting this local information is in ratio form whereby the per-fin heat transfer rate is divided by the average rate of heat transfer for the array as a whole. Both the numerator and denominator of the ratio represent time-averaged quantities. The normalized per-fin heat transfer information is presented in Figures 4.4,

4.5, and 4.6, respectively for the cases of the fluid-mover—heat-exchanger system, the velocity-driven P-Q model, and the pressure-driven P-Q model. The view conveyed in the figures is a plan view looking downward on the bed of pin fins.

Inspection of Figure 4 indicates a wide variation is the per-fin heat transfer rate. There is a monotonic row-by-row decrease in the per-fin heat transfer rates from the first to the last row. This is the expected trend in a tube bank. The absence of symmetry with respect to column 4 is noteworthy. In particular, the local per-fin values for fins 1, 2, and 3 differ from the values for fins 5, 6, and 7 in a given row. This outcome is the result of the direction of fan rotation.

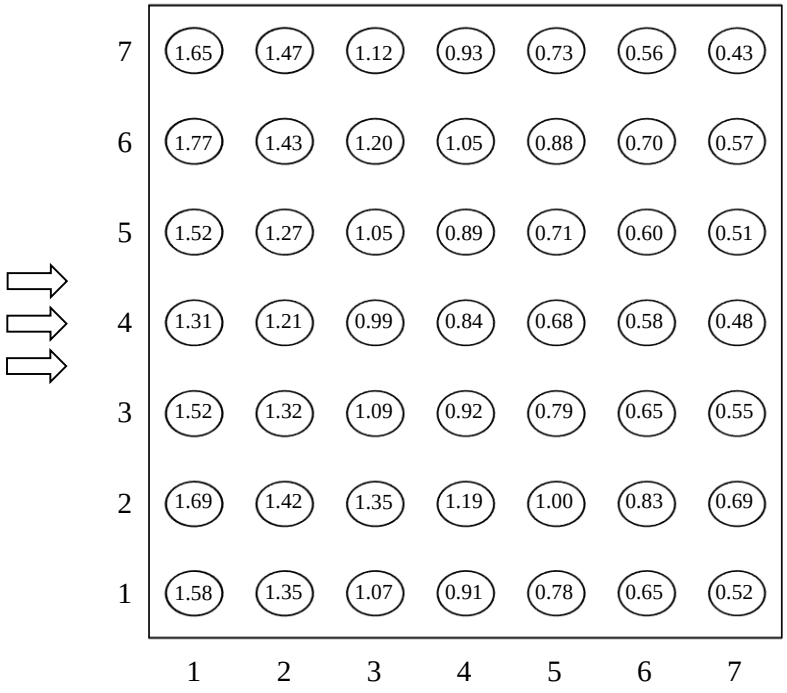


Figure 4.4 Normalized per-fin heat transfer rates in the form $Q_{fin}/Q_{ave}$ for the fluid-mover—heat-exchanger system.

Attention will now be turned to Figure 4.5. Here, the inflow of air entering the array is uniformly distributed, with the outcome being a much more uniform pattern of per-fin heat transfer. The fins in the first row experience virtually identical rates of heat transfer.

With increasing downstream distance, the velocity distribution at any cross section is modified by the presence of the side walls, so that the per-fin heat transfer rates display a cross-sectional distribution with the highest rates occurring away from the side walls and the lowest rates occurring adjacent to the side walls. In the streamwise direction, there is an orderly decrease in the per-fin rate of heat transfer.

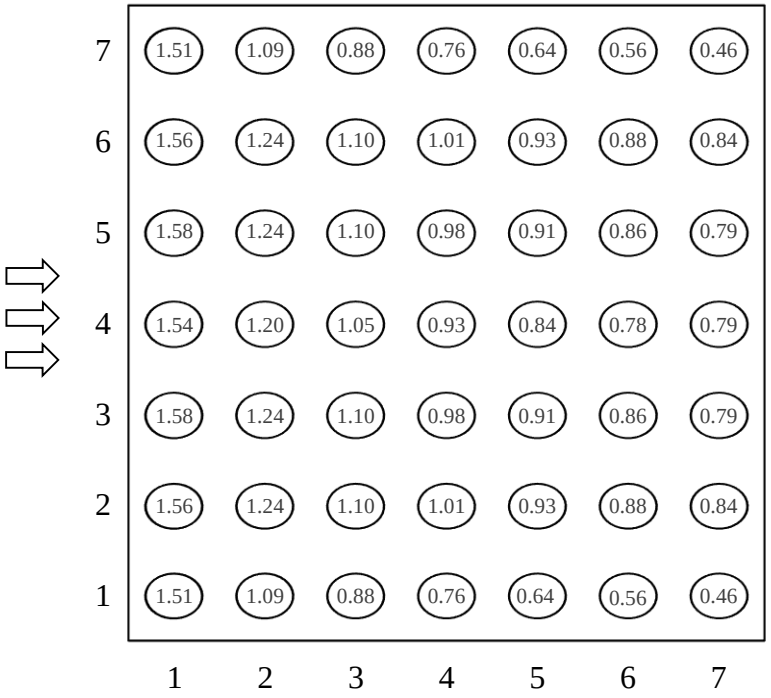


Figure 4.5 Normalized per-fin heat transfer rates in the form $Q_{fin}/Q_{ave}$ for the velocity-driven P-Q model.

Figure 4.6 is the last of the figures showing the local heat transfer results. It pertains to the pressure-driven P-Q model. It is appropriate to compare Figure 4.6 with its counterpart, Figure 4.5, because both are variants of the P-Q model. The comparison shows that the pressure-driven model gives rise to an overall more uniform distribution of the local rates of heat transfer.

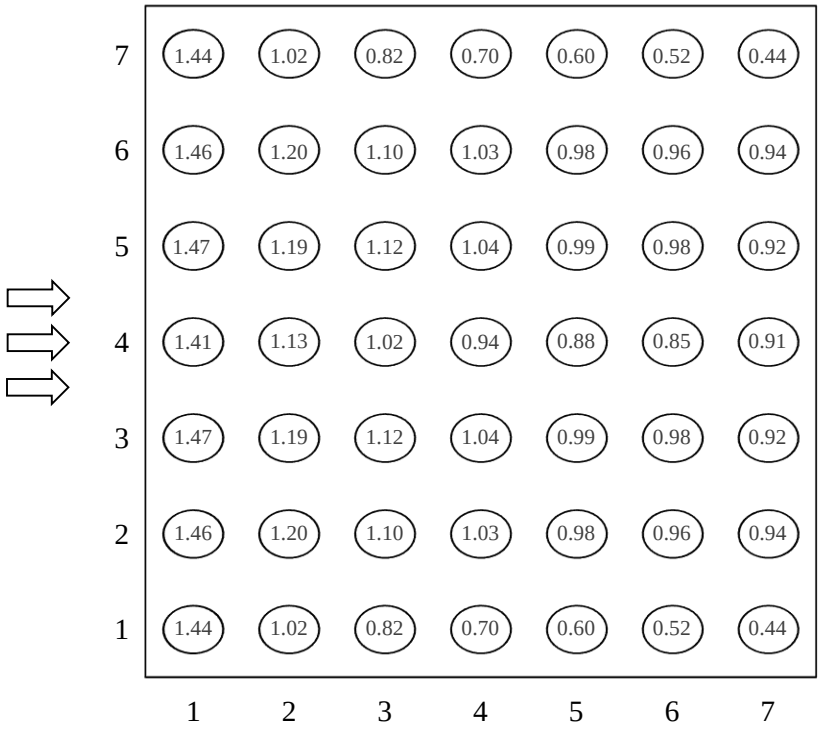


Figure 4.6 Normalized per-fin heat transfer rates in the form $Q_{fin}/Q_{ave}$ for the pressure-driven P-Q model.

### 4.5.3 Timewise variations of heat transfer

Fan rotation delivers a time-varying airflow to the inlet of the heat exchanger with a consequent time variation of the rate of heat transfer at both the fin array and the base surface. Illustrations of these time variations are displayed in Figures 4.7 and 4.8, respectively for the fin array and the base surface. The figures show spatial-integrated rates of heat transfer at fixed times presented as a function of the number of revolutions of the rotating fan. Note that the start-up transient period has been omitted from these figures.

In appraising the timewise variations exhibited in Figures 4.7 and 4.8, it is relevant to note that the displayed results depend not only on the imposed unsteadiness due to the

rotation of the fan, but are also affected by the heat capacity of the materials that comprise the heat exchanger.

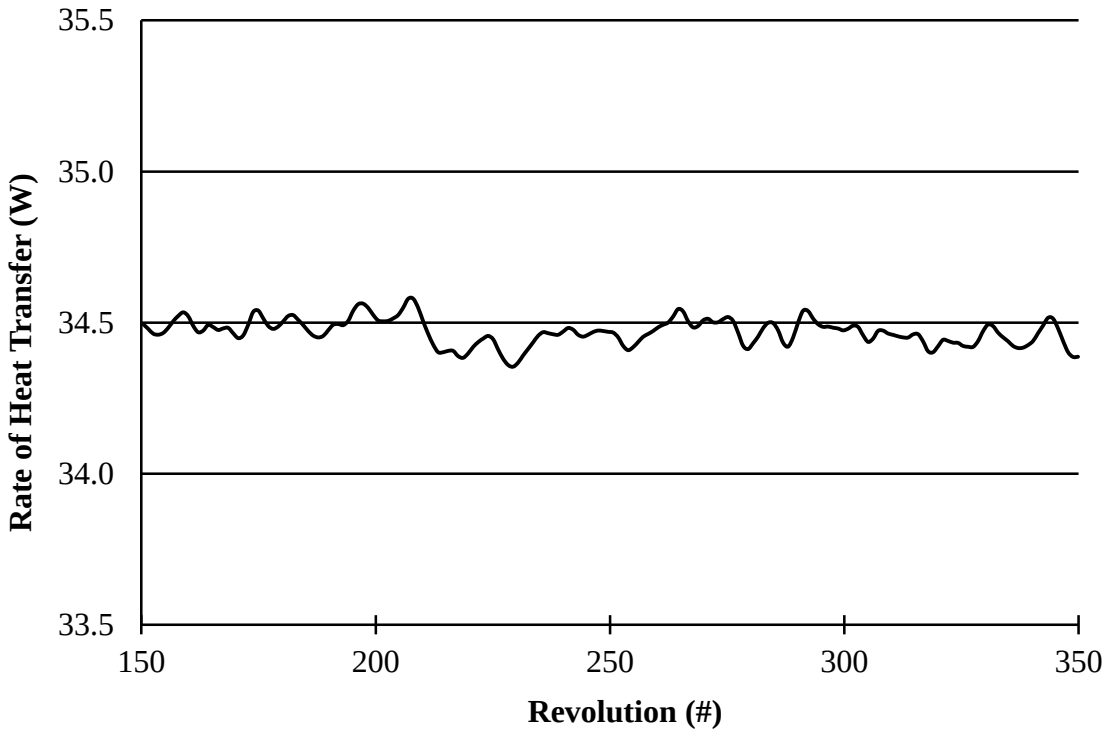


Figure 4.7 Timewise variation of the overall rate of heat transfer from the pin-fin array for the fluid-mover—heat-exchanger system.

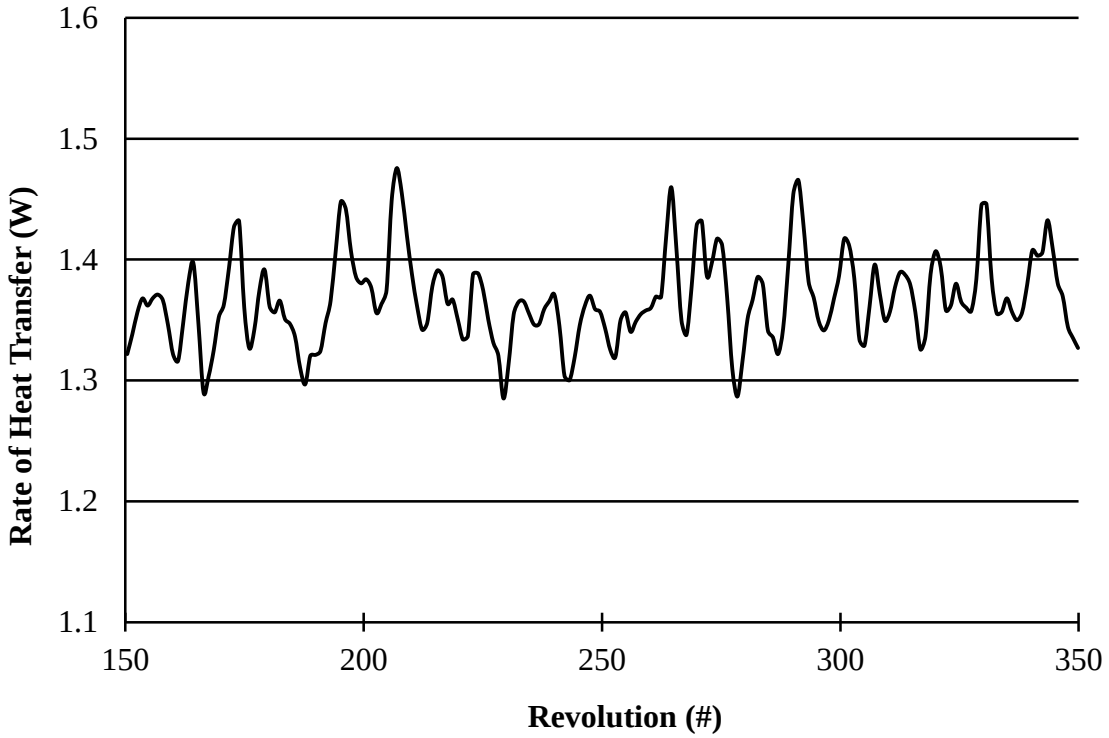


Figure 4.8 Timewise variation of the overall rate of heat transfer from the base surface for the fluid-mover—heat-exchanger system.

### 4.5.4 Temperature distributions

Further insights into the physical processes which occur within the pin-fin array can be extracted from temperature field information conveyed in Figures 4.9, 4.10, and 4.11. Each figure consists of three parts, respectively corresponding to the fluid-mover—heat-exchanger system, the velocity-driven P-Q model, and the pressure-driven P-Q model. The displayed images are instantaneous. Figure 4.9 shows a plane parallel to the base surface and 1 cm above it, and Figures 4.10 and 4.11 are respectively for planes that are 2.5 and 4 cm above the base. The height of the duct is 5 cm. To help interpret these figures, recall that the inlet fluid temperature is 20 $^{o}$C, and the base surface temperature is 50 $^{o}$C. These values are arbitrary and do not affect the nature of the results.

It is seen from Figure 4.9 that the temperature pattern for the rotating fan case is distinctly different from those for the P-Q cases. For the latter, tongues of incoming cool fluid penetrate deeply into the array, threading through the lanes between the fins. In contrast, for the rotating fan case, the cool fluid does not penetrate very deeply into the array except for a single tongue. Rather, there is a tendency for the incoming flow to meander and thereby to attain somewhat elevated temperature. In the open duct downstream of the array, the flow achieves higher temperatures than those associated with the P-Q flows.

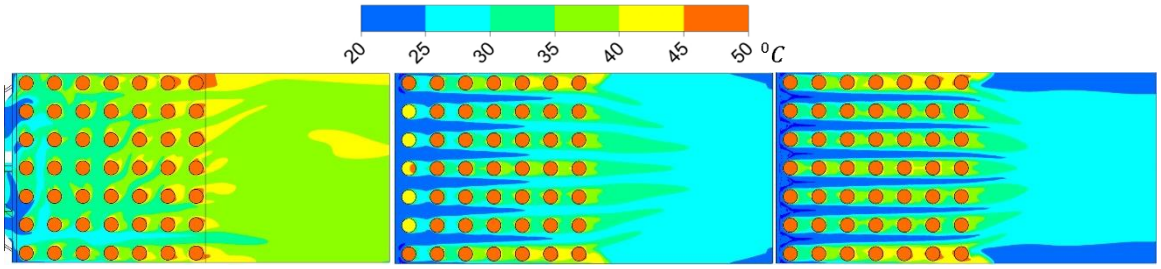


Rotating fan P-Q velocity driven P-Q pressure driven

Figure 4.9 Instantaneous temperature distributions on a plane parallel to the base surface and 1 cm above it.

Figure 4.10 displays temperature patterns that are more or less the same as those of Figure 4.9 for the P-Q cases. For the rotating fan case, there are now two tongues of cool fluid that penetrate the array but, in addition, there is a stream of relatively warmer fluid that occupies an intermediate position between the two cool tongues. The fluid in the duct downstream of the array is cooler than that seen in Figure 4.9. Figure 4.11 maintains the same appearance as in the prior figures for the P-Q cases. However, for the rotating fan case, the cool incoming fluid tends to meander, but it appears that other fluid within the array has experienced moderate heating. In the downstream duct, the elected temperatures seen in Figure 4.9 are once again seen. The temperature patterns reflect the great differences between the regularity of the flow in the P-Q cases and the randomness of the rotating-fan delivered flow.

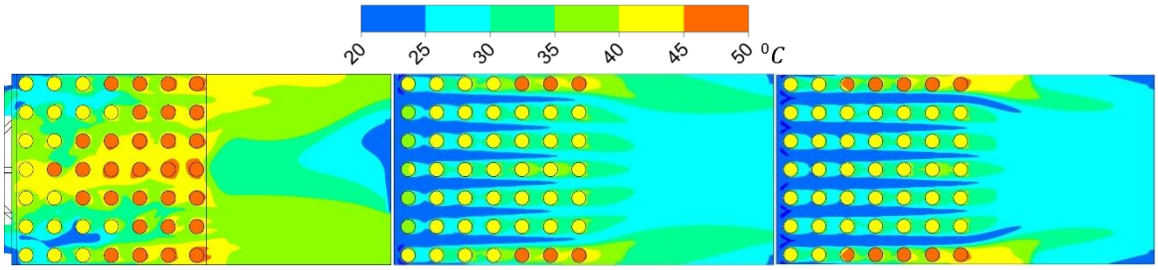


Rotating fan P-Q velocity driven P-Q pressure driven

Figure 4.10 Instantaneous temperature distributions on a plane parallel to the base surface and 2.5 cm above it.

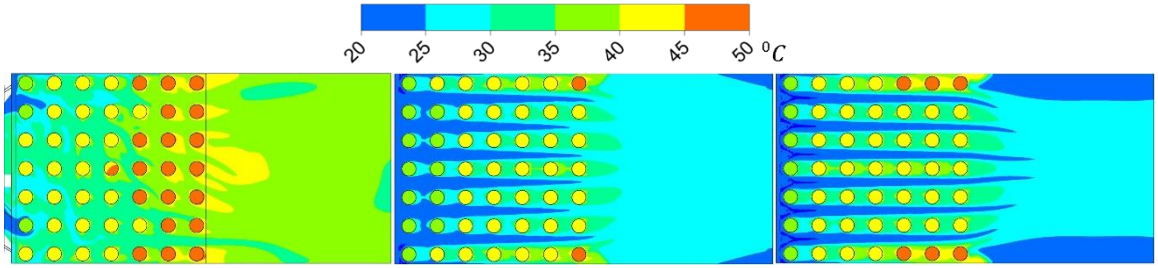


Rotating fan P-Q velocity driven P-Q pressure driven

Figure 4.11 Instantaneous temperature distributions on a plane parallel to the base surface and 4 cm above it.

## 4.6 Fluid-mechanic Results and Discussion

The presentation of fluid-flow results will include the mass flow rates corresponding to the three flow-delivery models, velocity contour diagrams, and velocity vector diagrams.

The fluid flow inferences drawn from Table 4.2 and Figures 4.9-4.11 are corroborated in Table 4.3, which displays the mass flow rates for each of the flow delivery models investigated in this paper. The expectation based on those inferences is that the fan-driven flowrate should be much lower than the flowrates based on the P-Q models. As seen in the table, the fan-driven flowrate is approximately 37% of those based on the P-Q models. With such a disparity, it might be expected that the degradation of heat transfer performance for the rotating-fan case would be even greater than that shown in Table 4.2. There, it is shown that the heat transfer for the fan-driven case is about 73% of that of the

velocity-driven P-Q model. The counteracting process which enhances the heat transfer in the fan-driven case is the mixing of the fluid passing through the array due to the swirl imparted by fan rotation.

Table 4.3 Mass flow rates corresponding to different fluid delivery models.

| Mass flow rate (kg/s) | | |
|---|---|---|
| Blower curve (V-driven) | Blower curve (P-driven) | Rotating fan |
| 0.00543 | 0.00549 | 0.00205 |

### 4.6.1 Velocity contour diagrams

Velocity contour diagram are presented in Figures 4.12-4.14, respectively for planes of observation that are parallel to the base and respectively situated 1, 2.5, and 4 cm above it. The height of the duct is 5 cm. Inspection of Figure 4.12 reveals a flow pattern for the P-Q cases that is drastically different from than for the rotating fan case. Whereas the former flow patterns relentlessly follow the lanes between the adjacent columns of fins, there is no easily identified pattern that can be seem for the fan-driven flow. The reason for the disparity is that the fan-driven flow is unable to penetrate the pin-fin array at this level of the observation plane. Further study of the rotating fan results of Figure 4.12 suggests that there are pockets of backflow (negative velocities) in the lanes between the adjacent columns of fins. Furthermore, it appears that the largest expanse of forward flow occurs downstream of the array. These trends will be more definitively illustrated shortly by means of vector diagrams.

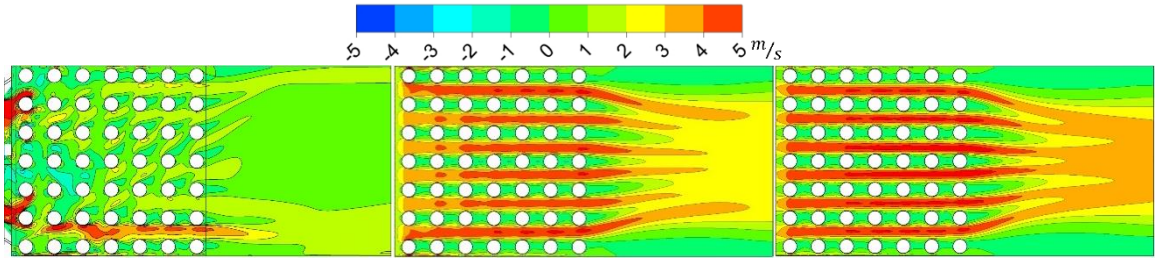


Rotating fan P-Q velocity driven P-Q pressure driven

Figure 4.12 Instantaneous velocity distributions on a plane parallel to the base surface and 1 cm above it.

The results shown in Figure 4.13 correspond to a plane that is 2.5 cm above the base. The flow patterns for the P-Q models in this figure are not materially different from those seen in Figure 4.12. On the other hand, the fan-driven flow is seen to push its way into a limited region of the array as a consequence of the direction of rotation of the fan. Regions of backflow continue to exist within the pin-fin array.

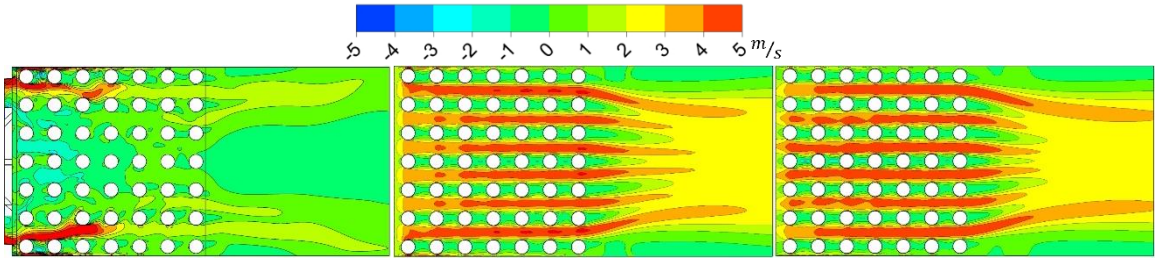


Rotating fan P-Q velocity driven P-Q pressure driven

Figure 4.13 Instantaneous velocity distributions on a plane parallel to the base surface and 2.5 cm above it.

Figure 4.14 conveys results for the fan-driven case on a plane that is 4 cm above the base. The results for the P-Q cases at that level are no different from those already shown in Figures 4.12 and 4.13. The velocity pattern seen in Figure 4.14 strongly reflects the effect of the fan's direction of rotation. Fluid forced into the array passes through it along oblique paths. Many of the zones of backflow have been suppressed.

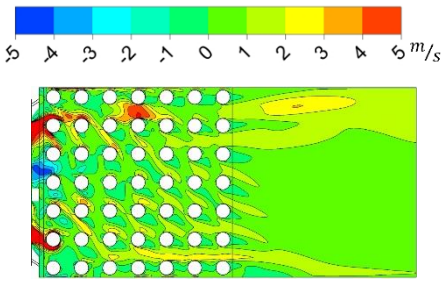


Rotating fan

Figure 4.14 Instantaneous velocity distribution on a plane parallel to the base surface and 4 cm above it.

### 4.6.2 Velocity vectors

The presentation of the velocity-vector results will focus on the case of the fan-driven flow because their complexity deserves elucidation. Figure 4.15 conveys this information, with Parts (a)-(c) corresponding to planes at different elevations above the base. The lengths of the displayed vectors are proportional to the local magnitude of the velocity. In these diagrams, the fan is located at the bottom and the duct exit is at the top.

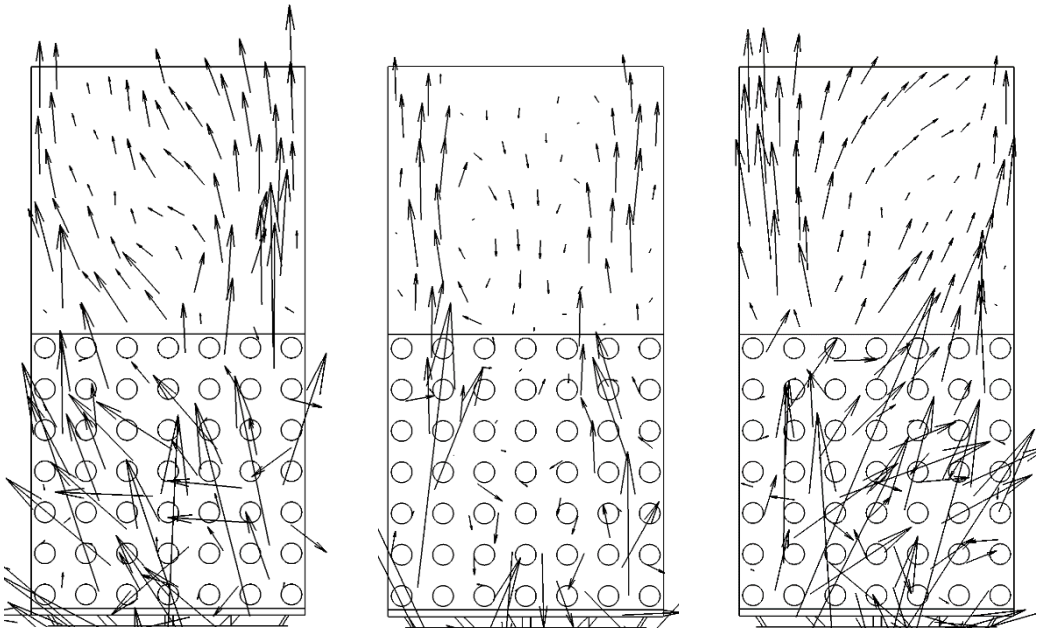

Fan Fan Fan

Figure 4.15 Velocity vectors for the rotating-fan case at planes that are (a) 1, (b) 2.5, and (c) 4 cm above the base.

An overview of Figure 4.15 shows that the flow patterns displayed in Parts (a) and (c) appear to be reversals of each other. In the (a) part, the vector directions of the flow passing through the array have a leftward cant, while in Part (c), the vectors are canted toward the right. The flow direction reversal is also evident in the open duct downstream of the array. The (b) part of the figure displays an altogether different pattern. For one thing, there is evidence of low-velocity backflow in the region away from the sidewalls both within the array and in the downstream duct.

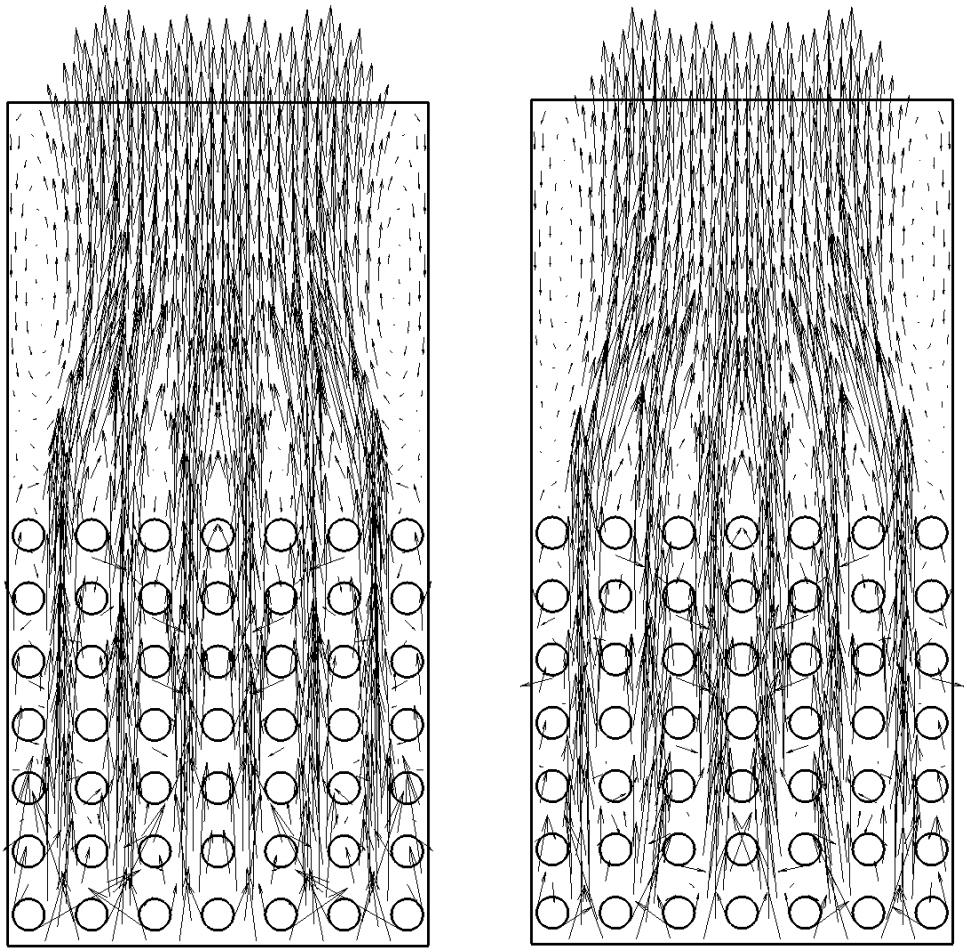

Inflow (a)

Inflow (b)

Figure 4.16 Velocity vectors for the P-Q cases. (a) Velocity-driven, (b) pressure-driven.

The final vector diagram, Figure 4.16, is focused on the flow patterns corresponding to the P-Q model, with the respective parts of the figure corresponding to the velocity-driven and pressure-driven cases. The displayed flow patterns are more-or-less independent of the plane of observation and show no difference between the velocity-driven and pressure-driven cases. Inspection of the figure reveals a very well behaved flow which seeks the unobstructed lanes between the columns of fin fins. Very little flow penetrates the streamwise spaces between successive fins in any one column where there is evidence of recirculating flow. In the downstream duct, the jets emerging from the respective lanes merge. Weak recirculation zones are seen to be present adjacent to the walls of the downstream duct.

## 4.7 Concluding Remarks

The research reported here has demonstrated the importance of properly accounting for the nature of the flow delivered to the inlet cross section of a heat exchanger. Although the best current design protocol makes use of the P-Q curves supplied by the fan manufacturer, the resulting heat transfer predictions are not correct. For one thing, research has shown that the manufacturer-supplied P-Q curves are flawed because no account was taken of the change of the fan performance in the presence of a downstream load. Perhaps of greater significance is that the P-Q model does not take account of the true nature of the flow delivered to the inlet of the heat exchanger. It has been demonstrated here that a more appropriate approach is to consider the fluid mover (e.g., a fan) and the heat exchanger as a single system, thereby enabling them to interact with each other.

The complex flow, including swirl, delivered to the inlet of the heat exchanger by the rotating fan encounters significant fluid resistance within the pin-fin array, with the outcome being a significant reduction in the delivered rate of flowrate compared with that for the P-Q models. Those models envision the delivered flow as uniform and parallel.

From the present numerical solutions for both the fan-delivered and P-Q delivered cases, it was found that the fan-delivered flow was approximately 37% of that of the velocity-driven P-Q flow model. This outcome leads to the expectation of a large reduction of the heat transfer for the fan-driven flow. On the other hand, the actual reductions in the rate of heat transfer obtained from the numerical simulations were modest, no greater than 27%. This outcome can be attributed to the intense mixing of the fan-driven flow within the pin-fin array. That mixing tends to compensate for the diminished flow rate for the fan-driven case.

# CHAPTER 5

# NUMERICAL STUDY OF TURBULENCE INTENSITY EFFECTS AND ASYMMETRIC FLOW OVER A CIRCULAR CYLINDER

## 5.1 Introduction

The effect of freestream turbulence on the fluid flow and heat transfer around the boundary of objects subjected to external flows has attracted considerable interest of the past 75 years; for example, [40, 41]. More recently, studies of internal flows in pipes and ducts have also directed attention to the impact of turbulence intensity at the inlet of the flow space [42]. For both of these situations, different effects of the turbulence were encountered. For the external flows, attention was focused primarily on the response of the skin friction and Nusselt number for a cylinder in crossflow to the magnitude of the turbulence intensity, and to a lesser extent, on the magnitude of the turbulent length scale. On the other hand, for internal flows, the magnitude of the turbulence intensity was shown to have a remarkable effect on the possible relaminarization of the incoming turbulent flow. Of these situations, focus will be directed here to the cylinder in crossflow situation.

The published literature on free stream turbulence effects on a cylinder in crossflow is rather voluminous. For discussion purposes, it is convenient to classify that literature into experimental and analytical work. By far, the amount of experiment work has considerably exceeded that by analysis. Since the outcomes of the experimental work are highly varied and do not lead to definitive conclusions, only a chronological overview is sufficient. In [43], in the early 1970s, experiments at a fixed Reynolds number of 19,000 were performed with a variation of turbulence intensity from 2.5% to 16%. The results for the average Nusselt number were correlated by the means of the parameter $TuRe^{1/2}$, where $Tu$ is turbulence intensity and $Re$ is the cylinder Reynolds number. Later, in 1977, Zukauskas and co-workers [44] reported extensive data for cylinder Reynolds numbers

between $10^5$ and $10^6$, thereby traversing the critical regime. Four different values of turbulence intensity were investigated: 1.2, 2.7, 7, and 15%. The heat transfer results were correlated by the parameter $Tu^{0.2}Re^{0.6}$. Neither [43] nor [44] considered the issue of the turbulence length scale, and both were restricted to the steady state.

In [45], experiments were performed in which the turbulence intensity was varied from 1.5 to 40%. For Reynolds numbers less than 10,000, the heat transfer results at any angular positions depended only slightly on the turbulence intensity. In the final correlation, the average Nusselt number depended on $TuRe^{1/2}$. Once again, scale effects were not considered. The experiments reported by Peyrin and Kondjoyan [46] in 2002 were based on a fixed velocity and a fixed value of the turbulence intensity as turbulence length scale was varied by a factor of two. No effect on the average heat transfer coefficient was observed. More recently, in 2007, experiments were performed [47] for a fixed Reynolds number at which the turbulence intensity was varied at a fixed value of the length scale, and the length scale was varied for a fixed value of the turbulence intensity. For the fixed length scale experiments, the heat transfer increases with increasing turbulence intensity, while for a fixed intensity value $Tu$ = 6.9%, the heat transfer decreased with increasing turbulence length scale.

The foregoing literature review confirms the rather dispersed nature of the experimental information that is available for the cylinder in crossflow. For the most part, the flow was considered to be steady and the turbulence length scale was regarded as a secondary variable.

The analytical work relating to the effects of freestream turbulence are generally approximate and based on simplifying assumptions so that a general overview is sufficient. In 1966, [48], performed an analysis of the flow at the stagnation point of a cylinder in crossflow. The eddy viscosity is assumed to be proportional to the turbulence in the freestream, the proportionality constant being determined from the experimental data. The governing equations were the boundary layer equations for incompressible flow

near the stagnation point. In 1979, [49] analytically investigated the effects of freestream turbulence and turbulence length scale on skin friction and heat transfer. The analysis was confined to the steady state and to phenomena that are upstream of angular positions that are 60-70 degrees from the stagnation point, thereby ignoring the wake region of the cylinder.

In 1982, Gorla and co-workers [50] used a boundary layer model to study turbulence effects in the steady state, with a major emphasis on the stagnation point. The solution approach was the approximate local similarity method and irrotational potential flow inviscid flow was assumed for the freestream. The eddy diffusivity model was adjusted to achieve agreement with the experimental data. For a given length scale, the Nusselt number increases with increasing value of $TuRe^{1/2}$. The Zukauskas group [51] used a very simple model for the thermal boundary layer to predict the variation of the heat transfer coefficient as a function of angular position for *Re* ranging from $5.5 \times 10^4$ to $2.03 \times 10^6$ and for *Tu* = 1.5% without any concern for the length scale.

## 5.2 Modeling and Numerical Simulations

The physical situation to be solved by numerical simulation is depicted in Figure 5.1. As seen there, a circular cylinder is situated in crossflow in a uniform upstream freestream. The turbulence intensity of the freestream flow is a major independent variable of the work, with the Reynolds number being a second independent variable. Heat transfer is a major focus and heat transfer results are detailed at all angular positions of the cylinder surface.

The fluid flow is turbulent, two-dimensional, and both steady and transient flows are considered. The solution domain extends significantly upstream, downstream, and laterally with respect to the cylinder proper. Thanks to the availability of large computer resources, the use of high quality meshes was achievable. The software package, ANSYS

CFX 16.1, is employed as the numerical simulation tool. The residual target for convergence was $10^{-6}$ or smaller. It was found that a time step as small as 0.0005 seconds was necessary to resolve the unsteadiness of both the fluid flow and the heat transfer.

The extent of the solution domain is picture schematically in Figure 5.1. As seen there, the upstream boundary of the domain is situated 10 cylinder diameters before the stagnation point, and the downstream extension of 50 diameters was chosen to be large enough to enable wake effects to be properly dealt with. The lateral extension of the solution domain was chosen to be 15 diameters at either side of the cylinder. The range of considered Reynolds numbers extended from 10,000 to 50,000.

Two thermal boundary conditions at the cylinder surface were investigated: (a) uniform temperature and (b) uniform wall heat flux. The freestream temperature at the upstream boundary of the solution domain was specified as being uniform across the span of the boundary. At that boundary, the value of the freestream turbulence was varied from 1, 5, and 10%, also uniform across the span of the upstream boundary. Also uniform across the span was the axial velocity whose specification resulted in the Reynolds numbers that were referenced earlier. The two lateral boundaries seen in Figure 5.1 were assigned an *opening* boundary condition so that fluid was free to enter or leave at will. At those boundaries, the pressure was specified as the ambient value. The boundary at the downstream end of the solution domain was also taken to be an opening, with the pressure also as ambient. At all the boundaries that were specified as openings, the direction of the flow was determined by means of the direction of entrainment. Whenever there is a fluid inflow at an opening boundary condition, the temperature of the ambient is conveyed into the solution domain.

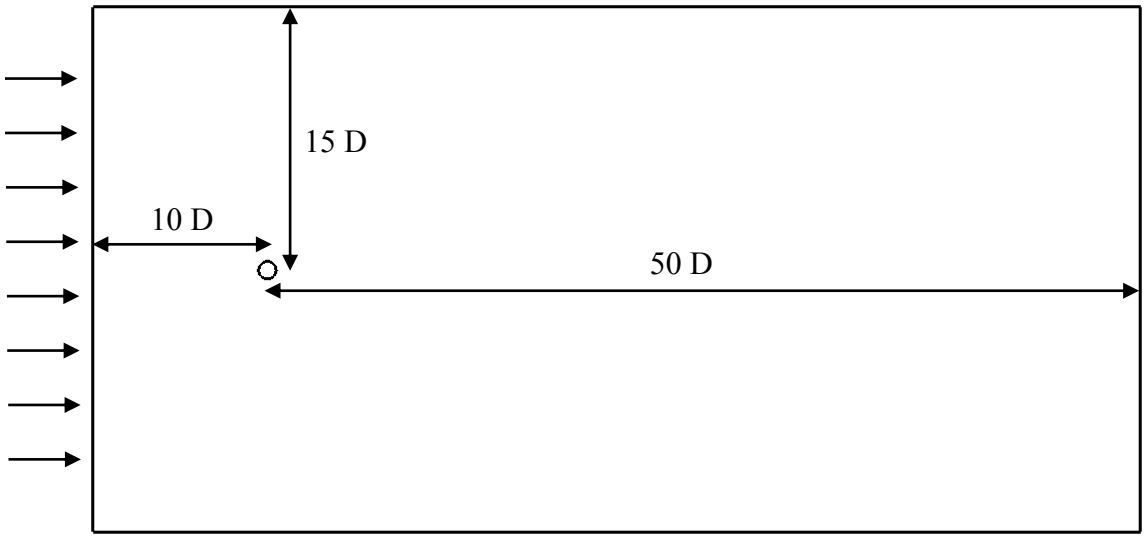


Figure 5.1 Plan view of the solution domain for the numerical simulations.

To compete the geometrical descriptions of the problem in question, the relevant angular coordinates are displayed in Figure 5.2. The origin of coordinates ($\theta = 0^o$) is situated at the forward stagnation point of the cylinder. Note that the coordinate system recognizes both positive and negative values of the angle.

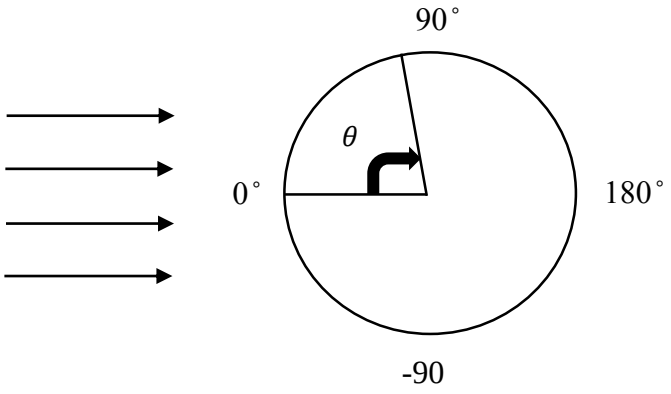


Figure 5.2 Definition of the angular coordinates for a circular cylinder in crossflow.

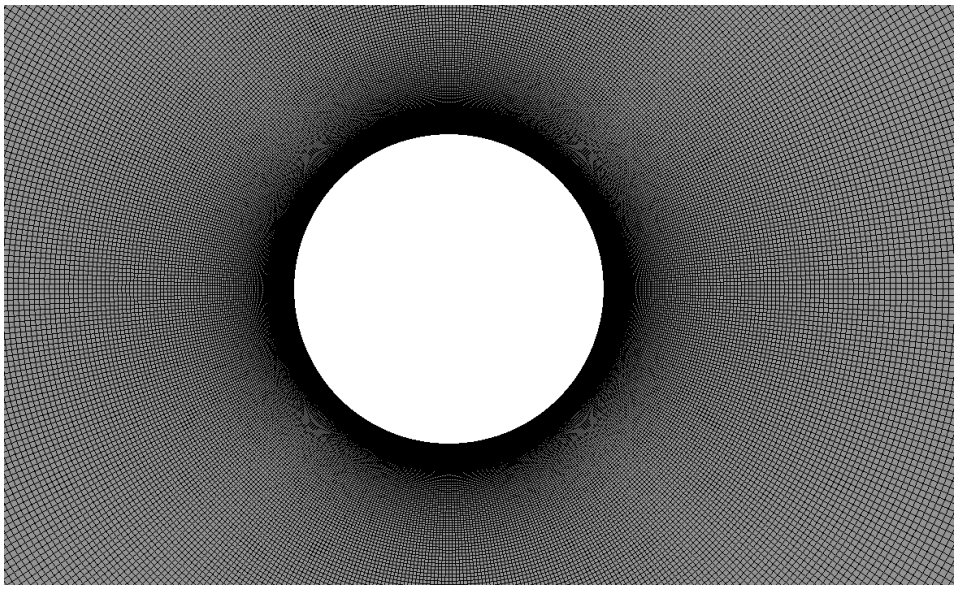

Figure 5.3 Final version of the mesh in the neighborhood of a circular cylinder

The quality of any numerical solutions is highly dependent on the mesh used to discretize the solution space. It is a necessary part of numerical simulation work to demonstrate that the solutions obtained are independent of the nature of the mesh. Making use of different types of meshes and varying the number of nodes are key factors in the verification of mesh independence. In particular, two meshes, each respectively consisting of one-million and 1.8-million nodes, were employed for the mesh independence study. Figure 5.2 displays the mesh in the near neighborhood of the cylinder. Immediately adjacent to the cylinder surface, the mesh is so fine as to appear continuous. The metric selected for the evaluation of mesh independence was the overall heat transfer rate for the entire surface of the cylinder. For the one-million node mesh, the heat transfer rate was 137.40 Watts per meter of cylinder length. In contrast, for the 1.8-million node mesh, the corresponding heat transfer was 137.71 Watts per meter of cylinder length. The difference between these results is approximately 0.2%. This level of agreement was taken to be strong testimony as to the validity of the numerical simulation methodology.

## 5.3 Governing Equations

The governing differential equations that describe the fluid flow and heat transfer processes are similar to those that have been used in Chapter Two, but with a significant change. That change is that the steady-state model utilized in that chapter has to be transformed to an unsteady model expressed by terms such as $\frac{\partial u_j}{\partial t}$. Momentum conservation is expressed by the RANS equations displayed in equation (2.1) and modified with foregoing time-dependent term. The mass conservation equation, (2.3), remains as before because the density is assumed be constant. Also, the energy conservation equation, (2.7), can be used here after the unsteady term $\rho c_p \frac{\partial T}{\partial t}$ is appended to it.

The aforementioned equations require a turbulence model to complete them. Based on the arguments used to justify its use in preceding chapters of this thesis, the SST *k-ω* (Shear Stress Transport) turbulence model has been used here for the current numerical simulations. One major difference between the use of SST *k-ω* model in the preceding chapter and its use here is that previously, the freestream turbulence was not needed to be specified. Here, however, the freestream turbulence *Tu* is a major independent variable and is thereby specifiable. The definition of *Tu* is

$$Tu = \frac{rms\ value\ of u'}{u_{ave}} = \frac{\sqrt{\frac{1}{t^*}\int_0^{t^*} u'^2 dt}}{u_{ave}} \times 100\% \tag{5.1}$$

$$u'(x, y, z, t) = u\,(x, y, z, t) - u_{ave}\,(x, y, z) \tag{5.2}$$

The quantity $u'$ is termed the instantaneous turbulent fluctuation velocity in the streamwise direction. It is the difference between the instantaneous velocity and the time average velocity $u_{ave}$ at the point in question. The decomposition indicated in equation

(5.2) is the basis by which the Navier-Stokes equations are transformed to the RANS equations.

The overwhelming majority of the numerical work of this chapter was performed making use of the SST $k$-$\omega$ model. The governing equations for that model are displayed as equations (4.4) to (4.6).

However, in order to demonstrate that the results produced by the use of that model are not specific to it, another turbulence model was used to a lesser extent. That alternative model is the SAS-SST model (SAS: Scale Adaptive Simulation). It adapts the length scale automatically to the resolved scales of the flow field. The distinguishing factor in the model is the use of the von Karman length scale which is a three-dimensional generalization of the classic boundary layer definition. The governing equations of the SAS-SST model differ those of the SST $k$-$\omega$ model by an additional source term in the transport equation for the turbulence eddy frequency $\omega$.

## 5.4 Local Instantaneous Heat Transfer Results

The presentation of the local instantaneous heat transfer results will encompass three independent variables: (a) turbulence intensity ($Tu$ = 1, 5, and 10%), (b) Reynolds number ($Re$ = 50,000), (c) angular position ($\theta$ = 0 to 360 degrees), and (d) time (t = 1 to 1.1s). In truth, results were also obtained for Reynolds number of 10,000, but are not shown here because of their length and also because they did not differ qualitatively from those for $Re$ = 50,000. Note also that the time coordinate used for the presentation did not begin at the very outset of the numerical simulations. Rather, the start of the time scale was selected after a more or less repeating time dependence had been developed. The resulting time scale on the figures to be presented ranged from one to 1.1 seconds.

In order to achieve an orderly presentation of results, the angular space extending from 0 to 360 degrees was subdivided into four quadrants: (a) 0 to 90 degrees, (b) 0 to -90 degrees, (c) 90 to 180 degrees, and (d) -90 to -180 degrees. This subdivision recognizes that important fluid flow and heat transfer events are not symmetric above and below the diametral plane (a straight line extending from (θ = 0 to 180). The boundary condition on the surface of the cylinder was fixed at a uniform heat flux.

The layout of the figures proceeds as follows: For a given turbulence intensity, the figures are grouped according to a single figure number but with parts (a) – (d) for the respective angular quadrants 0 to 90 degrees, 0 to -90 degrees, 90 to 180 degrees, and -90 to 180 degrees. In each of the parts of the figures, there are ten curves, each of which corresponds to a given angular position. Note that each cluster of four figures corresponds to a Reynolds number of 50,000, to the uniform heat flux boundary condition, and to a fixed turbulence intensity. There are three such clusters corresponding respectively to *Tu* = 1, 5, and 10%. Each cluster is conveyed by Figures 5.4, 5.5, and 5.6. The heat transfer results are presented in terms of the spatially and timewise varying local Nusselt number *Nu*. As a first step in evaluating Nu, a local/temporal heat transfer coefficient *h* is defined as

$$h = \frac{q}{(T_w - T_\infty)} \tag{5.3}$$

Since the results to be presented in Figures 5.4 – 5.6 correspond to the uniform heat flux boundary condition on the cylinder surface, the local wall temperature varies with the angle θ and is evaluated as such. The ambient temperature $T_\infty$ that appears in the defining equation for *h* is a constant. Once *h* was determined, it was represented in dimensionless form by the Nusselt number defined as

$$Nu = \frac{hD}{k} \tag{5.4}$$

in which $D$ is the cylinder diameter, and $k$ is the thermal conductivity of the flowing air at 25 $^oC$.

Attention is first turned to Figure 5.4 which is for 1% turbulence intensity. By inspection of the (a) part of the figure, it is seen that for angular locations up to 50 degrees, the local Nusselt number curves are virtually independent of time. As the angular coordinate θ increases, the timewise fluctuations increase to a maximum at the 80-degree location and diminish slightly at the 90-degree location. Next, it is appropriate to look at the counterpart situation displayed in Figure 5.4 (b) which corresponds to angles in the range from 0 to -90 degrees. A comparison of Figures 5.4 (a) and (b) indicates that there are hardly any differences between the heat transfer results for the upper and lower portions of the cylinder. In particular, the fluctuations begin at θ = ± 50 degrees for the two situations, and the subsequent fluctuation magnitudes are more or less same. One difference is that the respective fluctuations are out of phase: the maximum for one of the traces occurs at the same time as does the minimum for the other traces. This is an important finding, because others in the past [52 and 53] have assumed that the results for the positive and negative angular positions are the same.

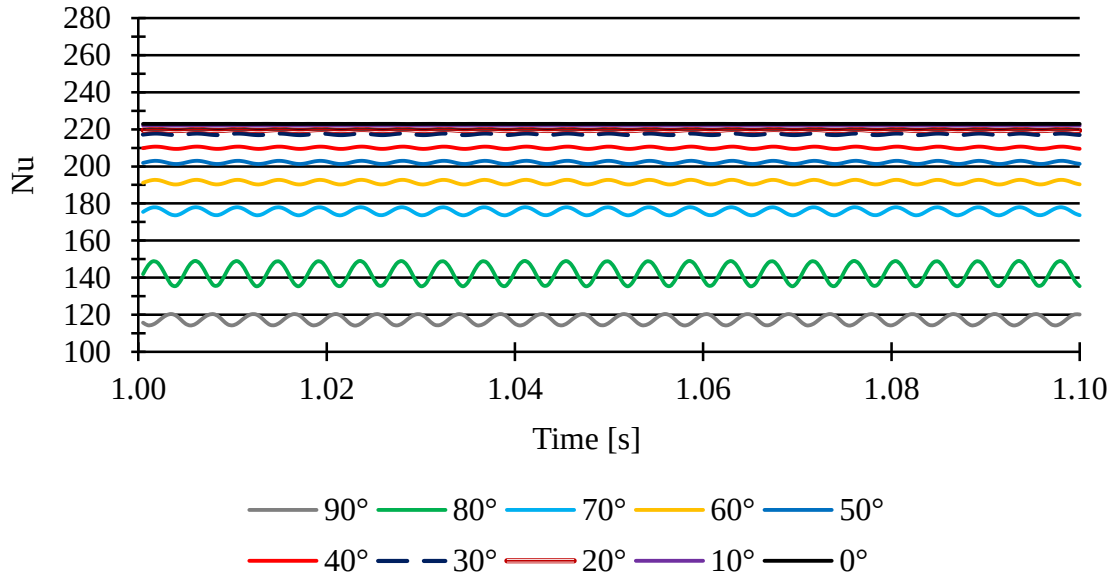


Figure 5.4 (a) Local *Nu* numbers from 0 to 90 degrees varying with time [*Tu* = 1%, *Re* = 50,000, and $q_w$ = uniform].

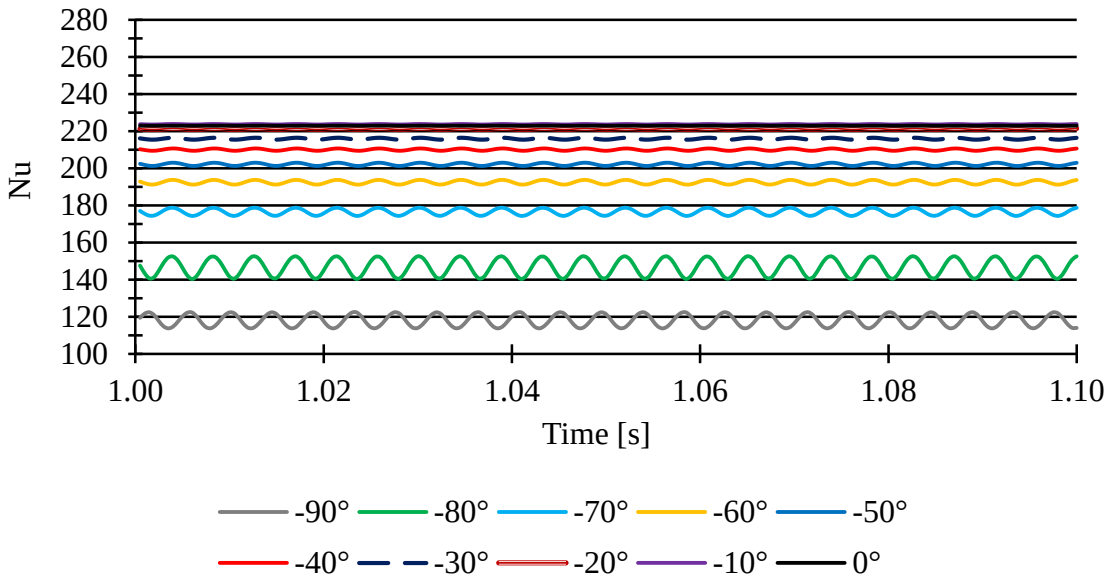


Figure 5.4 (b) Local *Nu* numbers from 0 to -90 degrees varying with time [*Tu* = 1%, *Re* = 50,000, and $q_w$ = uniform].

Attention is next directed to heat transfer results for the back side of the cylinder. Once again, separate figures are displayed for angles between 90 and 180 degrees and for angles between -90 and 180 degrees. These results are respectively conveyed in Figures 5.4 (c) and 5.4 (d). For the Nusselt numbers for the positive angles, fluctuations are in evidence at all angular locations. Between 90 and 130 degrees, the fluctuations are moderate. However, for larger angles, considerably larger fluctuations are seen. The largest fluctuations occur at an angle of 160 degrees. With regard to the results shown in Figure 5.4 (d) for negative angles, the pattern of the fluctuations is similar to that shown in the preceding figure. The major difference is the phase of the respective fluctuations; that is, the maximum of one of the fluctuations occurs when the other fluctuations are at a minimum.

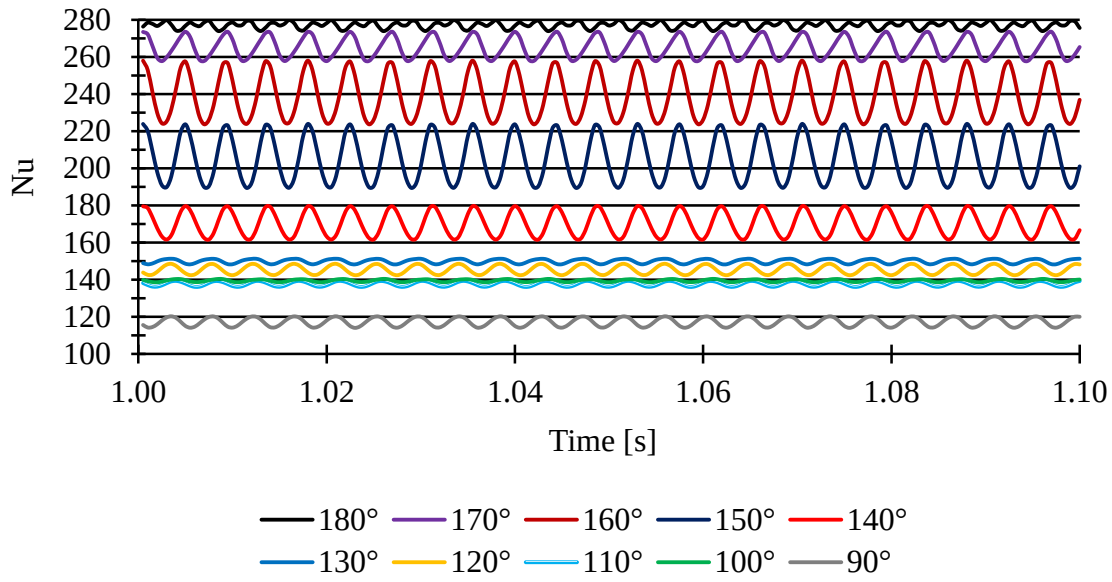


Figure 5.4 (c) Local *Nu* numbers from 90 to 180 degrees varying with time [*Tu* = 1%, *Re* = 50,000, and $q_w$ = uniform].

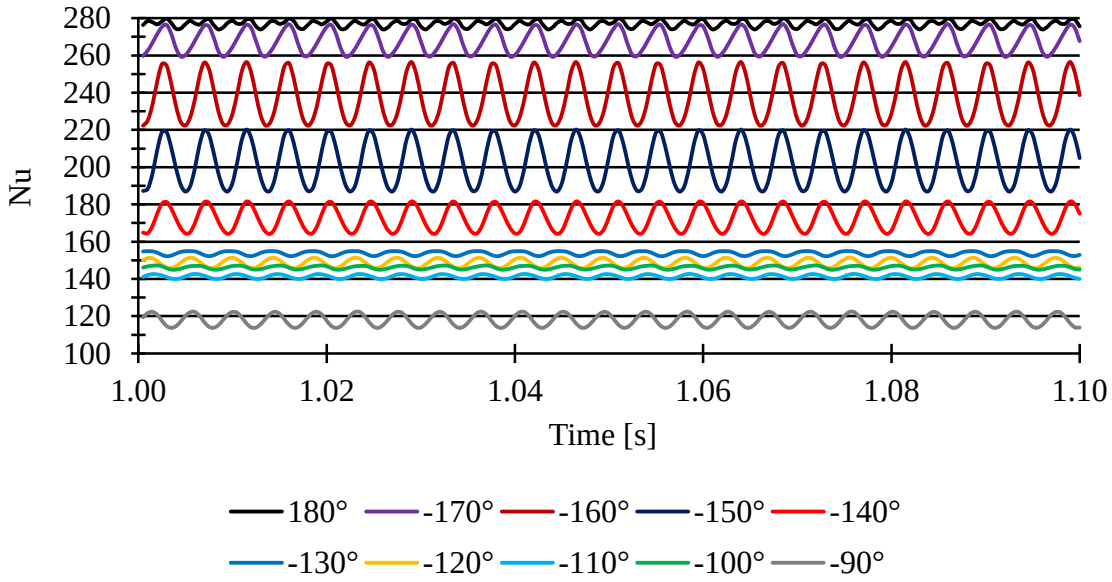


Figure 5.4 (d) Local *Nu* numbers from -90 to -180 degrees varying with time [*Tu* = 1%, *Re* = 50,000, and $q_w$ = uniform].

The second sets of figures, Figures 5.5, to be presented correspond to an inlet value of turbulence intensity of 5%. The format for these figures follows that already used for the results for the 1% turbulence intensity. Observation of Figure 5.5 (a) and comparison with Figure 5.4 (a) shows that the magnitude of the fluctuations, when they occur, is smaller for the higher initial turbulence. A comparison between Figure 5.5 (a) and (b) shows the phase difference that has already been mentioned in connection with the earlier figures of this group.

For the back-side Nusselt numbers, Figure 5.5 (c) and (d) can be consulted. Here again, the major fluctuations occur for angles $\theta$ of $\pm 140$ degrees and larger. The angular zone of larger fluctuations is between 140 and 170 degrees. At $\theta = 180$ degrees, the magnitude of the fluctuations tends to decrease.

The last set of figures in this segment of the results extends the range of inlet turbulence intensity to 10%, and Figures 5.6 (a) – (d) have been prepared for this purpose. Focus is first directed to Figure 5.6 (a) which corresponds to positive angles on the forward upper half of the cylinder. One immediate difference to be noted here is that the magnitudes of the Nusselt numbers are larger than for the previous counterpart Figures 5.4 (a) and 5.5 (a). In the current figure, 5.6 (a), it is noteworthy that the largest magnitude of the fluctuations occurs at the $\theta = 90$ degrees angular position. These similar findings may be seen in Figure 5.6 (b) which corresponds to the negative angles 0 to -90 degrees. The noteworthy difference between the two figures is that the phases are different. In particular, the maximum Nusselt numbers in Figure 5.6 (a) occur at the same time that the minimum Nusselt numbers are achieved in Figure 5.6 (b). The final discussion item relates to the back face of the cylinder. For this, results are displayed in Figures 5.6 (c) and (d) respectively. These figures show that the angular zone of maximum Nusselt number fluctuations is in the range of 150 to 160 degrees. Again, the aforementioned phase shift in the time dependence of Nusselt numbers between the positive and negative angles can be seen.

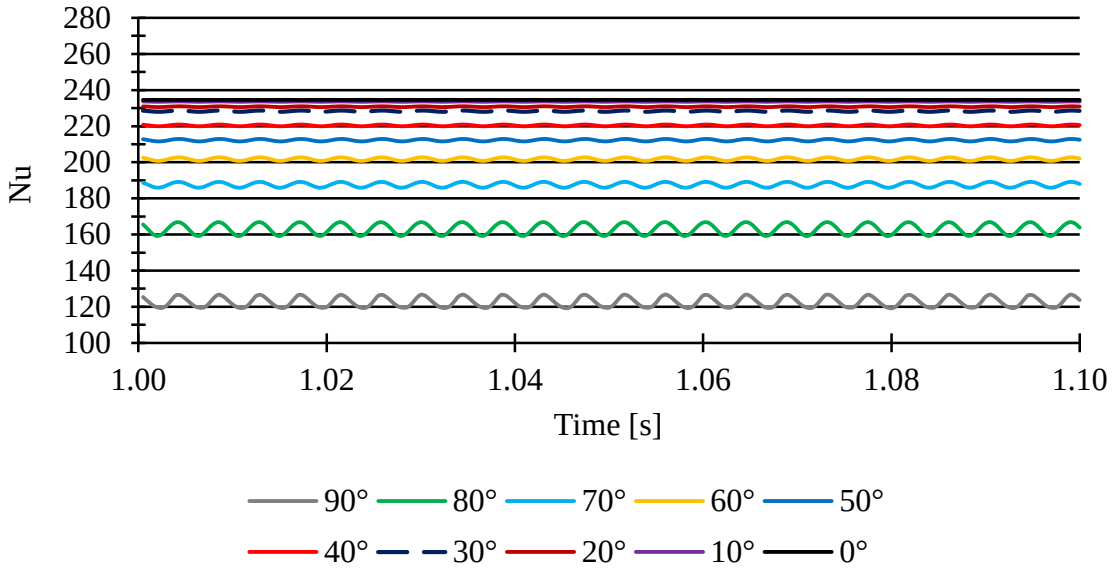


Figure 5.5 (a) Local *Nu* numbers from 0 to 90 degrees varying with time [*Tu* = 5%, *Re* = 50,000, and $q_w$ = uniform].

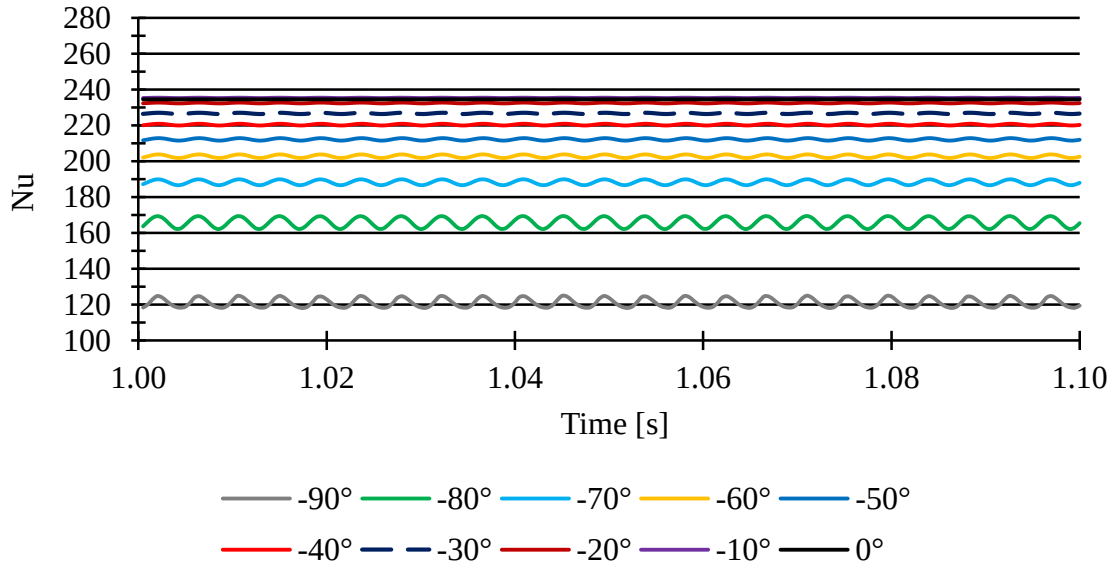


Figure 5.5 (b) Local *Nu* numbers from 0 to -90 degrees varying with time [*Tu* = 5%, *Re* = 50,000, and $q_w$ = uniform].

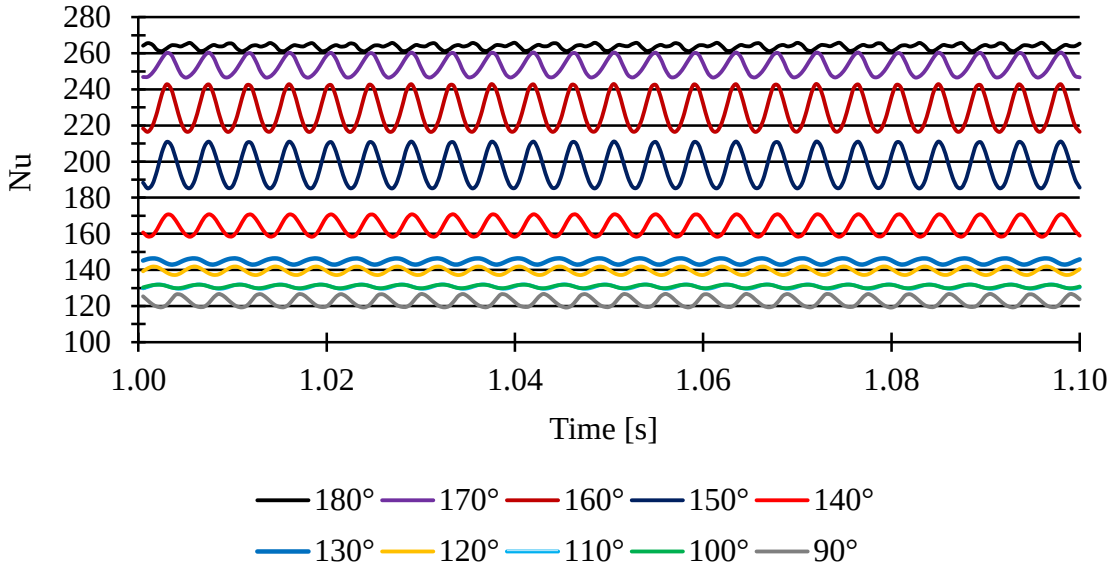


Figure 5.5 (c) Local *Nu* numbers from 90 to 180 degrees varying with time [*Tu* = 5%, *Re* = 50,000, and $q_w$ = uniform].

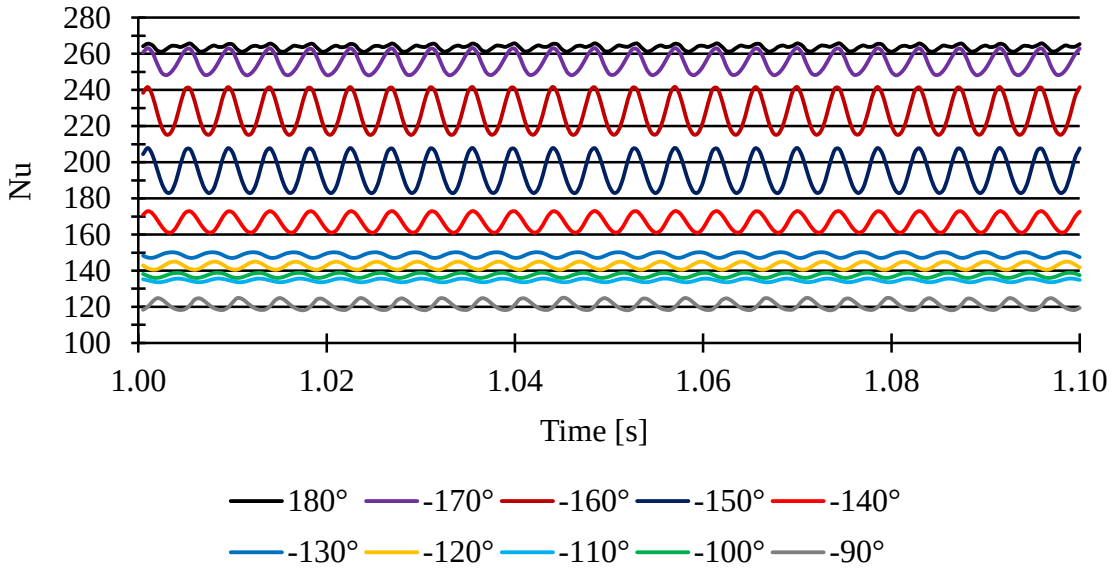


Figure 5.5 (d) Local *Nu* numbers from 90 to -180 degrees varying with time [*Tu* = 5%, *Re* = 50,000, and $q_w$ = uniform].

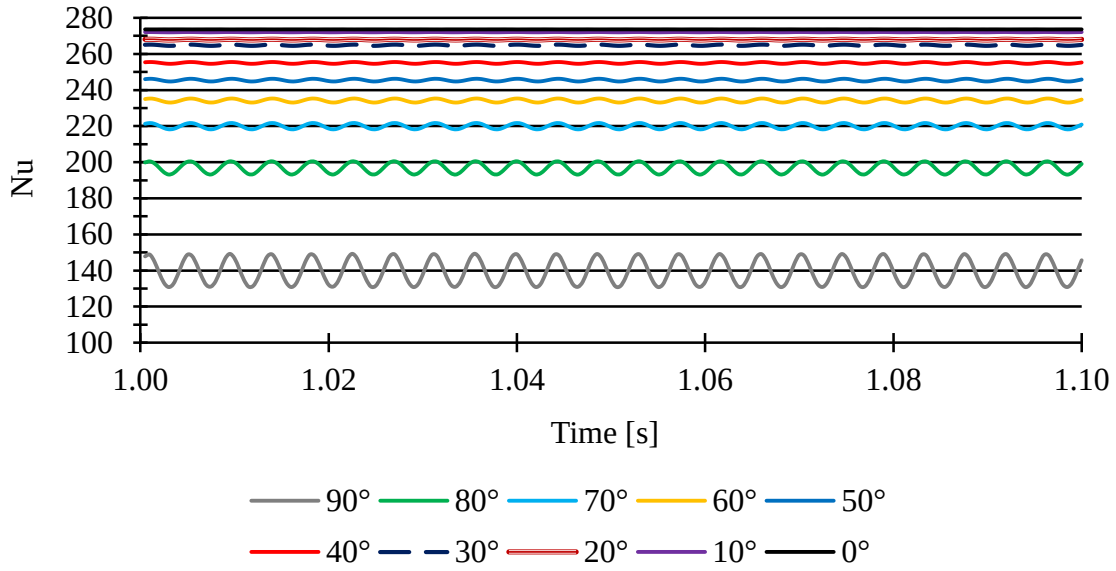


Figure 5.6 (a) Local *Nu* numbers from 0 to 90 degrees varying with time [*Tu* = 10%, *Re* = 50,000, and $q_w$ = uniform].

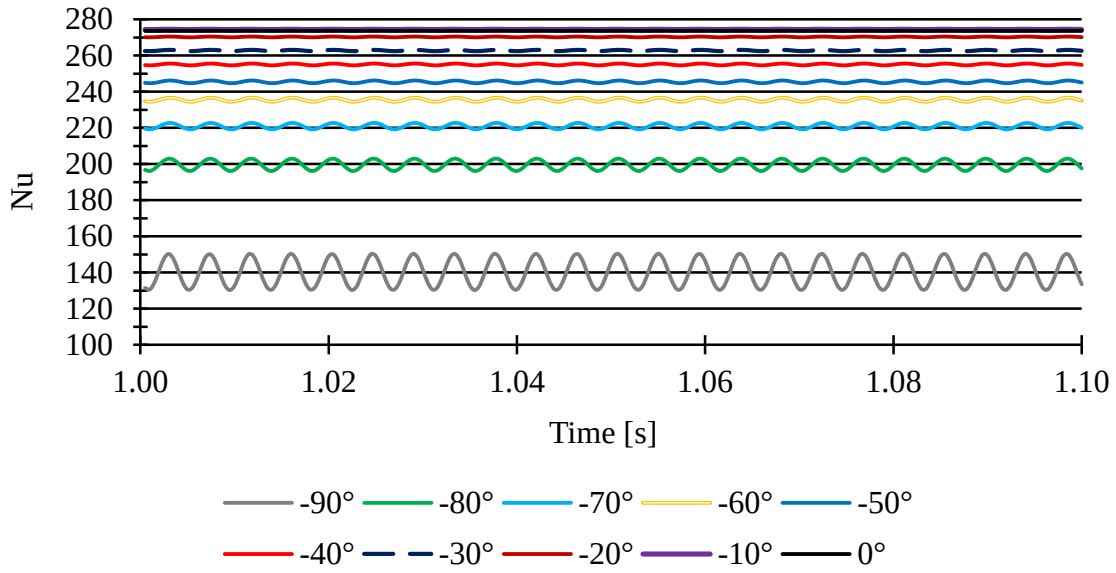


Figure 5.6 (b) Local *Nu* numbers from 0 to -90 degrees varying with time [*Tu* = 10%, *Re* = 50,000, and $q_w$ = uniform].

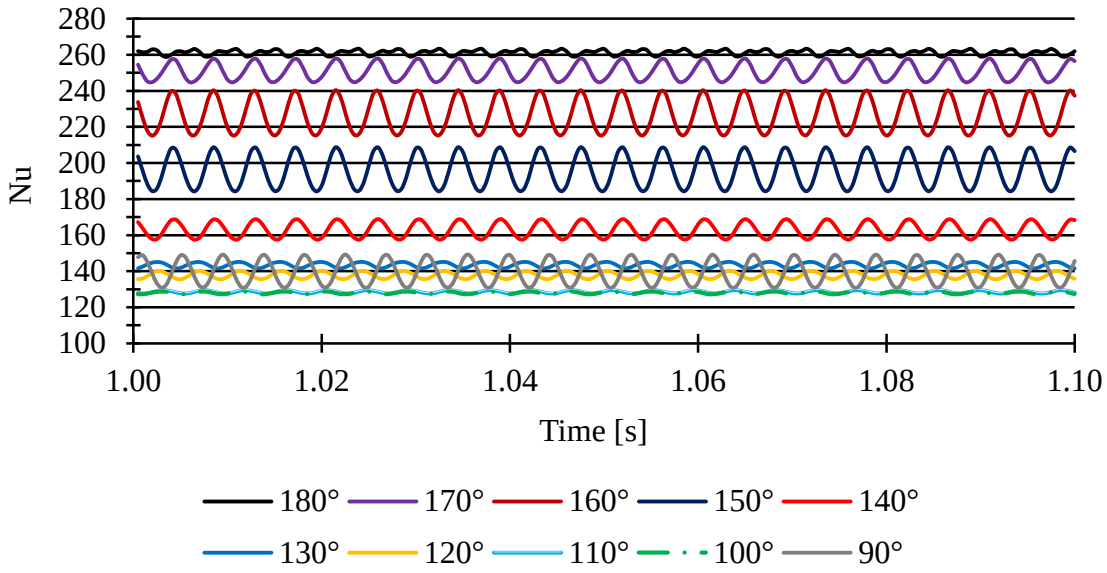


Figure 5.6 (c) Local *Nu* numbers from 90 to 180 degrees varying with time [*Tu* = 10%, *Re* = 50,000, and $q_w$ = uniform].

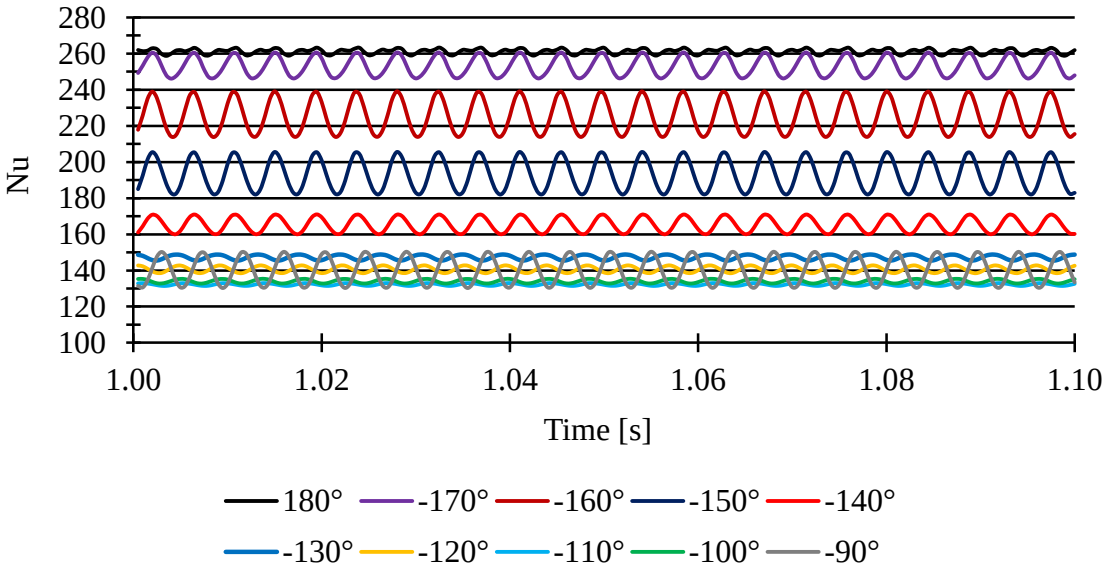


Figure 5.6 (d) Local *Nu* numbers from -90 to -180 degrees varying with time [*Tu* = 10%, *Re* = 50,000, and $q_w$ = uniform].

Since the frequency of the oscillations in the local *Nu* number varies with the *Tu* value, this information can be expressed in dimensionless form by evaluating Strouhal number (*St*). If *f* is the frequency of local *Nu* number, *D* is the characteristic length (diameter), and, *U* is the flow velocity then *St* follows as

$$St = \frac{fD}{U} \tag{5.5}$$

Table 5.1 *St* at frontal and rearward cylinder locations for *Re* = 10,000 and 50,000.

| | *Re* = 10,000 | | *Re* = 50,000 | |
|---|---|---|---|---|
| | Front | Back | Front | Back |
| *Tu* = 1% | 0.230 | 0.230 | 0.190 | 0.190 |
| *Tu* = 5% | 0.223 | 0.223 | 0.194 | 0.194 |
| *Tu* = 10% | 0.217 | 0.217 | 0.192 | 0.192 |

For *Re* = 50,000, *St* is insensitive to the turbulent intensity, but for *St* decreases slightly with increasing *Tu*. Furthermore, the magnitude of *St* is somewhat larger for *Re* =10,000 than for *Re* = 50,000. The front- and rear-face *St* values are identical.

## 5.5 Local Time-average Heat Transfer Results

The next category of result to be presented here, Figures 5.7 (a) and (b), are time-averaged, spatially varying Nusselt numbers. These figures correspond respectively to Reynolds numbers of 10,000 and 50,000. This is an especially important category because in the experimental literature in which there were no unsteady results identified, the presentation was limited to a display of spatial variations. The time averaging was performed over the range of time between 1s and 1.1s. These are the times for which information was displayed in Figure 5.4-5.6. Clearly, during that range of times, periodic fluctuations had already set in.

The heat transfer results are presented in terms of the time-average, spatially varying Nusselt number, $\overline{Nu}(\theta)$. A time-average, spatially varying heat transfer coefficient $\bar{h}(\theta)$ to evaluate $\overline{Nu}(\theta)$ is defined as

$$\bar{h}(\theta) = \frac{q}{(\overline{T_w}(\theta) - T_\infty)} \tag{5.6}$$

Since the results to be presented in Figure 5.7 correspond to the uniform heat flux boundary condition on the cylinder surface, the time-average, spatially varying wall temperature is evaluated as $\overline{T_w}(\theta)$. $\bar{h}(\theta)$ of Equation (5.5) can be converted to the dimensionless form which is the time-average, spatially varying Nusselt number by the definition

$$\overline{Nu}(\theta) = \frac{\bar{h}(\theta)D}{k} \tag{5.7}$$

For the easier comparison of the dimensionless heat transfer values for different Reynolds number, $\overline{Nu}(\theta)$ is divided by $\sqrt{Re}$. This normalization is frequently used in the published literature to facilitate comparisons of results for different values of *Re*.

$$(\overline{Nu}(\theta))/\sqrt{Re} = \frac{\bar{h}(\theta)D}{k}\frac{1}{\sqrt{Re}} \tag{5.8}$$

Figure 5.7 shows the angular distribution of the Nusselt number for the three investigated turbulence levels *Tu* and for the upper face (positive angles) and the lower face (negative angles). The (a) and (b) parts of the figure are for Re = 10,000 and 50,000 respectively.

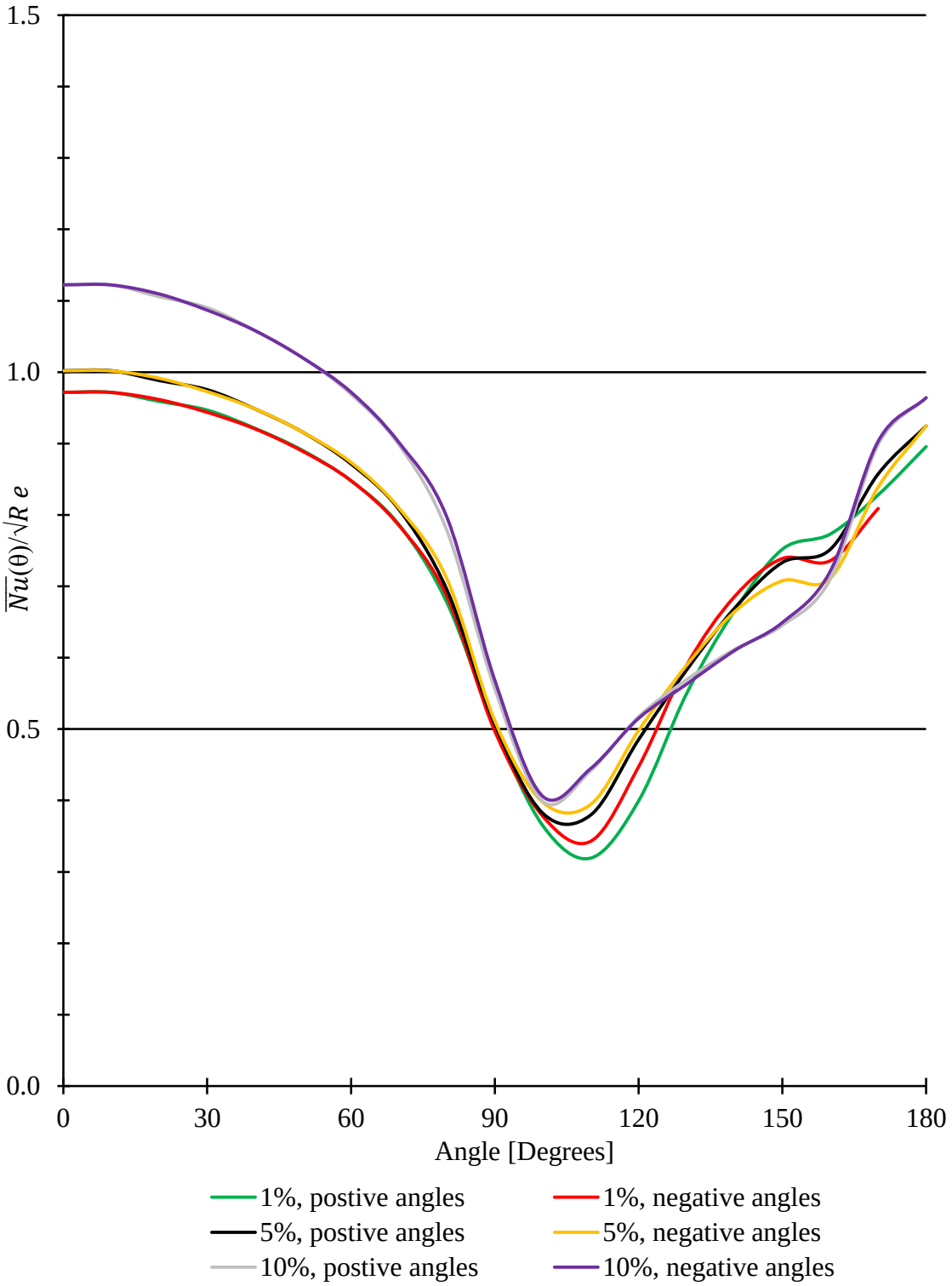


Figure 5.7 (a) Dimensionless time-average, spatially varying $(\overline{Nu}(\theta))/\sqrt{Re}$ as a function of θ [*Re* = 10,000, and $q_w$ = uniform].

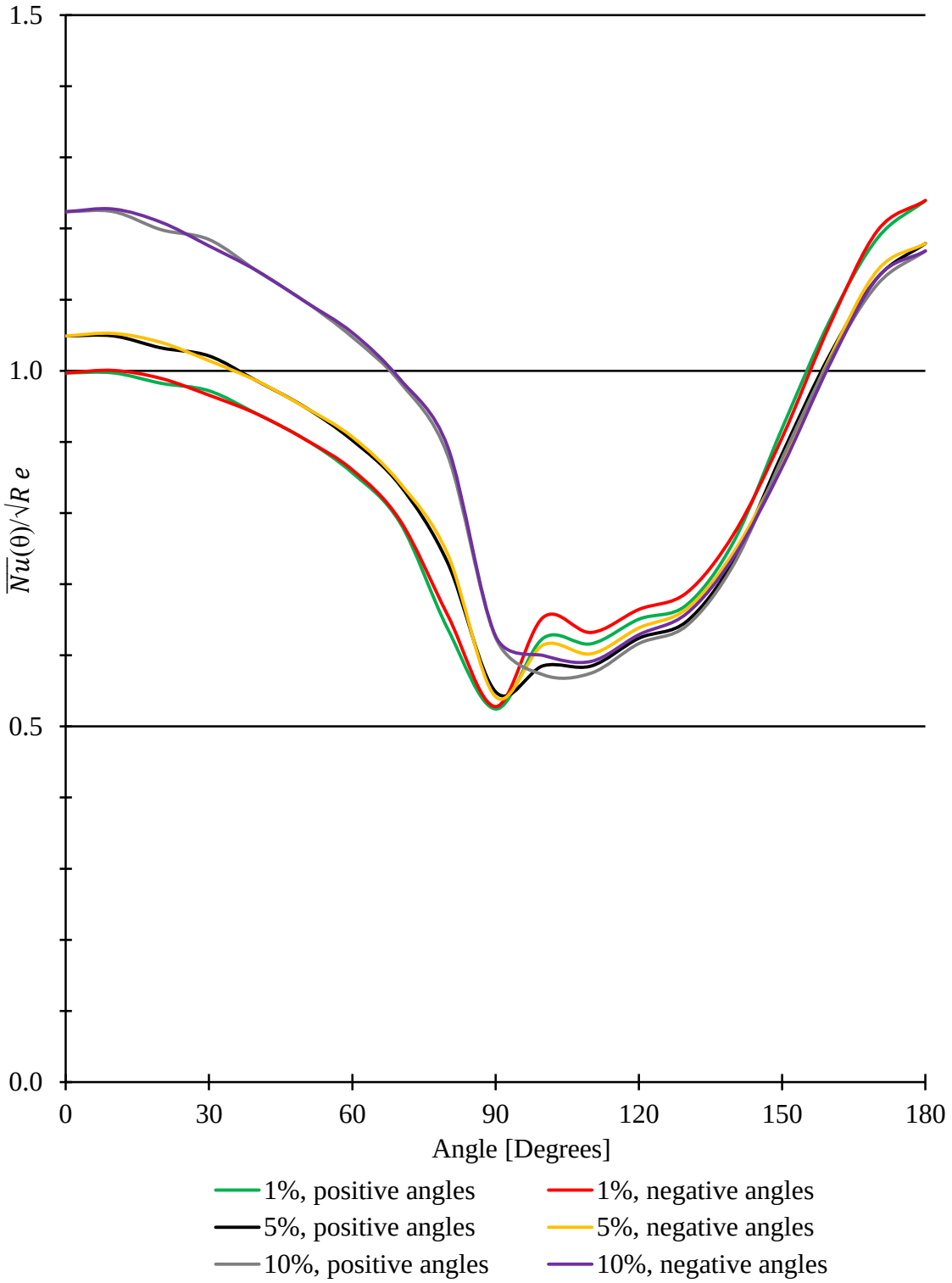


Figure 5.7 (b) Dimensionless time-average, spatially varying $(\overline{Nu}(\theta))/\sqrt{Re}$ as a function of θ [*Re* = 50,000, and $q_w$ = uniform].

Figure 5.7 (a) and (b) show the dimensionless time-average $\overline{Nu}(\theta))/\sqrt{Re}$ profiles achieved from the current study for two Reynolds numbers, *Re* = 10,000 and 50,000. These clearly show that the case for Re = 50,000 has a higher dimensionless heat transfer values. The $(\overline{Nu}(\theta))/\sqrt{Re}$ for the higher Reynolds number is greater than that for the lower Reynolds number over the entire circumference of the cylinder. Another conclusion that can be drawn from Figures 5.7 (a) and (b) is that √Re is not a suitable power of Re for bringing together the results for different Re.

Furthermore, the figures also demonstrate the effect of the turbulence intensity on heat transfer. In particular, $(\overline{Nu}(\theta))/\sqrt{Re}$) increases with increasing *Tu* until separation of the boundary layer begins for both Reynolds numbers. For different Reynolds numbers, boundary layer separation occurs at slightly different angular positions. For both for Reynolds numbers, it occurs around $\theta = 90^o$ - $110^o$. However, smaller *Tu* gives rise to smaller angles for *Re* = 10,000, and vice versa for Re = 50,000. At the larger Reynolds number, the high turbulence case displays rather flat minima at separation. After the separation, higher *Tu* does not guarantee higher heat transfer values in the wake region.

Another feature is the unsymmetric behavior of dimensionless heat transfer values. Specifically, $(\overline{Nu}(\theta))/\sqrt{Re}$) for corresponding positive angles and negative angles are lightly different especially around separation regions. This is crucial observation, since others in the past [52, 53] have assumed that the results for the positive and negative angular positions are the same.

## 5.6 Spatial-average, Time-varying Heat Transfer Results

The spatial-average, time varying Nusselt number $\overline{Nu}(t)$ are shown in Figure 5.8 (a) - (d). The (a) and (b) parts are for *Re* =10,000, whereas the (c) and (d) parts are for *Re* = 50,000. The figures show results for both for uniform wall temperature, (a) and (c) parts, and for uniform wall heat flux, (b) and (d) parts. As seen there, there is timewise periodic

fluctuation for both boundary conditions and both Reynolds numbers. The amplitude of fluctuations for the uniform heat flux case is smaller than those for the uniform temperature case and a similar trend occurs with increasing Reynolds number. On the other hand, increasing Reynolds number gives rise to higher spatial-average Nusselt numbers as found in other literature [47].

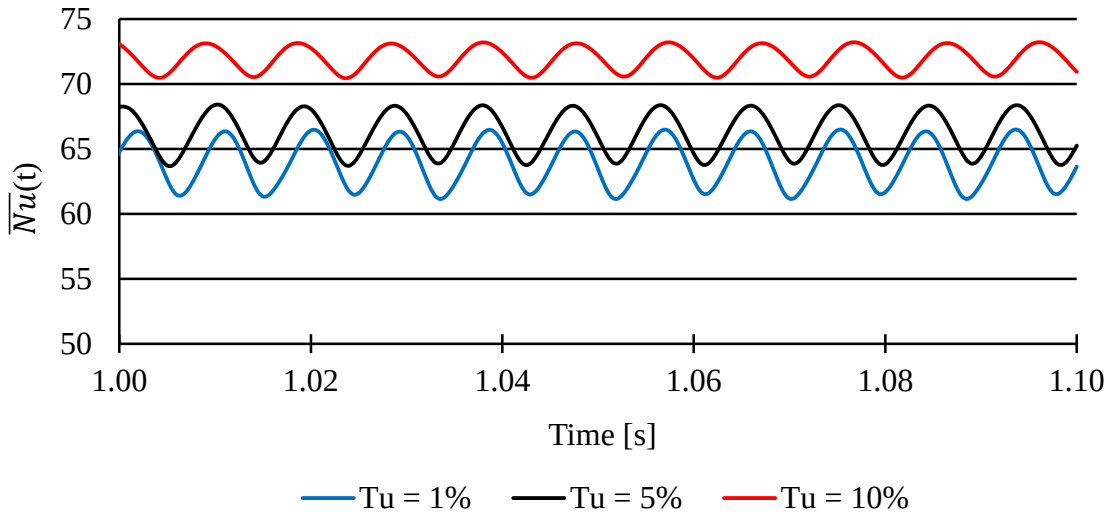


Figure 5.8 (a) All-angle-average spatial average $\overline{Nu}$(t) numbers varying with time, [$Re$ = 10,000, $T_w$ = uniform].

In all four figures from Figure 5.8 (a) to Figure 5.8 (d), it is obvious that higher turbulence intensity causes higher dimensionless heat transfer. Similar evidence has been found in other literature [45, 47]. It is noteworthy that the time-average Nusselt number difference between 5% and 10% turbulence intensities is much larger than that between 1% and 5% turbulence intensity at the higher Reynolds number.

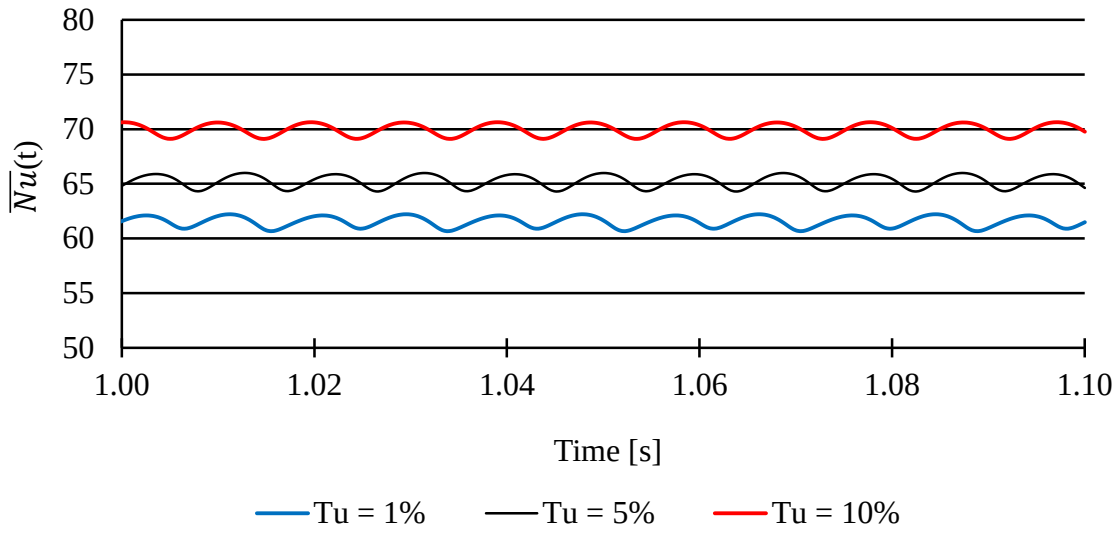


Figure 5.8 (b) All-angle-average spatial average $\overline{Nu}(\mathrm{t})$ numbers varying with time, [*Re* = 10,000, $q_w$ = uniform].

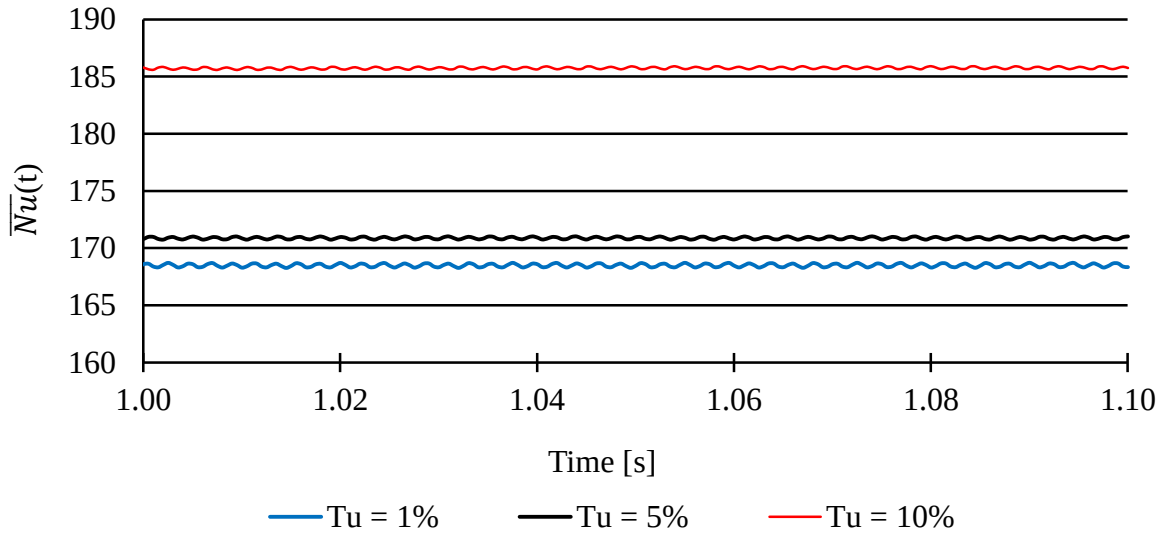


Figure 5.8 (c) All-angle-average spatial average $\overline{Nu}(\mathrm{t})$ numbers varying with time, [*Re* = 50,000, $T_w$ = uniform].

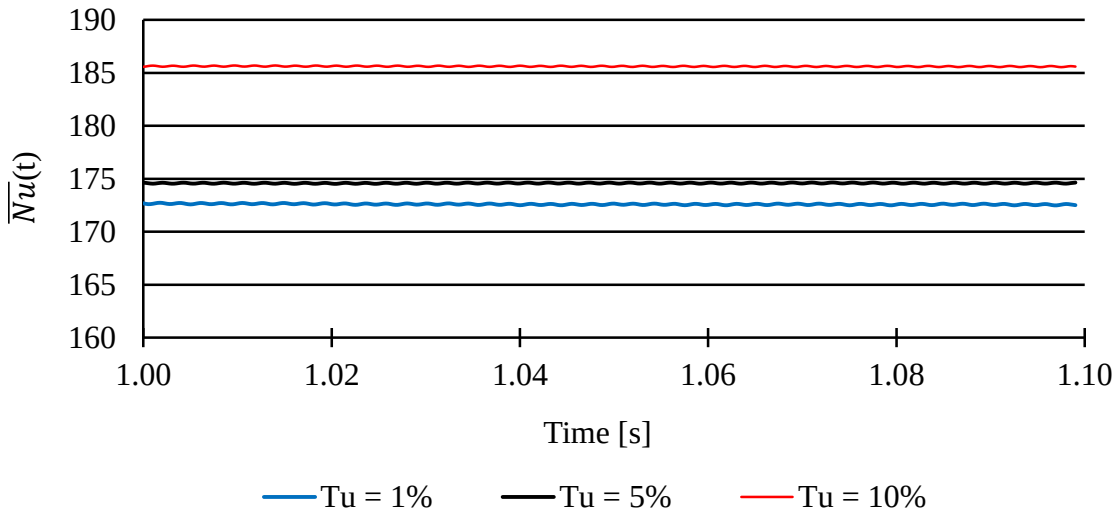


Figure 5.8 (d) All-angle-average spatial average $\overline{Nu}$(t) numbers varying with time, [*Re* = 50,000, $q_w$ = uniform].

## 5.7 Time- and Spatial-average Nusselt Numbers

### 5.7.1 Present results

The next focus is on time- and spatial-averages of the Nusselt number. This quantity is the most commonly appearing in the heat transfer design literature. The values of this quantity that have been extracted from the present calculations are summarized in Tables 5.2(a) and (b). To avoid possible initial-condition effects, the average values are calculated after 0.3 seconds. The Nusselt numbers for the uniform heat flux case are slightly smaller than those for the uniform temperature case when Reynolds number is 10,000. Conversely, the Nusselt numbers for the uniform heat flux case are slightly higher than those for the uniform temperature case when Reynolds number is 50,000.

Table 5.2 (a) Spatial- and time-average $\overline{Nu}$ number [*Re* = 10,000].

| | $\overline{Nu}$ number | | |
|---|---|---|---|
| | A: $T_w$ = uniform | B: $q_w$ = uniform | B compared to A [%] |
| *Tu* = 1% | 63.9 | 61.5 | -3.7 |
| *Tu* = 5% | 66.2 | 65.2 | -1.5 |
| *Tu* = 10% | 71.9 | 69.9 | -2.8 |

Table 5.2 (b) Spatial- and time-average $\overline{Nu}$ number [*Re* = 50,000].

| | $\overline{Nu}$ number | | |
|---|---|---|---|
| | A: $T_w$ = uniform | B: $q_w$ = uniform | B compared to A [%] |
| *Tu* = 1% | 168.5 | 172.7 | 2.5 |
| *Tu* = 5% | 170.9 | 174.6 | 2.2 |
| *Tu* = 10% | 185.7 | 185.6 | -0.1 |

### 5.7.2 Literature comparisons

It is appropriate to validate the current simulation model by comparing $\overline{Nu}$ number results with those of the published literature being experimentally studied. The present time- and spatial-average $\overline{Nu}$ numbers for both Re = 10,000 and 50,000 have been compared with literature [45 and 54]. The current study has *Tu* = 10%, and the literature [45 and 54] has *Tu* = 11 - 12% for the specific Reynolds number. The comparison in Figure 5.9 shows an excellent agreement between the present predictions and the published data.

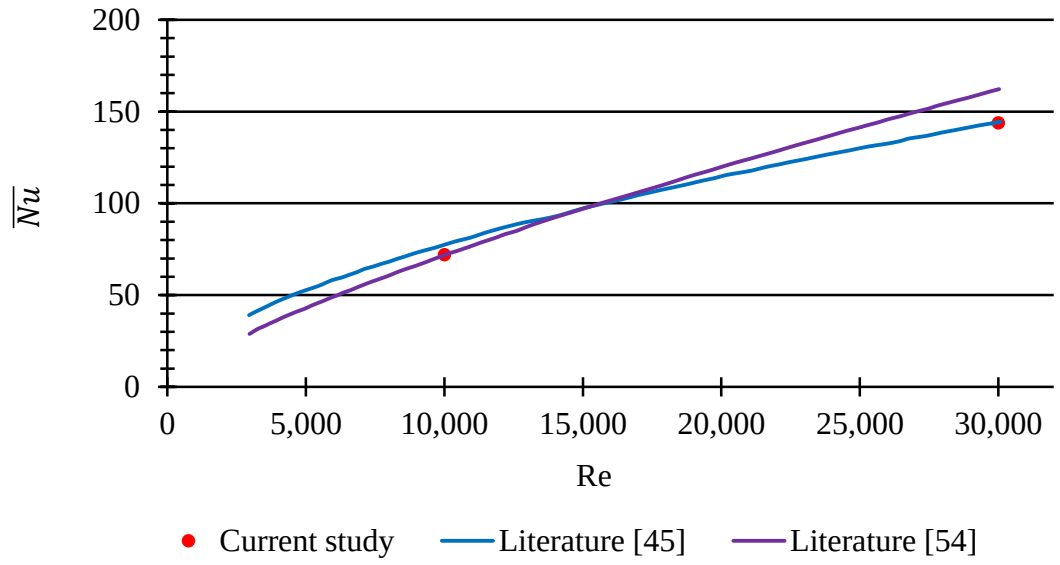


Figure 5.9 Spatial- and time-average $\overline{Nu}$ number comparison with literature. (a) Current study $Tu$ = 10%, (b) Literature [45]: $Tu$ = 11~12%, (c) Literature [54]: $Tu$ = 11~12%.

Attention now is directed to researchers' correlation and the comparison. Skimanovic et al. [43] achieved by experiment the equation for a circular cylinder in turbulent crossflow. Their equation is given below based on Reynolds number of 19,000 and turbulence intensity ranging from 2.5% to 16%.

$$\overline{Nu} = 0.25Re^{0.618} + 0.488Re^{1.118}\left(\frac{Tu}{100}\right) - 0.914Re^{1.618}\left(\frac{Tu}{100}\right)^2 \quad (5.9)$$

Kondjoyan et al. [45] also obtained by experiment the correlation based on freestream turbulence intensity and Reynolds number for a circular cylinder in crossflow. Their correlation (5.10) is for the Reynolds number range between 3,000 and 40,000 and turbulence intensity ranging from 1% to 45%.

$$\overline{Nu} = (1.07 + 0.015Tu\sqrt{Re}) \times 0.63\sqrt{Re} \quad (5.10)$$

The correlation for a circular cylinder in crossflow based on experiments from Mehendale et al. [55] is given below for 25,000 < Re < 100,000 and for 0.73% < *Tu* < 15.2%.

$$\overline{Nu} = 0.902\sqrt{Re} + 2.14\,Re\left(\frac{Tu}{100}\right) - 2.89\sqrt{Re^3}\left(\frac{Tu}{100}\right)^2 \qquad (5.11)$$

The comparisons made here are between the current numerical simulation results and the correlations (5.9) through (5.11) from literature [43, 45, and 55]. These comparisons for different Reynolds numbers, 10,000, 30,000, and 50,000 are shown in Figure 5.10 (a) – (c). The current simulation results are very close to those of Kondjoyan [45] for all Reynolds number cases. Lesser agreement is attained with Mehendale [55], for which the present results fall about 30% low. For one thing, the slope $\frac{d\overline{Nu}}{dTu}$ of the literature curves are higher than those of the present results. In particular, the slope in the equation of Mehendale et al. is steeper than the others because their equation is much influenced by the fact that they had results for higher Reynolds numbers. In that sense, the comparison of the present results with Mehendale is somewhat inappropriate.

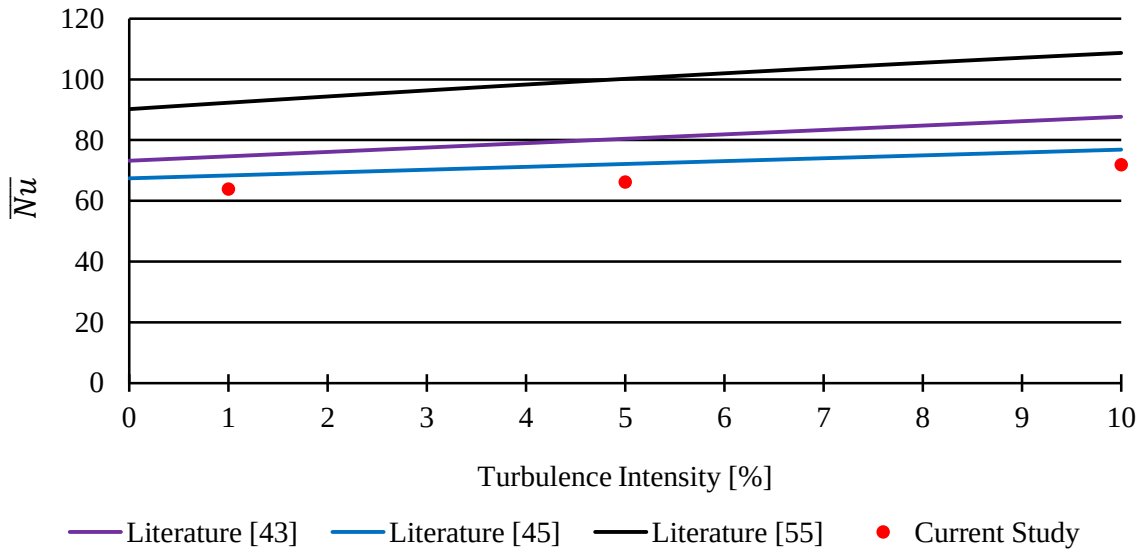


Figure 5.10 (a) $\overline{Nu}$ number as a function of *Tu* at Re = 10,000.

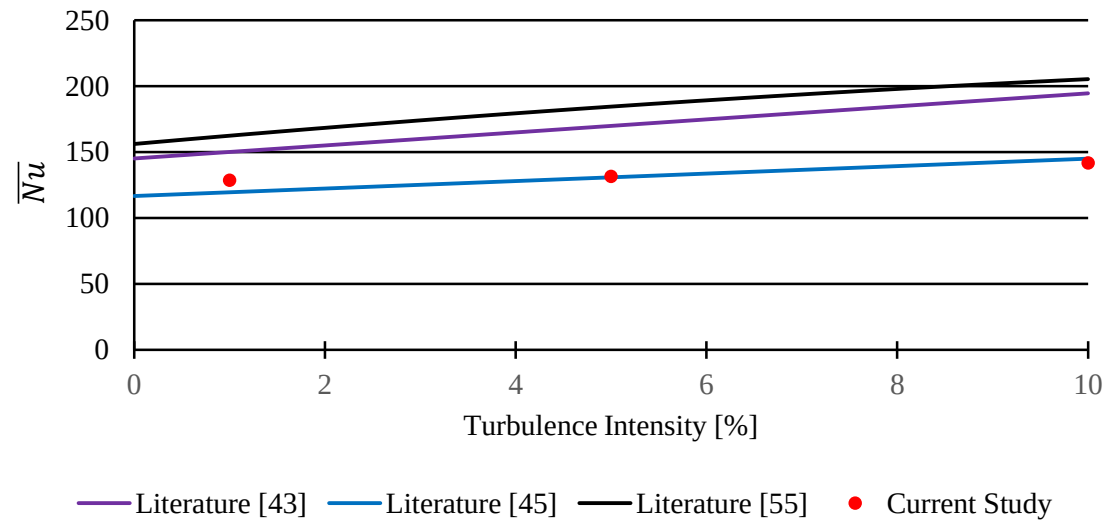


Figure 5.10 (b) $\overline{Nu}$ number as a function of $Tu$ at Re = 30,000.

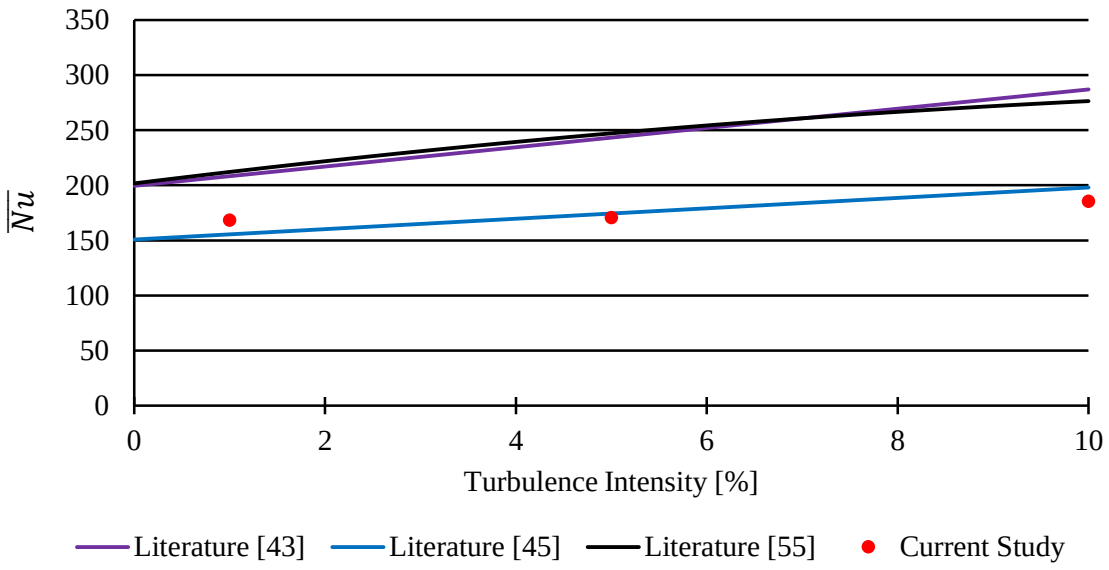


Figure 5.10 (c) $\overline{Nu}$ number as a function of $Tu$ at Re = 50,000.

## 5.8 Investigation of New Correlation

It is necessary to create a new correlation because there is no unique correlation which represents both low and high Reynolds numbers well. It is seen that the relationship based on the higher Reynolds numbers has a higher slope ($\frac{d\overline{Nu}}{dTu}$) than those based on lower Reynolds numbers. Graphical representations of the spatial- and time-average Nusselt numbers are plotted in Figure 5.11 and 5.12 respectively as functions of *Tu* and *Re*.

The correlation in Figure 5.12 shows that at higher Reynolds, it has higher slope ($\frac{d\overline{Nu}}{dRe}$). From Figure 5.11, it appears that $\frac{d\overline{Nu}}{dTu}$ increases with increasing turbulence intensity. For the both cases, $R^2$ values are 1, which suggests that the equations almost perfectly match the results. This correlation can be combined based on the results of the $\overline{Nu}$ ratios shown in Table 5.3. It demonstrates that the $\overline{Nu}$ ratios at each turbulence intensity is almost same so that it is possible to make one consolidated correlation.

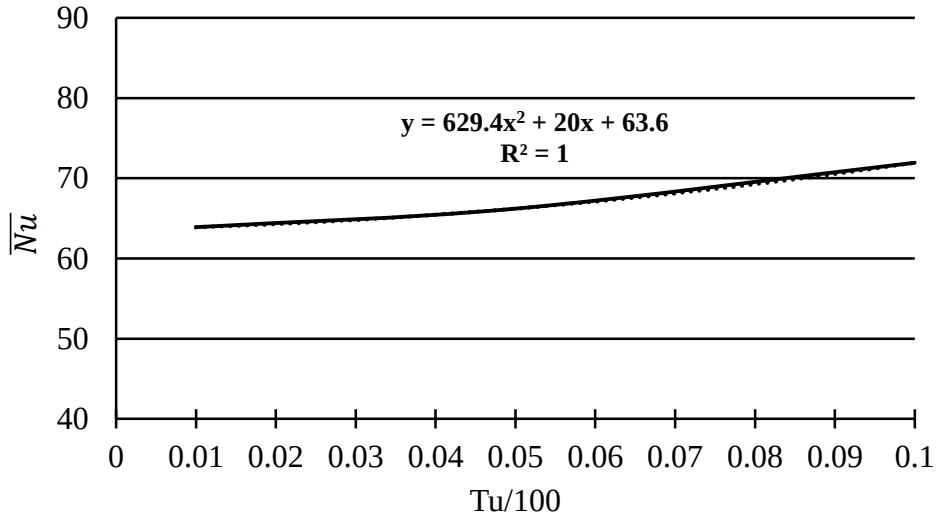


Figure 5.11 Spatial- and time-average $\overline{Nu}$ as a function of *Tu* at *Re* = 10,000.

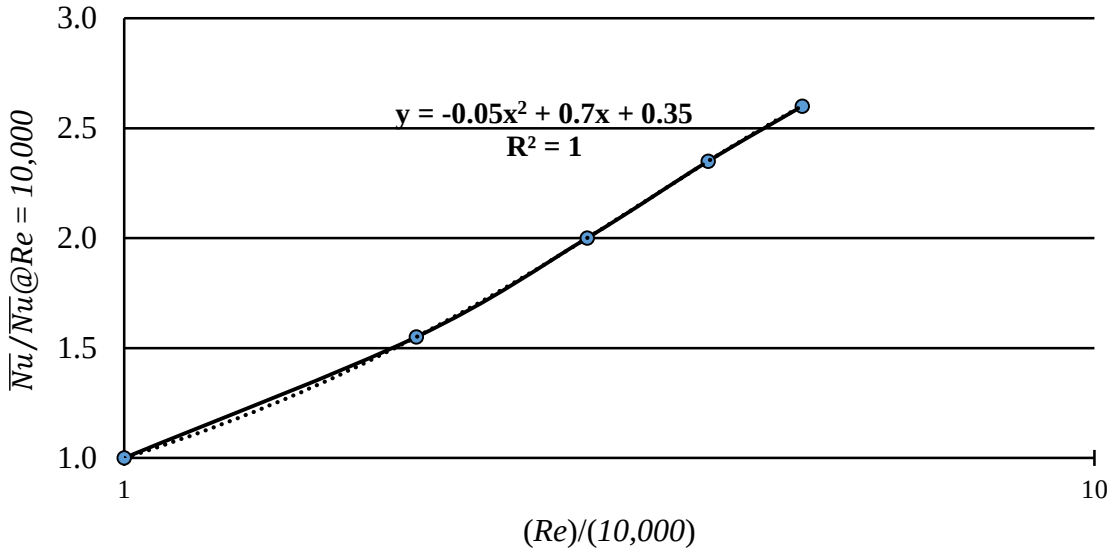


Figure 5.12 Spatial- and time-average $\overline{Nu}$ as a function of *Re* at using average $\overline{Nu}$ ratios at *Tu* = 1%, 5%, and 10%. Horizontal axis is logarithmic.

Table 5.3 Spatial- and time-average $\overline{Nu}$ at each *Re* and *Tu*.

| | *Re* | | | $\overline{Nu}$ Ratio | |
|---|---|---|---|---|---|
| | 10,000 | 30,000 | 50,000 | 30,000/10,000 | 50,000/10,000 |
| *Tu* = 1% | 63.9 | 128.7 | 168.5 | 2.0 | 2.6 |
| *Tu* = 5% | 66.2 | 131.5 | 170.9 | 2.0 | 2.6 |
| *Tu* = 10% | 71.9 | 141.9 | 185.7 | 2.0 | 2.6 |

Based on the information in the table, a correlation equation (5.12) is determined. This correlation is for *10,000 < Re < 50,000* and for *1% < Tu < 10%*. It is not a linear relationship which has also been shown in other correlations. At higher Reynolds numbers and higher turbulence intensities, the slopes are steeper, and vice versa. It improves a weakness of other correlations from prior research and consolidates those.

$$\overline{Nu} = [629.4(\frac{Tu}{100})^2 + 20\left(\frac{Tu}{100}\right) + 63.6] \times [-0.05(\frac{Re}{10{,}000})^2 + 0.7\left(\frac{Re}{10{,}000}\right) + 0.35] \quad (5.12)$$

The information conveyed in Table 5.4 is a comparison between average Nusselt numbers from the simulations and those from the correlation (5.12). Those are in excellent agreement with each other. Additional Reynolds number cases, *Re* = 20,000 and 40,000 were run to validate the correlation (5.12). The results from those Reynolds numbers also well match this correlation without interfering the fact that R square is one.

Table 5.4 Comparison of spatial- and time-average $\overline{Nu}$ from simulation with that from correlation (5.12).

| | Re | | | | | |
|---|---|---|---|---|---|---|
| | 10,000 | | 30,000 | | 50,000 | |
| | Simulation | Equation | Simulation | Equation | Simulation | Equation |
| $Tu$ = 1% | 63.9 | 63.9 | 128.7 | 127.7 | 168.5 | 166.0 |
| $Tu$ = 5% | 66.2 | 66.2 | 131.5 | 132.3 | 170.9 | 172.1 |
| $Tu$ = 10% | 71.9 | 71.9 | 141.9 | 143.8 | 185.7 | 186.9 |

Sak et al. [47] also presented correlation at *Re* = 27,700 and 2.9% < *Tu* < 8.3% below.

$$\overline{Nu} = 114.2 + 465.9\,Tu \tag{5.13}$$

Since the current study does not have results for the specific Reynolds number (27,700), the correlation (5.12) corresponding to Reynolds number ranging from 10,000 to 50,000 can be used for comparison. The comparison displayed in Figure 5.9 demonstrates that the agreement is highly satisfactory.

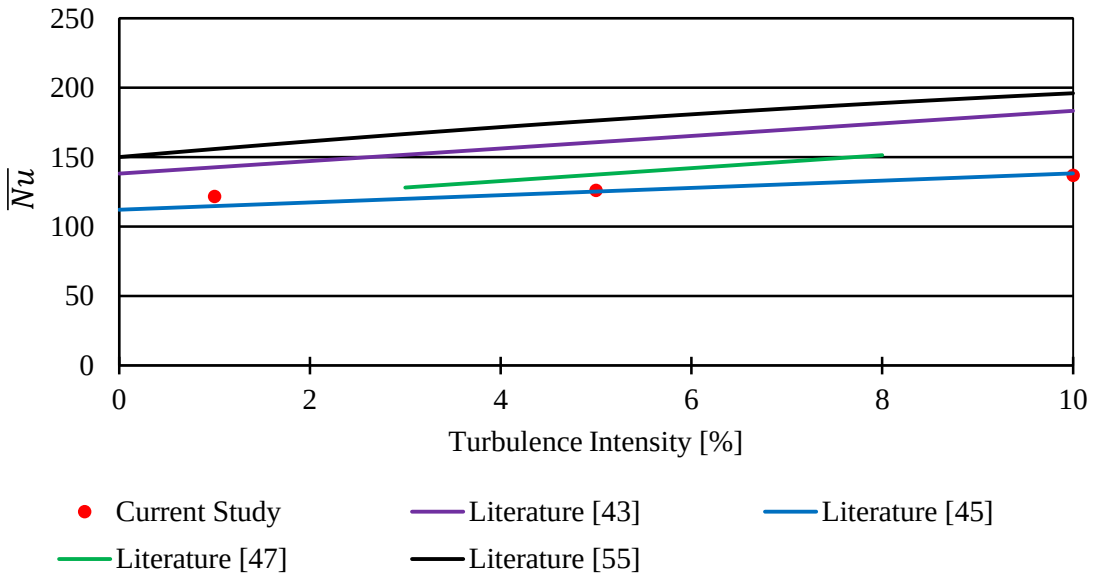


Figure 5.13 $\overline{Nu}$ numbers as a function of turbulence intensity at Re = 27,700.

## 5.9 Comparison of Results Using Different Turbulence Models: SST vs. SAS-SST

It is relevant to investigate if there is turbulence model dependence on the dimensionless heat transfer results. The spatial- and time-average $\overline{Nu}$ values have been compared and listed in Table 5.5 for two different turbulence models: SST vs. SAS-SST. The same conditions, *Re* = 10,000, and *Tu* = 5%, have been used for a fair comparison. The difference between spatial- and time-average *Nu* from the two models is only 1.5%. This outcome proves that the results do not depend on turbulence models.

The difference between SST model and SAS-SST model is in the way of dealing with the turbulence length-scale. SAS-SST model allows to adapt the length-scale automatically to the resolved scales of the flow field in unsteady flow regions. For SAS-SST model, one additional SAS sources term is added to the governing equations of SST model.

Table 5.5 Spatial- and time- average $\overline{Nu}$ number comparison [$Re$ = 10,000, $Tu$ = 5%]: SST model vs. SAS-SST model.

| $\overline{Nu}$ Comparison | | |
|---|---|---|
| A: SST model | B: SAS-SST model | B compared to A (%) |
| 66.2 | 65.2 | 1.5 |

## 5.10 Concluding Remarks

The investigation of heat transfer at the surface of a cylinder in crossflow conducted in this chapter contains a number of novel features. A major independent variable is the magnitude of the freestream turbulence intensity and a second is the Reynolds number. The overall slate of results includes: (a) timewise variations of the local heat transfer coefficient, (b) timewise variations of the spatial-average heat transfer coefficient, (c) spatial variations of the timewise-average heat transfer coefficient, (d) spatial- and timewise-average heat transfer coefficient as a function of turbulence intensity and Reynolds number, (e) timewise fluctuation frequencies, (f) correlations of the spatial- and timewise-average heat transfer coefficient with turbulence intensity and Reynolds number. This collection of results is believed to be the most comprehensive among any that are found in the published literature. In particular, the local and spatial-average timewise variations of the heat transfer coefficient presented here constitute the most extensive information on timewise variations available.

Whenever possible, the present results were compared with those of the published literature. Such comparisons could not be made for those results for which there is a timewise feature since the literature is not well represented. Therefore, only those quantities which do not depend on time were available for comparison. One such quantity is the spatial variation of the local heat transfer coefficient around the circumference of the cylinder. There are several papers that deal with this quantity in the published literature, and it appears that these do not form a tight consensus. The present results fall in with the general range of the literature values.

The major correlation effort of this chapter is focused on relating the spatial- and timewise-average heat transfer coefficient with the Reynolds number and the turbulence intensity. In that regard, available literature relationships were demonstrated to be insufficient. The correlation formulated here is believed to be the very best that is now available.

Another issue considered in this chapter relates to the difference between the results for the uniform wall temperature and the uniform wall heat flux boundary conditions. The heat transfer coefficients for the two cases differed by no more than a few percent. However, the relative magnitudes (higher or lower) were different for different Reynolds numbers.

The frequency of the timewise periodic variations of the local and spatially averaged heat transfer coefficients were presented in dimensionless form by means of the Strouhal number. It was found that the values of the Strouhal number were insensitive to the magnitude of the turbulence intensity and varied only slightly with the Reynolds number.

Another outcome of this chapter is that the local heat transfer coefficient is not precisely axisymmetric. In particular, the circumferential variation of the coefficient on the upper half of the cylinder is not quite the same as on the lower half. The differences are mostly in evidence in the neighborhood of the point of boundary layer separation.

# CHAPTER 6

## ACCOMPLISHMENTS

The general theme of this thesis is applications-useful heat transfer fundamentals for crossflow heat exchangers. Since convective heat transfer is at the core of the work, it is natural that fluid mechanics fundamentals, both for laminar and turbulent flow, would be deeply involved. The primary tool for the execution of the thesis is numerical simulation, a necessary prerequisite for the use of which is validation. Here, validation was achieved by comparisons of specially executed numerical solutions with very highly accurate experiments performed in our laboratory.

### 6.1 Chapter Two

Three very different categories of crossflow heat exchangers are considered here, varying in levels of complexity. The first category, dealt with in Chapter Two, is multi-row tube banks. This category, although well researched, is beset with many uncertainties due to poorly executed and misunderstood research outcomes.

For example, the issue of flow regime corresponding to certain reported experiments is still in doubt. It is appropriate to discuss how this issue was treated here. To set the stage for the approaches used in this thesis, it is relevant to note that there is a turbulence model that reduced to a laminar flow model when it is applied to a flow which is truly laminar. With this knowledge, duplicate solutions, one laminar and the other turbulent, were obtained for a variety of physical situations. When the two solutions gave identical results, it was concluded that the flow was laminar. If the solutions differed significantly, turbulence was concluded. A second approach was based on calculating the ratio of the turbulent viscosity to the laminar (molecular) viscosity using numerical simulations.

When values of this ratio were found to be very much below one, it was concluded that laminar flow prevailed. On the other hand, if the ratio achieved values of several tenths and greater, purely laminar flow no longer existed. The two methods of identifying the flow regime yielded the same outcome.

The foregoing discussion was intended to convey an example of how the research of Chapter two was carried out. A summary of the accomplishments of Chapter Two follows:

O The nature of the flow regime, laminar versus turbulent, was evaluated by means of two independent approaches. (i) Compared predicted heat transfer coefficients from a laminar model and a turbulent model. (ii) Determined magnitude of the turbulent viscosity relative to the laminar viscosity.

O Identified the array population that gives rise to Nusselt numbers that are independent of the population size. This determination provides a means of defining a fully developed regime.

O Demonstrated that shorter arrays give rise to higher array-average Nusselt numbers than do longer arrays.

O Showed that geometric symmetry prevails for different symmetric models of the solution domain.

O Variation of pressure as a function of location in the array demonstrated the influence of alternating velocity accelerations and decelerations.

O Showed that after the initial rows of the array, the per-row pressure drop became constant, indicating flow periodicity.

O Flow visualization was accomplished by means of vector diagrams and streamline patterns. The flow was shown to be two-faced in that it consisted of a through flow stream and a succession of captured eddies.

O Demonstrated that for laminar flow, in contrast to turbulent flow, start-up flow transients do converge to steady state.

O Determined the array-average Nusselt numbers for arrays of different numbers of cylinders.

## 6.2 Chapter Three

Chapter Three of the thesis has already been mentioned briefly at the beginning of this summarizing chapter. In Chapter Three, the validation of the simulation model was described in detail. The numerical predictions were in excellent agreement with experimental measurements, providing irrefutable proof of the numerical simulation model and its implementation.

## 6.3 Chapter Four

Chapter Four addresses a very profound issue in heat exchanger analysis. A heat exchanger and the fluid mover (e.g., fan or blower) which delivers a flowing fluid to the exchanger inlet may experience profound interactions which argues against treating them as separate entities. On the other hand, current design practice takes account of fluid-thermal interactions within the heat exchanger proper, but the fluid delivered to the heat exchanger inlet is specified without consideration of any possible influence of the exchanger or of the type of fluid mover. Most commonly, the magnitude of the flowrate arriving at the exchanger inlet is based on the pressure rise-flowrate curve (P-Q) curve

supplied by the manufacturer of the fan or blower coupled with the unsubstantiated assumption that the flow is uniformly distributed across the exchanger inlet.

The literature has shown that the traditional P-Q curves do not apply when the fluid mover is heavily loaded. In addition, it is a major idealization to assume that the delivered flow is uniformly distributed. In Chapter Four, these issues are addressed in detail in a case-study format by means of numerical simulation. That case study deals with a pin-fin array housed in a duct, with air supplied in crossflow either by means of a rotating fan or in accordance with a P-Q curve.

The research performed in Chapter Four has demonstrated the importance of properly accounting for the nature of the flow delivered to the inlet cross section of a heat exchanger. Although the best current design protocol makes use of the P-Q curves supplied by the fan manufacturer, the resulting heat transfer predictions are not correct. For one thing, research has shown that the manufacturer-supplied P-Q curves are flawed because no account was taken of the change of the fan performance in the presence of a downstream load. Perhaps of greater significant is that the P-Q model does not take account of the true nature of the flow delivered to the inlet of the heat exchanger. It has been demonstrated here that a more appropriate approach is to consider the fluid mover and the heat exchanger as a single system, thereby enabling them to interact with each other.

The complex flow, including swirl, delivered to the inlet of the heat exchanger by the rotating fan encounters significant fluid resistance within the pin-fin array, with the outcome being a significant reduction in the delivered rate of flow compared with that for the P-Q models. Those models envision the delivered flow as uniform and parallel. From the present numerical solutions for both the fan-delivered and P-Q delivered cases, it was found that the fan-delivered flow was approximately 37% of that of the velocity-driven P-Q flow model. This outcome leads to the expectation of a large reduction of the heat transfer for the fan-driven flow. On the other hand, the actual reductions in the rate of

heat transfer obtained from the numerical simulations were modest, no greater than 27%. This outcome can be attributed to the intense mixing of the fan-driven flow within the pin-fin array. That mixing tends to compensate for the diminished flow rate for the fan-driven case.

## 6.4 Chapter Five

The special focus of Chapter Five was to determine the impact of turbulence intensity of the heat transfer performance of heat exchangers. Whereas this goal served to motivate the investigation described in Chapter Five, other issues of equal importance emerged. The most remarkable issue was the virtually perfectly periodic timewise fluctuations of the heat transfer results, both local and spatial averaged. Unsteady operation in the presence of constant boundary conditions often consists of a start-up transient, which depends on the specifics of the initial conditions, followed by a steady or a periodic steady state. In the situation studies in Chapter Five, the start-up transient was completed in approximately one second, and the periodic steady-state continued on without interruption. In addition to the freestream turbulence as a primary independent variable, a second is the Reynolds number.

The overall slate of results includes: (a) timewise variations of the local heat transfer coefficient, (b) timewise variations of the spatial-average heat transfer coefficient, (c) spatial variations of the timewise-average heat transfer coefficient, (d) spatial- and timewise-average heat transfer coefficient as a function of turbulence intensity and Reynolds number, (e) timewise fluctuation frequencies, (f) correlations of the spatial- and timewise-average heat transfer coefficient with turbulence intensity and Reynolds number. This collection of results is believed to be the most comprehensive among any that are found in the published literature. In particular, the local and spatial-average timewise variations of the heat transfer coefficient presented here constitute the most extensive information on timewise variations available.

The major correlation effort of this chapter is focused on relating the spatial- and timewise-average heat transfer coefficients with the Reynolds number and the turbulence intensity. In that regard, available literature relationships were demonstrated to be insufficient. The correlation formulated here is believed to be the very best that is now available.

Whenever possible, the present results were compared with those of the published literature. Such comparisons could not be made for those results for which there is a timewise feature since the literature is not well represented. Therefore, only those quantities which do not depend on time were available for comparison. One such quantity is the spatial variation of the local heat transfer coefficient around the circumference of the cylinder. There are several papers that deal with this quantity in the published literature, and it appears that these do not form a tight consensus. The present results fall in with the general range of the literature values.

The frequency of the timewise periodic variations of the local and spatially averaged heat transfer coefficients were presented in dimensionless form by means of the Strouhal number. It was found that the values of the Strouhal number were insensitive to the magnitude of the turbulence intensity and varied only slightly with the Reynolds number.

Another outcome of this chapter is that the local heat transfer coefficient is not precisely axisymmetric. In particular, the circumferential variation of the coefficient on the upper half of the cylinder is not quite the same as on the lower half. The differences are mostly in evidence in the neighborhood of the point of boundary layer separation. This finding contradicts the symmetry assumption made by several earlier investigators.

Still another issue considered in this chapter relates to the difference between the results for the uniform wall temperature and the uniform wall heat flux boundary conditions. The heat transfer coefficients for the two cases differed by no more than a few percent.

However, the relative magnitudes (higher or lower) were different for different Reynolds numbers.

All told, it is the writer's hope that this thesis has added significantly to both the fundamentals and applications knowledge bases for crossflow heat exchangers.

## References

[1] E. M. Sparrow, J. C. K. Tong, and J. P. Abraham, Fluid flow in a system with separate laminar and turbulent zones, *Numer. Heat Tr. A. – Appl.*, vol. 53, pp. 341-353, 2008.

[2] A. West, B. E. Launder, and H. Iacovides, On the computational modelling of flow and heat transfer in in-line tube banks, *First U.K. National Conference on Heat Transfer*, p 1097-1114 vol.2, 1984.

[3] Y. Takemoto, K. Kawanishi, and J. Mizushima, Heat transfer in the flow through a bundle of tubes and transitions of the flow, *International Journal of Heat and Mass Transfer*, v 53, n 23-24, p 5411-19, 2010.

[4] W. M. Kays and R. K. Lo, Basic heat transfer and flow friction design data for gas flow normal to banks of staggered tubes – use of a transient technique, *Tech. Rept. 15, Navy Contract N6-ONR-251 T. O. 6*, Stanford University, 1952.

[5] W. M. Kays, A. L. London, and R. K. Lo, Heat-transfer and friction characteristics for gas flow normal to tube banks, use of transient-test technique, *American Society of Mechanical Engineers - Transactions*, v 76, n 3, p 387-396, 1954.

[6] A. Zukauskas, Heat transfer from tubes in crossflow, *Advances in Heat Transfer*, v 18, p 87-160, 1987.

[7] B. W. Floan, and E. M. Sparrow, Fluid flow in heat exchangers whose flow passages contain periodically deployed tubes, *Numerical Heat Transfer, Part A (Applications)*, v 62, n 2, p 81-94, 2012.

[8] M. Fujii, and T. Fujii, A numerical analysis of laminar flow and heat transfer of air in an in-line tube bank, *Numerical Heat Transfer*, v 7, n 1, p 89-102,1984.

[9] O. L. Pierson, Effect of tube arrangement on convection heat transfer and flow resistance in cross flow of gases over tube banks, *Transactions of the ASME*, v 59, p 563-572, 1937.

[10] F. P. Incropera, D. P. Dewitt, T. L. Bergman, and A. S. Lavine, Introduction to heat transfer, 5th edition, *John Wiley and Sons*, 2007.

[11] S. W. Churchill, A Reinterpretation of the turbulent Prandtl number, *Ind. Eng. Chem. Res.*, vol. 41, pp. 6393-6401, 2002.

[12] W. M. Kays, Turbulent Prandtl number—Where are we?, *J. Heat Trans. ASME*, vol. 116, pp. 284-295, 1994.

[13] E. M. Sparrow, and J. W. Ramsey, Heat transfer and pressure drop for a staggered wall-attached array of cylinders with tip clearance, *International Journal of Heat and Mass Transfer*, v 21, p 1369-1377, 1978.

[14] E. M. Sparrow, J. W. Ramsey, and C. A. C. Altemani, Experiments on in-line pin fin arrays and performance comparisons with staggered arrays, *Journal of Heat Transfer*, v 102, n 1, p 44-50, 1980.

[15] E. M. Sparrow, and A. Hajiloo, Measurements of heat transfer and pressure drop for an array of staggered plates aligned parallel to an air flow, *Transactions of the ASME. Journal of Heat Transfer*, v 102, n 3, p 426-432, 1980.

[16] K. A. Moores, J. Kim, and Y. K. Joshi, Heat transfer and fluid flow in shrouded pin fin arrays with and without tip clearance, *International Journal of Heat and Mass Transfer*, v 52, n 25-26, p 5978-5989, 2009.

[17] S. W. Chang, T. L. Yang, and C. C. Huang, Endwall heat transfer and pressure drop in rectangular channels with attached and detached circular pin-fin array, *International Journal of Heat and Mass Transfer*, v 51, n 21-22, p 5247-5259, 2008.

[18] S. Rangadinesh, M. Rajasekar, S. Arunkumar, and M. Venkatesan, Experimental and numerical analysis on heat transfer characteristics of shoe brush-shaped fins, *Current Science*, v 106, n 10, p 1414-1420, 2014.

[19] H. Bayat, A. M. Lavasani, and T. Maarefdoost, Experimental study of thermal-hydraulic performance of cam-shaped tube bundle with staggered arrangement, *Energy Conversion and Management*, v 85, p 470-476, 2014.

[20] G. P. Merker, and H. Hanke, Heat transfer and pressure drop on the shell-side of tube-banks having oval-shaped tubes, *International Journal of Heat and Mass Transfer*, v 29, n 12, p 1903-1909, 1986.

[21] A. P. Fraas, Heat exchanger design, second edition, John Wiley & Sons, 1989.

[22] J.-H. Zhou, and C.-X. Yang, Design and simulation of the CPU fan and heat sinks, *IEEE T. Compon. Pack. T.*, vol. 31, pp. 890-903, 2008.

[23] D. Agonafer, and A. Free, Conjugate model of a pin-fin heat sink using a hybrid conductance and CFD model within an integrated MCAE tool, *Thermal Management of Electronic Systems II*. Springer Netherlands, pp. 53-62, 1997.

[24] A. Sanyal, K. Srinivasan, and P. Dutta, Numerical study of heat transfer from pin-fin heat sink using steady and pulsated impinging jets, *IEEE T. Compon. Pack. T.*, vol. 32, pp. 859-867, 2009.

[25] S. Sathe, K. M. Kelkar, K. C. Karki, C. Tai, C. Lamb, and S. V. Patankar, Numerical prediction of flow and heat transfer in an impingement heat sink, *J. Electron. Packaging*, vol. 119, pp. 58-63, 1997.

[26] N. Sahiti, A. Lemouedda, D. Stojkovic, F. Durst, and E. Franz, Performance comparison of pin fin in-duct flow arrays with various pin cross-sections, *Appl. Therm. Eng.*, vol. 26, pp. 1176-1192, 2006.

[27] J. F. Mitre, L. M. Santana, R. B. Damian, J. Su, and P. L. C. Lage, Numerical study of turbulent heat transfer in 3D pin-fin channels: Validation of a quick procedure to estimate mean values in quasi-periodic flows, *Appl. Therm. Eng.*, vol. 30, pp. 2796-2803, 2010.

[28] T. Izci, M. Koz, and A. Koar, The effect of micro pin-fin shape on thermal and hydraulic performance of micro pin-fin heat sinks, *Heat Transfer Eng.*, vol. 36, pp. 1447-1457, 2015.

[29] Y. Rao, C. Wan, and S. Zang, An experimental and numerical study of flow and heat transfer in channels with pin fin-dimple combined arrays of different configurations, *J. Heat Trans. ASME*, vol. 134, pp.121901, 2012.

[30] A. K. Saha, and S. Acharya, Parametric study of unsteady flow and heat transfer in a pin-fin heat exchanger, *Int. J. Heat Mass Tran.*, vol. 46, pp. 3815-3830, 2003.

[31] F. R. Menter, Two-equation eddy-viscosity turbulence models for engineering applications, *AIAA J.*, vol. 32, pp. 1598-1605, 1994.

[32] U. Engdar, and J. Klingmann, Investigation of two-equation turbulence models applied to a confined axis-symmetric swirling flow, *ASME 2002 Pressure Vessels and Piping Conference*, pp. 199-206, 2002.

[33] W. Li, J. Ren, J. Hongde, Y. Luan, and P. Ligrani, Assessment of six turbulence models for modeling and predicting narrow passage flows, part 2: Pin fin arrays, *Numer. Heat Tr. A. – Appl.*, vol. 69, pp. 445-463, 2016.

[34] A. Li, X. Chen, and L. Chen, Numerical investigations on effects of seven drag reduction components in elbow and T-junction close-coupled pipes, *Build. Serv. Eng. Res. T.*, vol. 36, pp. 295-310, 2014.

[35] Y. Bayazit, E. M. Sparrow, and D. D. Joseph, Perforated plates for fluid management: plate geometry effects and flow regimes, *Int. J. Therm. Sci.*, vol. 85, pp. 104-111, 2014.

[36] E. M. Sparrow, J. M. Gorman, and J. P. Abraham, Quantitative assessment of the overall heat transfer coefficient U, *J. Heat Trans. ASME*, vol.135, pp. 061102, 2013.

[37] F. R. Menter, M. Kuntz, R. Langtry, Ten years of industrial experience with the SST turbulence model, *Turbulence, Heat and Mass Transfer 4*, 2003.

[38] S. W. Churchill, A reinterpretation of the turbulent Prandtl number, *Ind. Eng. Chem. Res.*, vol. 41, pp. 6393-6401, 2002.

[39] G. V. Shankaran, M. B. Dogruoz, Validation of an advanced fan model with multiple reference frame approach, *2010 12th IEEE Intersociety Conference on Thermal and Thermomechanical Phenomena in Electronic Systems*, ITherm 2010.

[40] J. Kestin, P. F. Maeder, and H. H. Sogin, The influence of turbulence on the transfer of heat to cylinders near the stagnation point, *Zeitschrift fuer Angewandte Mathematik und Physik*, v 12, n 2, p 115-132, 1961.

[41] J. Kestin, R. T. Wood, The mechanism which causes free-stream turbulence to enhance stagnation-line heat and mass transfer, *International Heat Transfer Conference* 4, 1970.

[42] B. B. B. Jensen, Numerical study of influence of inlet turbulence parameters on turbulence intensity in the flow domain: Incompressible flow in pipe system, *Proceedings of the Institution of Mechanical Engineers, Part E: Journal of Process Mechanical Engineering*, v 221, n 4, p 177-186, 2007.

[43] S. Sikmanovic, S. Oka, and S. Koncar-Djurdjevic, Influence of the structure of turbulent flow on heat transfer from a single cylinder in a cross flow, *Jpn Soc of Mech Eng*, p 320-324, 1974.

[44] G. B. Zdanavichyus, V. Y. Survila, and A. A. Zukauskas, Influence of the degree of turbulence of an inflowing air stream on local heat transfer on a circular cylinder in the critical flow regime, *International Chemical Engineering*, v 17, n 1, p 115-121, Jan 1977.

[45] A. Kondjoyan, and J. D. Daudin, Effects of free stream turbulence intensity on heat and mass transfer at the surface of a circular cylinder and an elliptical cylinder, axis ratio 4, *International Journal of Heat and Mass Transfer*, v 38, n 10, p 1735-1749, 1995.

[46] F. Peyrin, and A. Kondjoyan, Effect of turbulent integral length scale on heat transfer around a circular cylinder placed cross to an air flow, *Experimental Thermal and Fluid Science*, v 26, n 5, p 455-460, July 2002.

[47] C. Sak, R. Liu, D. S. –K. Ting, and G. W. Rankin, The role of turbulence length scale and turbulence intensity on forced convection from a heated horizontal circular cylinder, *Experimental Thermal and Fluid Science*, v 31, n 4, p 279-289, 2007.

[48] M. Smith, and A. M. Kuethe, Effects of turbulence on laminar skin friction and heat transfer, *Physics of Fluids*, v 9, n 12, p 2337-2344, 1966.

[49] B. Sunden, A theoretical investigation of the effect of freestream turbulence on skin friction and heat transfer for a bluff body, *International Journal of Heat and Mass Transfer*, v 22, n 7, p 1125-1135, 1979.

[50] R. S. R. Gorla, N. Nemeth, Effects of free stream turbulence intensity and integral length scale on heat transfer from a circular cylinder in crossflow, *Heat Transfer 1982, Proceedings of the Seventh International Conference*, v 3, p 153-158, 1982.

[51] P. P. Vaitiekunas, A. J. Bulota, A. A. Zukauskas, Prediction of the point of separation of the turbulent boundary layer from a cylinder in cross flow, *Fluid mechanics. Soviet research*, v 15, n 4, p 72-81, 1986.

[52] S. Kim, H. Nakamura, Large eddy simulation of turbulent heat transfer around a circular cylinder in crossflow, *Proceedings of the 5th Joint ASME/JSME Fluids Engineering Summer Conference, FEDSM 2007*, v 2 FORA, PART A, p 233-238, 2007.

[53] H. Necula, E. N. Ghizdeanu, *UPB Scientific Bulletin, Series C: Electrical Engineering*, v 70, n 1, p 35-40, 2008.

[54] A. Kondjoyan, J. D. Daudin, J. J. Bimbenet, Heat and mass transfer coefficients at the surface of elliptical cylinders placed in a turbulent air flow, *Journal of Food Engineering*, v 20, n 4, p 339-367, 1993.

[55] A. B. Mehendale, J. C. Han, S. Ou, Influence of high mainstream turbulence on leading edge heat transfer, *Journal of Heat Transfer*, 113(4), 843-850, 1991.

[56] F. R. Menter and Y. Egorov, Revisiting the turbulent scale equation, *Solid Mechanics and its Applications*, v 129, p 279-290, 2006.

[57] T. Frank, M. Adlakha, C. Lifante, H.-M. Prasser, F. Menter, Simulation of turbulent and thermal mixing in T-Junctions using URANS and scale-resolving turbulence models in ANSYS CFX, *Nuclear Engineering and Design*, v 240, n 9, p 2313-2328, 2010.

[58] R. D. Blevins, Flow-induced vibration, *Van Nostrand Reinhold Co., Inc.*, 1990.